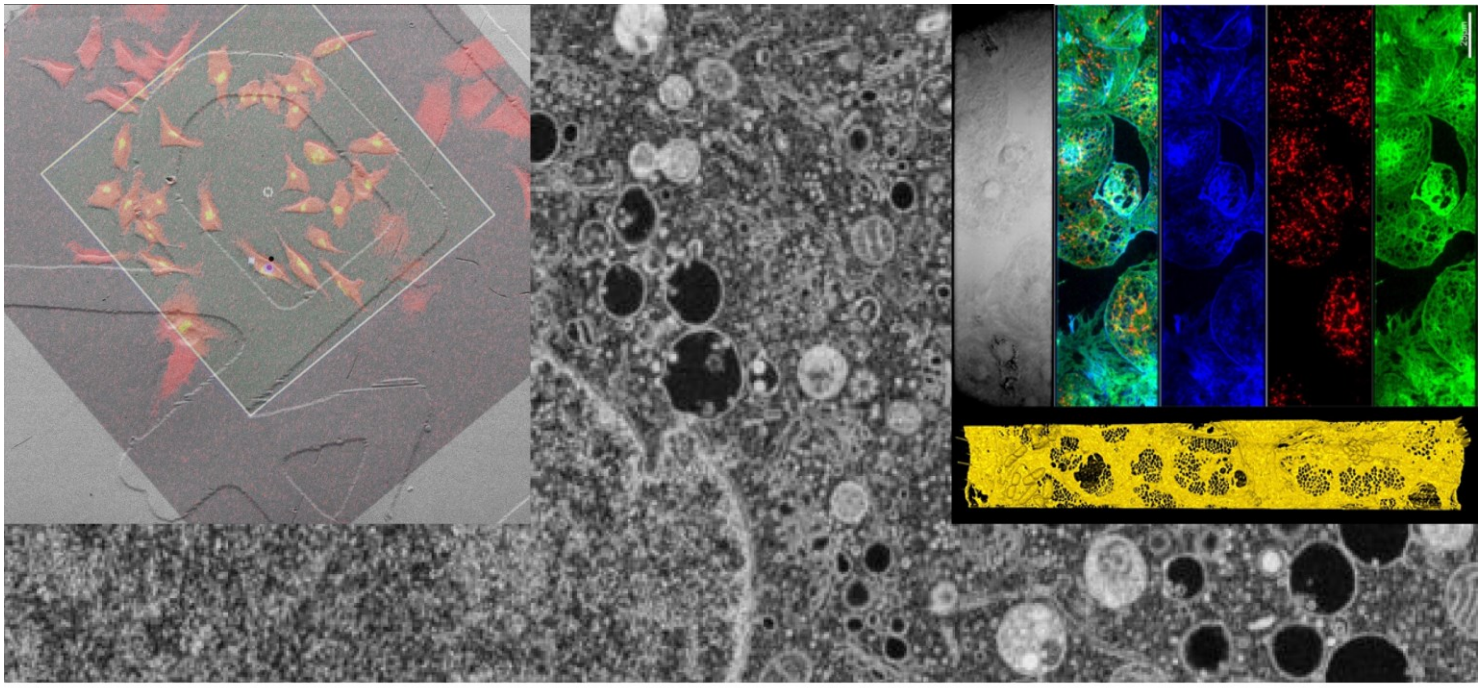

Correlative light and electron microscopy: new strategies for improved throughput and targeting precision

EMBL

Anna Maria Steyer

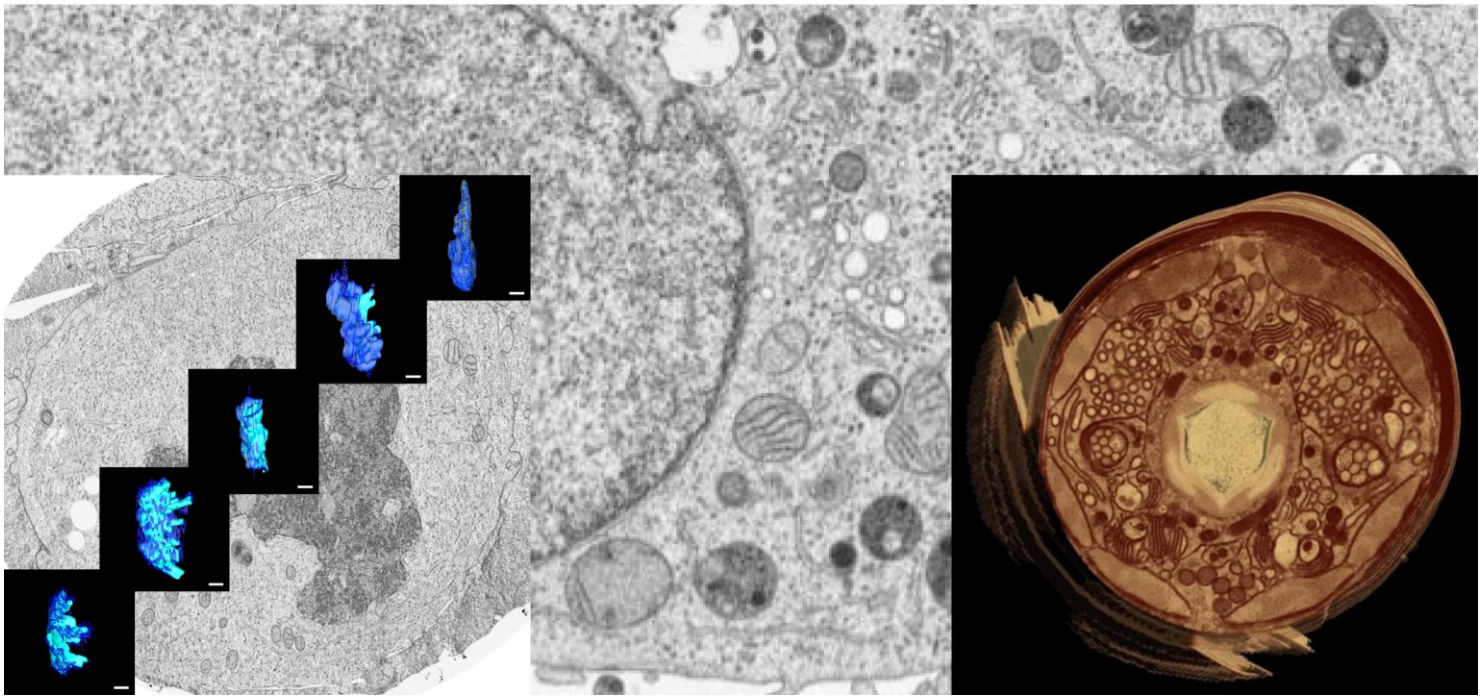

Dissertation

Submitted to the
Combined Faculties for the Natural Sciences and for Mathematics
of the Ruperto-Carola University of Heidelberg, Germany
for the degree of
Doctor of Natural Sciences

Presented by
Anna Maria Steyer, Dipl. Biol. (t.o.)
Born in Achim, Germany

Oral-examination:
30.03.2017

Correlative light and electron microscopy: new strategies for improved throughput and targeting precision

Conducted at

European Molecular Biology Laboratory

Cell Biology and Biophysics

Referees:

Dr. Anne-Claude Gavin

Prof. Dr. Ralf Bartenschlager

Acknowledgements

I would like to thank first of all my amazing boss **Yannick Schwab** for accepting me as his first PhD student. He has been always super enthusiastic, encouraging and supportive. He has made it possible to work on different amazing projects, developing different skills and tools associated with collaborative projects. Throughout my time as a PhD student Yannick has given me the opportunity to participate in different courses inside/outside EMBL, present my work at multiple national and international conferences and even represent our lab on different occasions. I would also like to thank him for his phenomenal feedback and continuous help with writing my thesis.

I would like to thank all the people that contributed to this work in one or the other way:

Matthia Karreman, who has been the first lab member I talked to and is the good spirit of the lab. She has been very important in lab / PhD related questions (Amira, Illustrator, Photoshop, just to name a few) and has become a great friend. I also have to thank her for working through my thesis and giving me highly appreciated feedback. As the third "Power Puff Girls" right from the beginning of joining the lab, **Nicole Schieber** has been the good soul and backbone of the lab. She has taught me different electron microscopy techniques like high-pressure freezing and serial sectioning. It has been an amazing time working and struggling with Phoebe 1 and 2 our focused ion beam-scanning electron microscope. It is also great to have some experimental help every now and then. I would also like to thank her for the valuable feedback on my thesis from a native speaker perspective. Nicole as well has become a dear friend. In my main project working on automating correlative light and electron microscopy I was blessed to work with **Jose Miguel Serra Lleti** a remarkable computer scientist and excellent partner in this project. Making our challenging automated CLEM pipeline work and struggling through new software versions and hardware updates would not have been possible without him. **Loredana Iovino** has been fabulous colleague to work with in the lab, experiencing the same ups and downs as a PhD student.

I also have to thank the marvelous people from the Electron Microscopy Core Facility (EMCF), who have been exceptionally supportive helping with, for example training on machines and feedback on the different projects. **Rachel Mellwig** has been a wonderful support with any scientific questions and a very thorough reading of my thesis. **Pedro Machado** has been challenging our workflows with the FIB-SEM. It has been a lot of fun writing a book chapter together with him about minimal resin. **Paolo Ronchi,** who has an amazing knowledge about

light and electron microscopy as well as the Golgi apparatus, has given very important feedback, especially on our automated CLEM screen looking at Golgi phenotypes. I want to thank **Martin Schorb** for his wonderful computer support for file-permissions, transferring data through different softwares to finally get the right file-format and help on analyzing 3D modeled data. Many thanks to **Androniki Kolovou** for giving feedback to my different projects and trying to accompany the EMBL choir with her electric guitar.

I have to thank the people from the Advanced Light Microscopy Facility (ALMF), who have been essential for the light microscopy pipeline of the project, for training on different light microscopes and feedback on my projects. In the automated CLEM project different expertise were needed and applied. **Beate Neumann** shared and adapted with me the spotting procedure to turn our petri dish into a miniaturized biological assay. **Christian Tischer** from the ALMF helped to set up a great image analysis pipeline for finding Golgi phenotypes. **Volker Hilsenstein** helped me with setting up the microscopy pipeline on the confocal microscope, including the relocation of the siRNA spots.

I would like to thank my TAC committee; **Yannick Schwab, Rainer Pepperkok, John Briggs** and **Ralf Bartenschlager**, for the support they have given me throughout the years developing the project. Most importantly giving very valuable feedback on my project and critical discussions. I would like to thank **Rainer Pepperkok** and the **Pepperkok lab** for letting me participate in their lab meetings and giving me feedback to my automating CLEM project. It was very nice collaborating with **Nurlanbek Duishoev** setting up the CLEM pipeline for looking at a phenotypic Golgi (siRPGRIP1).

I am very thankful for the great collaboration with our industrial partner Zeiss, where **Robert Kirmse** has been our project manager. In the project automating our CLEM pipeline we had a lot of great help and input from **Heiko Stegmann** (Zeiss) and it would not have been possible without the work of **David Unrau, Ken Lagarec** and **Mike Holtstrom** from Fibics.

I would like to thank **John Lucocq** (University of St. Andrews) for letting me stay in his lab, giving me insights into stereology and giving me feedback throughout my PhD work.

I thank **Jean-Claude Tinguely** (Ahluwalia Lab, Department of Physics and Technology, University of Tromsø) who has been designing the waveguide chips and acquiring the light microscopy images. **Øystein Ivar Helle** (Ahluwalia Lab, Department of Physics and Technology, University of Tromsø) was kind enough to show me the waveguide imaging and has been also doing some waveguide imaging for our CLEM experiments. **Cristina Ionica Øie** (Optical Nanoscopy research Group, Department of Physics and Technology, University of Tromsø) showed me how to extract LSECs and performed all the extraction and immuno-

staining-procedures for the light microscopy experiments. I want to thank **Balpreet Singh Ahluwalia** (Department of Physics and Technology, University of Tromsø) who let me stay in his lab and who has given great feedback on the project. **Peter McCourt** (Vascular Biology Research Group, Department of Medical Biology, University of Tromsø) has given very important feedback for the biological part of this project. I am very grateful for all the work **Randi Olsen** (Advanced Microscopy Core Facility, Institute of Medical Biology, Faculty of Health Sciences, University of Tromsø) has put into the EM sample preparation on the electron microscopy side and she has provided helpful advice on preparing samples for the scanning electron microscope.

I want to thank **Shotaro Otsuka** (Ellenberg Lab, Cell Biology and Biophysics, EMBL Heidelberg) for pulling me into the world of nuclear pores and the reformation of the nuclear envelope. This project combined live cell imaging, EM tomography, FIB-SEM imaging, FCS measurements and 3D- reconstruction. It has been an amazing project, extending on the difficulties of 3D-EM and the very special needs of mitotic cells. I thank **Jan Ellenberg** (Cell Biology and Biophysics, EMBL Heidelberg) and his team for great feedback on the different aspects of the project and welcoming me in their lab meetings.

I would like to thank **Tom Boissonnet**, who has done the first step on working on setting up an automated segmentation pipeline for a high-pressure frozen cell using MIB. I want to thank **Anna Arcon Fernandez** who progressed on applying the automated MIB segmentation pipeline to other HPF cells. I would like to thank **Suruchi Sethi** who was brave enough to join our lab for six months and engage into the challenges of trying to automate segmentation. **Ilya Belevich** (MIB), as well as **Anna Kreshuk** (Ilastik) were a great help in advancing with the segmentation pipeline.

I want to thank **Sebastian Markert** (Stigloher Lab, University of Würzburg), who has not only provided samples, but has taught me how to handle *C. elegans* and to freeze/process them properly. It has been great developing the minimal resin embedding technique for the worms together with him. I want to thank **Christian Stigloher** (University of Würzburg), who made it possible to stay in his lab to learn how to culture *C. elegans* and prepare them for EM. **Sarah Tröger** (University of Würzburg) has taken up the challenge to model all the neurons in the (80 µm) dataset that I acquired of *C.elegans*. This has made it possible to start comparing the three datasets we have modeled. Through a wonderful collaboration with **Mei Zhen, Ben Mulcay** and **Daniel Witvliet** from Toronto, we got a deeper insight into the connectomics of *C. elegans.* Daniel helped me with his astounding knowledge about the anatomy of *C. elegans* to target the correct region in our 80 µm dauer head dataset.

I would like to thank the EMBL community, including the choir and the Science and Society committee, which I have spend some remarkable time with.

I want to thank my family, especially my mother, who has always been very supportive and giving me good advice. She has always encouraged my steps in life and I would not be here without her. I would like to thank my grandfather and my godmother for continuous encouragement and support. And finally, my amaazzing boyfriend Paule, who has supported and encouraged me since we met and especially throughout my PhD. He has been amazingly patient, especially for long working hours and sharing me with the microscope over the weekend. And of course, thank you so much for your wonderful feedback on my thesis.

Abstract

The need for quantitative analysis is crucial when studying fundamental mechanisms in cell biology. Common assays consist of interfering with a system via protein knockdowns or drug treatments. These very often lead to important response variability that is generally addressed by analyzing large populations. Whilst the imaging throughput in light microscopy (LM) is high enough for such large screens, electron microscopy (EM) still lags behind and is not adapted to collect large amounts of data from highly heterogeneous cell populations. Nevertheless, EM is the only technique that offers high-resolution imaging of the entire subcellular context. Correlative light and electron microscopy (CLEM) has made it possible to look at rare events or addressing heterogeneous populations. Our goal is to develop new strategies in CLEM. More specifically, we aim at automatizing the processes of screening large cell populations (living cells or pre-fixed), identifying the sub-populations of interest by LM, targeting these by EM and measuring the key components of the subcellular organization. New 3D-EM techniques like focused ion beam - scanning electron microscopy (FIB-SEM) enable a high degree of automation for the acquisition of high-resolution, full cell datasets. So far, this has only been applied to individual target volumes, often isotropic and has not been designed to acquire multiple regions of interest. The ability to acquire full cells with up to 5 nm x 5 nm x 5 nm voxel size (x, y referring to pixel size, z referring to slice thickness), leads to the accumulation of large datasets. Their analysis involves tedious manual segmentation or so far not well established automated segmentation algorithms. To enable the analysis and quantification of an extensive amount of data, we decided to explore the potential of stereology protocols in combination with automated acquisition in the FIB-SEM. Instead of isotropic datasets, a few evenly spaced sections are used to quantify subcellular structures. Our strategy therefore combines CLEM, 3D-EM and stereology to collect and analyze large amounts of cells selected based on their phenotype as visible by fluorescence microscopy. We demonstrate the power of the approach in a systematic screen of the Golgi apparatus morphology upon alteration of the expression of 10 proteins, plus negative and positive control.

In parallel to this core project, we demonstrate the power of combining correlative approaches with 3D-EM for the detailed structural analysis of fundamental cell biology events during cell division and also for the understanding on complex physiological transitions in a multicellular model organism.

Zusammenfassung

Der Bedarf an quantitativer Analyse ist entscheidend um die grundlegenden Mechanismen in der Zellbiologie und angrenzenden Disziplinen zu verstehen. Gebräuchliche Analysen bei denen in ein biologisches Testsystem mit Hilfe von Protein-Knockdown oder mit Behandlung von chemischen Substanzen eingegriffen wird, sorgen häufig für sehr unterschiedliche Phänotypen.

Diese Variabilität wird meistens an Hand der Analyse von großen Populationen studiert. Während die Bildgebung in der Lichtmikroskopie (LM) einen Durchsatz erreicht, der ausreichend ist um große Populationen zu analysieren, hinkt die Elektronenmikroskopie (EM) noch immer hinterher und ist nicht dafür angepasst viele Daten von sehr heterogenen Zellpopulationen zu akquirieren. Dennoch, EM ist die einzige Technik, die hochauflösende Bilder vom gesamten subzellulären Kontext aufnehmen kann. Die Kombination von Licht- und Elektronenmikroskopie (CLEM) hat es möglich gemacht seltene Ereignisse oder heterogene Populationen anzuschauen. Unser Ziel ist es, neue CLEM Strategien zu entwickeln. Im Einzelnen wollen wir den Screeningprozess großer Zellpopulationen um Sub-Populationen zu finden, das Wiederfinden im EM und das Quantifizieren von Schlüsselkomponenten der subzellulären Strukturen, automatisieren (lebende oder fixierte Zellen). Neue 3D-EM Techniken wie Rasterelektronenmikroskopie mit fokussiertem Ionenstrahl (FIB-SEM) machen es möglich ein hohes Niveau an Automatisierung für die Akquisition von hochauflösenden, die ganze Zelle umspannenden Datensätzen, zu erreichen. Bis jetzt wurde dies nur bei einzelnen Zielvolumen vorgenommen, meistens isotropisch und nicht dafür vorgesehen, dass mehrere Regionen aufgenommen werden. Die Fähigkeit ganze Zellen mit 5 nm x 5 nm x 5 nm Voxelgröße (x/y bezieht sich auf die Pixelgröße, z bezieht sich auf die Schnittdicke) aufzunehmen, führt zu einer Akkumulation von großen Datensätzen. Deren Analyse involviert mühsame manuelle Segmentierung und Quantifizierung von umfangreichen Datenmengen. Wir haben uns entschlossen die Möglichkeit zu untersuchen, stereologische Protokolle in Kombination mit einer automatisierten Akquisition im FIB-SEM zu verwenden. Anstelle von isotropischen Datensätzen werden einige wenige gleichmäßig verteilte Schnitte verwendet um sub-zelluläre Strukturen zu quantifizieren. Unsere Strategie verbindet deshalb CLEM, 3D-EM und Stereologie um große Mengen an Daten von ausgewählten Zellen (phänotypisch sichtbar im Fluoreszenzmikroskop) aufzunehmen und zu analysieren. Wir demonstrieren die Stärke unseres Ansatzes in einem systematischen Screen der Morphologie des Golgi Apparates nach

der Veränderung der Expression von 10 Proteinen, inklusive Negativ- und Positivkontrolle. Parallel zu diesem Kernprojekt demonstrieren wir die Möglichkeiten die korrelative Ansätze und 3D-EM bieten, um detaillierte Strukturanalysen von fundamentalen zellbiologischen Prozessen während der Zellteilung und komplexe Veränderungen in einem multizellulären Modellorganismus zu verstehen.

Table of Contents

Abbreviations

Abbreviation	Meaning
3D-EM	3-dimensional electron microscopy
ALMF	Advanced Light Microscopy Facility
ATUM-SEM	automated tape-collecting ultramicrotome - scanning electron microscope
BSA	bovine serum albumin
C. elegans	*Caenorhabditis elegans*
CLEM	correlative light and electron microscopy
COPI/COPII	coat protein complex I/II
CoV	coefficient of variance
DAPI	4',6-diamidino-2-phenylindole
ddH_2O	double distilled water
DMEM	Dulbecco's Modified Eagle's Medium
dSTORM	direct stochastic optical reconstruction microscopy
E. coli	*Escherichia coli*
e.g.	*example gratia*
EM	electron microscopy/electron microscope
EMCF	Electron Microscopy Core Facility
ER	endoplasmic reticulum
ERES	ER exit sites
EsB	Energy selective Backscattered

ET	electron tomography
EtOH	ethanol
FCS	fetal calf serum
FIB-SEM	focused ion beam - scanning electron microscope
FM	fluorescent microscopy/fluorescence microscope
FOV	field of view
GFP	green fluorescent protein
h	hour
HCMV	human cytomegalovirus
HeLa	cell line derived from cervical cancer cells from Henrietta Lacks
HIV	human immunodeficiency virus
HPF	high-pressure freezing
i.e.	*id est*
IM	imaging medium
KC	Kupffer cell
KD	knockdown
LM	light microscopy/light microscope
LMIS	liquid-metal ion sources
LN_2	liquid nitrogen
LSECs	liver sinusoidal endothelial cells
LSM	laser scanning microscopy
min	minute

ml	milliliter
mM	millimole
mm	millimeter
MTOC	microtubule-organizing center
MVB	multivesicular body
NA	numerical aperture
NE	nuclear envelope
NGM	nematode growth medium
NPCs	nuclear pore complexes
NUPs	nucleoporins
ORS	object research systems
PALM	photoactivated localization microscopy
PBS	phosphate-buffered saline
PHEM	PIPES, HEPES, EGTA, magnesium (buffer composition)
PIC	photonic integrated circuit
ROI	region of interest
RT	room temperature
SBEM	serial block-face electron microscopy
SDS	sodium dodecyl sulfate
sec	second
SEM	scanning electron microscopy/scanning electron microscope
SESI	Secondary Electrons Secondary Ions

SIM	structured illumination microscopy
siRNA	Small-interfering ribonucleic acid
siRPGRIP1	siRNA against Retinitis Pigmentosa GTPase Regulator Interacting Protein 1
ssTEM	serial section transmission electron microscopy
STED	stimulated emission depletion
STORM	stochastic optical reconstruction microscopy
TEM	transmission electron microscopy/transmission electron microscope
TIRF	total internal reflection fluorescence
TGN	trans-Golgi network
µl	microliter
µm	micrometer
U	unit
UA	uranyl acetate
UV	ultraviolet
VSNR	variational stationary noise remover
VTC	vesicular-tubular cluster

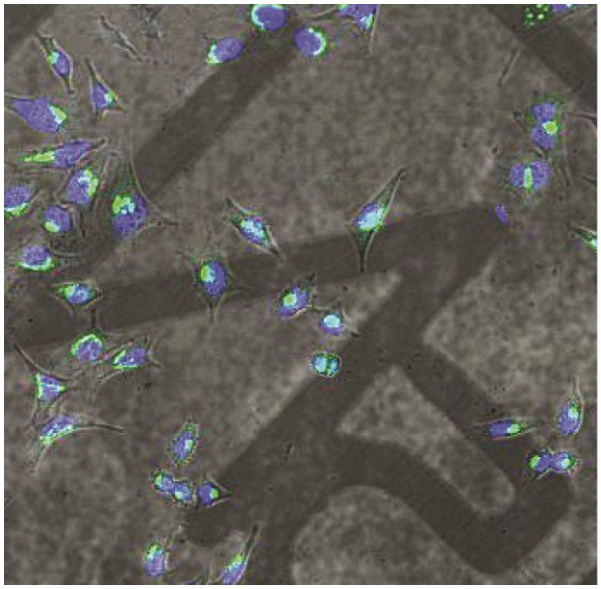

Chapter 1: Introduction

Cover image: Fluorescent image of HeLa cells (left: blue/DAPI, nucleus and green/GFP, Golgi signal) growing on a gridded-bottom culture dish. The coordinate system of the grid enable a precise targeting of the same cells inside the scanning electron microscope (right).

This thesis is about the development of new imaging methods for applications in life sciences. In particular, it integrates in the field of electron microscopy for cell biology, a discipline that has, at all ages, benefitted from improvements in techniques. My main interest lies on the development of correlative light and electron microscopy, a very powerful tool for synergizing functional and morphological studies in many biological systems. Moreover, I have strived to make use of volume EM, as a main mean for imaging the detailed ultrastructure in three dimensions. By developing new methods for the application of FIB-SEM in correlation with light microscopy, my goal was to drastically improve the throughput in data acquisition, leading to more quantitative information.

In the chapter 2, I will describe new strategies for *in toto* CLEM adapted to cultured cells. By automatizing the processes, the throughput in data collection can be drastically increased, thus enabling quantitative ultrastructural analysis on highly heterogeneous samples. The strategy elaborates on the combination of CLEM, 3D-EM and stereology to automatically collect EM data from large amounts of cells selected for their individual phenotype as visible by fluorescence microscopy. We decided to design our methods using one biological question focusing on the Golgi apparatus.
In preparation of a follow-up on this paradigm, I have been working on the adaptation to automated CLEM of a new super-resolution modality. In this very interdisciplinary project, I explored the possibilities to develop a workflow combining super-resolution microscopy on a photonics chip with CLEM and 3D-EM acquisition to look at endocytosis in liver sinusoidal endothelial cells (LSECs) (chapter 3).
In chapter 4, we have applied correlative workflows to analyze the reformation of the nuclear envelope and the nuclear pores during mitosis. The combination of high-resolution EM tomography and the acquisition of isotropic, full cell FIB-SEM datasets helped to elucidate the order of steps of nuclear envelope and nuclear pore reformation taking place through anaphase.
To further explore the potential of our 3D-CLEM methods, we developed an embedding method for *C. elegans* to be able to directly target specific regions within the organism inside the SEM. FIB-SEM datasets of the dauer larva stage were modeled to better understand the architecture and morphology of this specific stage (chapter 5).

The building blocks of this work belong to two technological fields: CLEM and FIB-SEM, a member of the 3D-EM family.

1.1 Correlative Light and Electron Microscopy

Even though it was not referred to as correlative light and electron microscopy (CLEM), the very first paper where a cell was imaged under a TEM was a *bona fide* CLEM experiment (Porter, Claude *et al.*, 1945). Indeed, these authors, who won the Nobel prize for their seminal work on the cell ultrastructure, were using a light microscope to first select the cells (chick fibroblasts) according to their shape and their potential for proper imaging by TEM. Upon such screen, the cells grown on a thin membrane of polymer (formvar) were detached from the culture dish and transferred to the EM grid for further study. In 1960 the combination of both techniques was used to look at the development of type 5 adenovirus (Godman, Morgan *et al.*, 1960). Until the 1990s the amount of papers reporting the use of CLEM was fluctuating around five papers per year, in the 1990s and early 2000s the amount increased to 15 – 30 and increased drastically since 2013 to 91 in 2016 (pubmed "CLEM" results by year). As a consequence of this, there has been an increasing number of technical variations on how to combine light and electron microscopy for the study of the same sample. One way to classify CLEM techniques is to consider, when in the sample preparation process the LM recordings are performed (Figure 1; de Boer, Hoogenboom *et al.*, 2015; Bykov, Cortese *et al.*, 2016; Spiegelhalter, Laporte *et al.*, 2014). Fluorescence imaging can be performed on living samples to follow for example the dynamic behavior of cells in a petri-dish or in an organism (Durdu, Iskar *et al.*, 2014; Goetz, Steed *et al.*, 2014; Karreman, Mercier *et al.*, 2016; Redemann and Muller-Reichert, 2013; Woog, White *et al.*, 2012). The ultrastructure of the selected cells is then studied in the EM using targeted approaches, which would rely either on the use of coordinate systems (for cultured cells) or on the anatomy of the specimen (for multicellular organisms or tissues). Besides these *in toto* CLEM approaches, there are very efficient methods that precisely identify the position of the fluorescent dye by screening the sample sections at the light microscope. Labeling a structure of interest can thus be done by applying affinity markers to the section (immunofluorescence), preserving the signals from genetically encoded fluorescent proteins (GFP, RFP, etc.), preserving signals from any fluorescent dye that could be applied to the living specimens, or during the sample preparation procedure. Such techniques can be referred to as on-section CLEM.

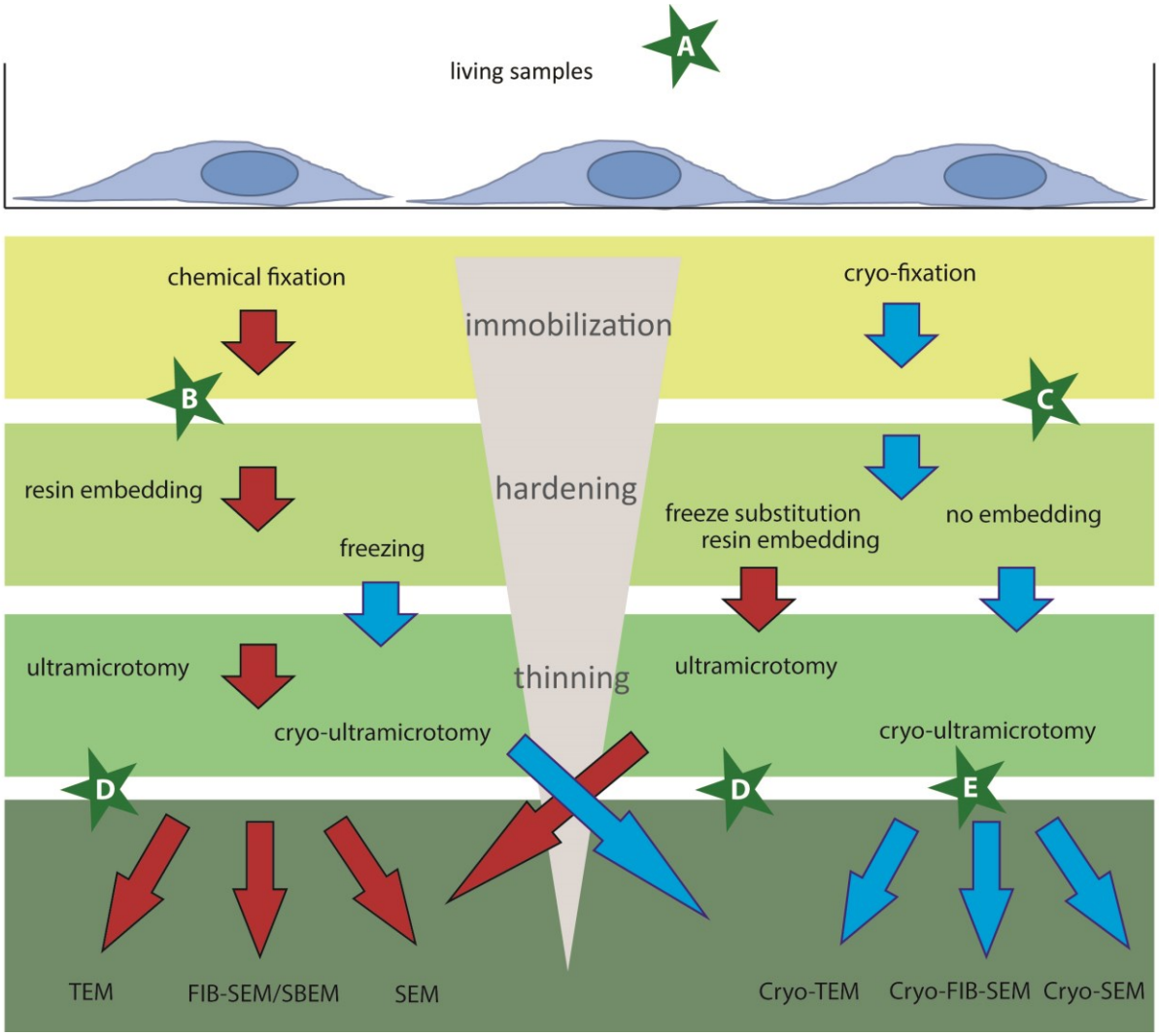

Figure 1: CLEM overview from a sample preparation point of view. This workflow shows how to prepare samples for electron microscopy including different types of CLEM. Green stars indicate steps where LM can be performed. A) LM is performed on living samples (van Rijnsoever, Oorschot et al., 2008; Spiegelhalter, Tosch et al., 2010; Kolotuev, Schwab et al., 2010). B) LM is performed after chemical fixation (Jimenez, Van Donselaar et al., 2010). C) On-section CLEM where either immunofluorescence and immunogold are correlated (Schwarz and Humbel, 2007; Karreman, Agronskaia et al., 2012) or the preserved signal from fluorescent probes is correlated with EM (Kukulski, Schorb et al., 2011; Watanabe, Punge et al., 2011). D) Fluorescence is inspected on embedded samples (Biel, Kawaschinski et al., 2003; Nixon, Webb et al., 2009). E) LM imaging is performed on vitrified samples or sections. The left side of the figure follows different routes for chemical fixation, whereas the right side follows cryo-fixation (Sartori, Gatz et al., 2007; Lucic, Kossel et al., 2007). Figure adapted from (Spiegelhalter, Laporte et al., 2014).

One major challenge when performing CLEM experiments is achieving a sufficient throughput in order to collect analyzable data. On-section CLEM approaches are probably the most efficient ones when it comes to acquiring information from multiple cells, because the screening is performed on large populations, and several events of interest can be selected from the same sections (Kukulski, Schorb *et al.*, 2012). Because many techniques are long and

tedious, most of the published papers rely on the study of a few specimens (Bumbarger, Riebesell *et al.*, 2013; Durdu, Iskar *et al.*, 2014; Goetz, Steed *et al.*, 2014). Hence, such approaches hardly lead to inter-specimen comparison or analysis. *In toto* CLEM was also performed on individual cultured cells in different projects for example looking at the formation of entotic cell-in-cell structures commonly observed in tumors (Russell, Lerner *et al.*, 2016). Other groups were looking at a novel molecular tether between late endosomes and the ER (Alpy, Rousseau *et al.*, 2013) or live cell dynamics in combination with 3D ultrastructure (Spiegelhalter, Laporte *et al.*, 2014).

My thesis work is about *in toto* CLEM, a set of techniques that still suffer from a low throughput. By improving the workflows and by using automated approaches for the correlation and/or for the imaging, the goal is to drastically improve their yield and efficiency.

1.2 Electron Microscopy in three dimensions

3D-EM techniques have been used early in the history of electron microscopy (Titze and Genoud, 2016) with applications on biological samples ranging from protein complexes to full organisms. At the high-resolution end of the scale in the field of structural biology, significant progresses have recently been made visualizing protein complexes. With the help of new detectors and new averaging techniques the boundaries have been pushed towards atomic resolution in the field of single particle analysis. In the last few years, single particle analysis has been utilized to extensively study many different topics ranging from virus particles to big protein complexes like the nuclear pore complex (Bartesaghi, Merk *et al.*, 2015; Schur, Hagen *et al.*, 2015; Hoelz, Glavy *et al.*, 2016). The new developments especially in cryo-electron microscopy, made it possible to expand the scope of research from individual molecular complexes to heterogeneous samples *in situ*, such as cells or tissues, with angstrom resolution (Zhou, 2011; Hoenger, 2014; Fernandez-Leiro and Scheres, 2016; Arnold, Mahamid *et al.*, 2016). The main advantage of cryo-EM over other techniques being the absence of chemical fixatives and other contrasting agents, leaving access to the native structure of macromolecules, hence to a close to atomic resolution. Nevertheless and especially when studying cells *in toto* and even more when working on tissues or full organisms, standard sample preparation techniques (chemical fixation, high-pressure freezing and freeze substitution) followed by room temperature EM are more accessible, hence routinely used for 3D-EM.

Serial sectioning of thin sections (50-100 nm) (Birch-Andersen, 1955; Bang and Bang, 1957) or thick sections (100 nm-1 µm) in combination with TEM tomography made it possible to reconstruct small cellular volumes in 3D. This was mainly used for subcellular parts of a cell (Marsh, 2005). The 3D information from individual sections was computationally reconstructed from a series (about 100) of 2D projections (TEM) taken at various tilt angles (typically ± 60°; Gilbert, 1972). One of the negative aspects of serial sectioning is the manual effort to cut and handle the sections, which takes time and is prone to error. Covering one full cell or even bigger volumes is time consuming and quite tedious. One example is the study on the model organism *C. elegans* which looked at the posterior nervous system using thousands of serial sections (Hall and Russell, 1991). A different way of preparing and looking at serial sections was published in 2006, array tomography and automated serial section collection (Hayworth, 2006). This technique is based on serial sections that are automatically collected on tape (automated tape-collecting ultramicrotome, ATUMtome (RMC)) and later on placed on silicon wafers, which can be imaged in a SEM (Schalek, 2012; Schalek, 2011). Although this method can handle large volumes and leaves open the possibility to re-image regions of interest, it still has to deal with distortions caused by the sectioning and the limited z resolution (Table 1) and so far has been mainly used in neuroscience (Kasthuri, Hayworth *et al.*, 2015; Mikula and Denk, 2015; Joesch, Mankus *et al.*, 2016). Envisioning to map the full mouse brain, the Lichtman lab has started looking at larger samples (Kasthuri, Hayworth *et al.*, 2015; Hayworth, Xu *et al.*, 2015) with array tomography and imaging on a multi-beam SEM. This method is able to acquire up to 91 fields of view at the same time. Already in 1981, the integration of an ultramicrotome inside a SEM was suggested to overcome the problems caused by manual serial sectioning (Leighton, 1981). In 2004, Denk built a serial block-face electron microscopy (SBEM) system, where a ultramicrotome was mounted inside the chamber of a scanning electron microscope and in which subcellular features were imaged directly from the exposed cross-sections at the resin block surface (Denk and Horstmann, 2004). Volume imaging was thus performed by automated slice and view iterations. Another form of volume imaging uses a focused ion beam to ablate thin resin layers instead of cutting off slices of material with a diamond knife. The focused ion beam - scanning electron microscope (FIB-SEM) was originally used in the semiconductor industry starting in the 1980s/90s as a tool to improve resolution of semiconductor fabrication. A couple of years later it was adapted to biological specimen for example to look at the internal morphology of small arthopods (Young, Dingle *et al.*, 1993). After the turn of the millennium a variety of topics were looked at with

FIB-SEM techniques from gland cells in crustacea (Drobne, Milani *et al.*, 2005a ; Drobne, Milani *et al.*, 2005b) to site-specific targeting in yeast and lymphoid tumor tissue (Heymann, Hayles *et al.*, 2006) or adult brain tissue (Knott, Marchman *et al.*, 2008). Wei and others demonstrated the removal of thin layers of yeast cells down to 3 - 4 nm, to expose the surface of the sample that is then imaged (Wei, Jacobs *et al.*, 2012). In the last couple of years a variety of topics and also a variety of tissues have been covered by FIB-SEM, from retina (Hoang, Kizilyaprak *et al.*, 2016) to podocytes in the kidney (Ichimura, Kakuta *et al.*, 2017; Burghardt, Hochapfel *et al.*, 2015) and skin (Cretoiu, Gherghiceanu *et al.*, 2015). Different groups looked at virus infected cells (Romero-Brey and Bartenschlager, 2015; Villinger, Neusser *et al.*, 2015; Earl, Lifson *et al.*, 2013; Milrot, Mutsafi *et al.*, 2016) and even used the FIB-SEM for the study of the nuclear pore complex (Hampoelz, Mackmull *et al.*, 2016). Each of the volume EM methods have positive and negative aspects (Briggman and Bock, 2012; Titze and Genoud, 2016) and would fit to specific projects. Parameters such as sample size, the region of interest to be acquired, x/y/z resolution and the time available dictate which method would be best to use. In comparison to serial sectioning TEM or SEM, SBEM and FIB-SEM techniques image the sample block surface and not individual sections, therefore distortions arising from cutting sections are negligible. This also makes image processing easier since only shifts in x/y can be assumed and therefore translational shift is sufficient for alignment.

Table 1: Comparison between 3D-EM techniques

	ssTEM	ATUM-SEM	SBEM	FIB-SEM	Single particle analysis
Fully automated acquisition	no	no	yes	yes	yes
Sections preserved for reimaging	yes	yes	no	no	yes
Staining	*En bloc* or on section	*En bloc* or on section	*En bloc*	*En bloc*	*on grid*
Achievable x/y pixel size (nm)	4	4	10	5	0.2 (resolution after averaging)
Achievable z resolution (nm)	40	30	25	5	0.2 (resolution after averaging)
Typical field of view (µm), without tiling	21	65	40	10	0.25
Acquisition time for a volume of 10 x 10 x 10 µm³ with voxel size (x, y, z) nm³	26 hours 3 x 3 x 70 *	23 hours 3 x 3 x 30	2 hours 10 x 10 x 25	39 hours 5 x 5 x 5	----
Operations for image stack alignment	Distortions and rotations	Distortions and rotations	Translational shift	Translational shift	----

* For the ssTEM a lot of time has to be spend after the acquisition in aligning the data

For my thesis work, I decided to exploit the potentials of the FIB-SEM

FIB-SEM systems, combining the capability of imaging with a precision machining tool, were developed as a result of the research on liquid-metal ion sources (LMIS) for use in space by Krohn in 1961 (Krohn, 1961; Krohn and Ringo, 1975). In the 1980s, the focused ion beam was commercialized as a tool used mainly in the semiconductor industry for methods of failure analysis, circuit repair and modification or lithographic mask repair (Orloff, Utlaut *et al.*, 1993). The FIB has four functions that can be used for different applications: imaging, milling, implantation and deposition. Accelerated ions can indeed be used to image sample surfaces at quite high-resolution, but being heavier than electrons, their landing energy is much higher and

result in sample damages. Therefore the FIB is rarely used for continuous imaging (hence the idea to combine the FIB within a SEM). Precisely this property, linked to the fact that ions are significantly larger than electrons (Yao, 2007), is used to remove material by expelling surface atoms (sputtering) at high-resolution. Accelerated ions (as well as electrons) can also be used to deposit material on the sample surface. This happens when the ions are colliding with a gaseous precursor that is vaporized above the surface of the sample. The energy of the ion is then transferred to the precursor molecule that lands on the sample surface. At high acceleration energies, the precursor molecules will penetrate the sample resulting in implantation of material. The combination of milling and depositing allows this machine to create almost every possible shape. It has been used for micromachining, preparing lamellas to visualize in a TEM or to expose cross-sections through material. Only within the last 10 years did the FIB-SEM technology begin to emerge as a widely used technique not only in the field of material science, but also in the life sciences (Cantoni and Holzer, 2014; Bassim, Scott *et al.*, 2014; Peddie and Collinson, 2014; Narayan and Subramaniam, 2015). In particular, the field of neurobiology has been pushing the limits (speed, volume) of FIB-SEM and SBEM systems to understand the wiring of the brain better (Hayworth, Xu *et al.*, 2015). Besides neurobiology, FIB-SEM has been instrumental to answer fundamental cell biology questions like the changes happening to human cytomegalovirus (HCMV) infected cells (Villinger, Neusser *et al.*, 2015) or how dengue virus perturbs the mitochondrial morphodynamics (Chatel-Chaix, Cortese *et al.*, 2016) and surface-connected tubular conduits in HIV-infected macrophages (Bennett, Narayan *et al.*, 2009). The FIB-SEM has also been used to look at whole eukaryotic cells with macromolecular resolution (Villinger, Gregorius *et al.*, 2012) as well as metastasizing tumor cells in brain biopsies (Karreman, Mercier *et al.*, 2016), the optic nerves of mice (Schertel, Snaidero *et al.*, 2013), or the blood vessel fusion in zebrafish (Armer, Mariggi *et al.*, 2009).

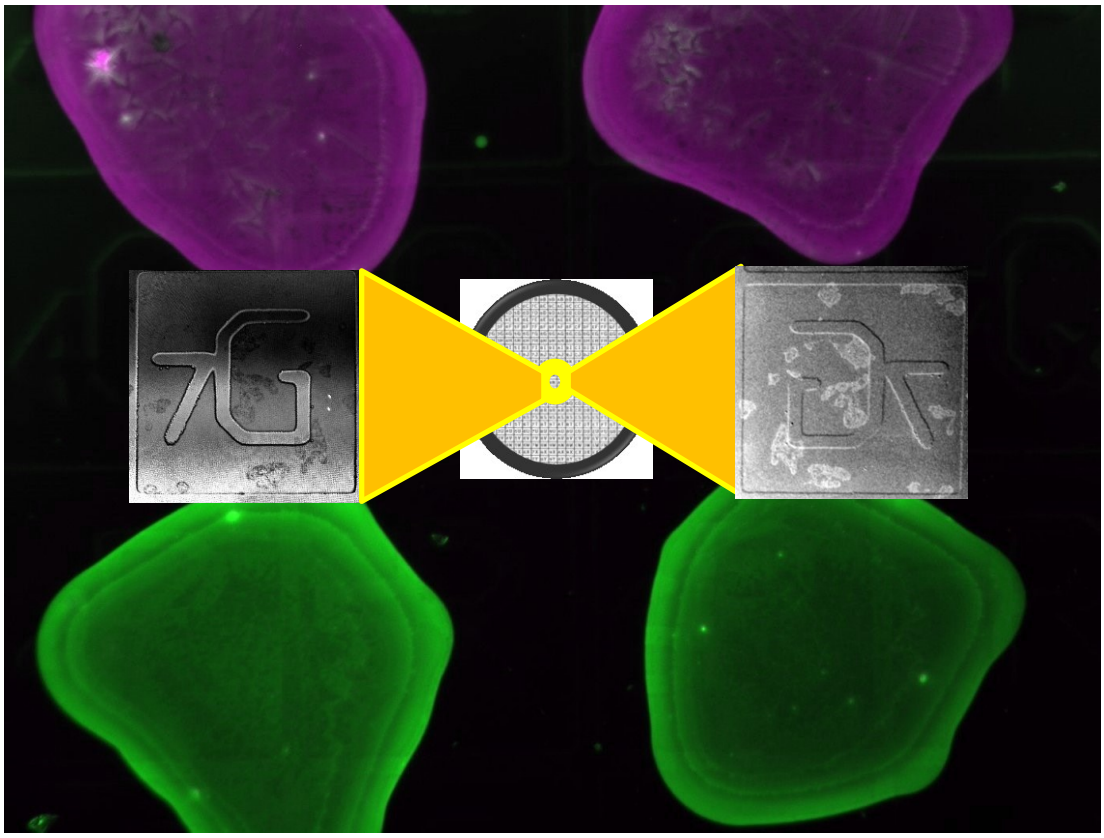

Chapter 2: Phenotypic screens using automated correlative light and electron microscopy

Cover Image: Fluorescently labeled gelatin spots containing siRNA. LM and EM image of the coordinate system.

The QR code is a link to the supplementary videos (#1), also available following this link: **http://tinyurl.com/Steyer-videos**

2.1 Introduction

The need for quantitative analysis is crucial when performing research on fundamental mechanisms in cell biology. Common assays consist of interfering with a system via protein knockdowns or drug treatments; these often lead to variable responses that need to be addressed at the level of populations (Figure 2).

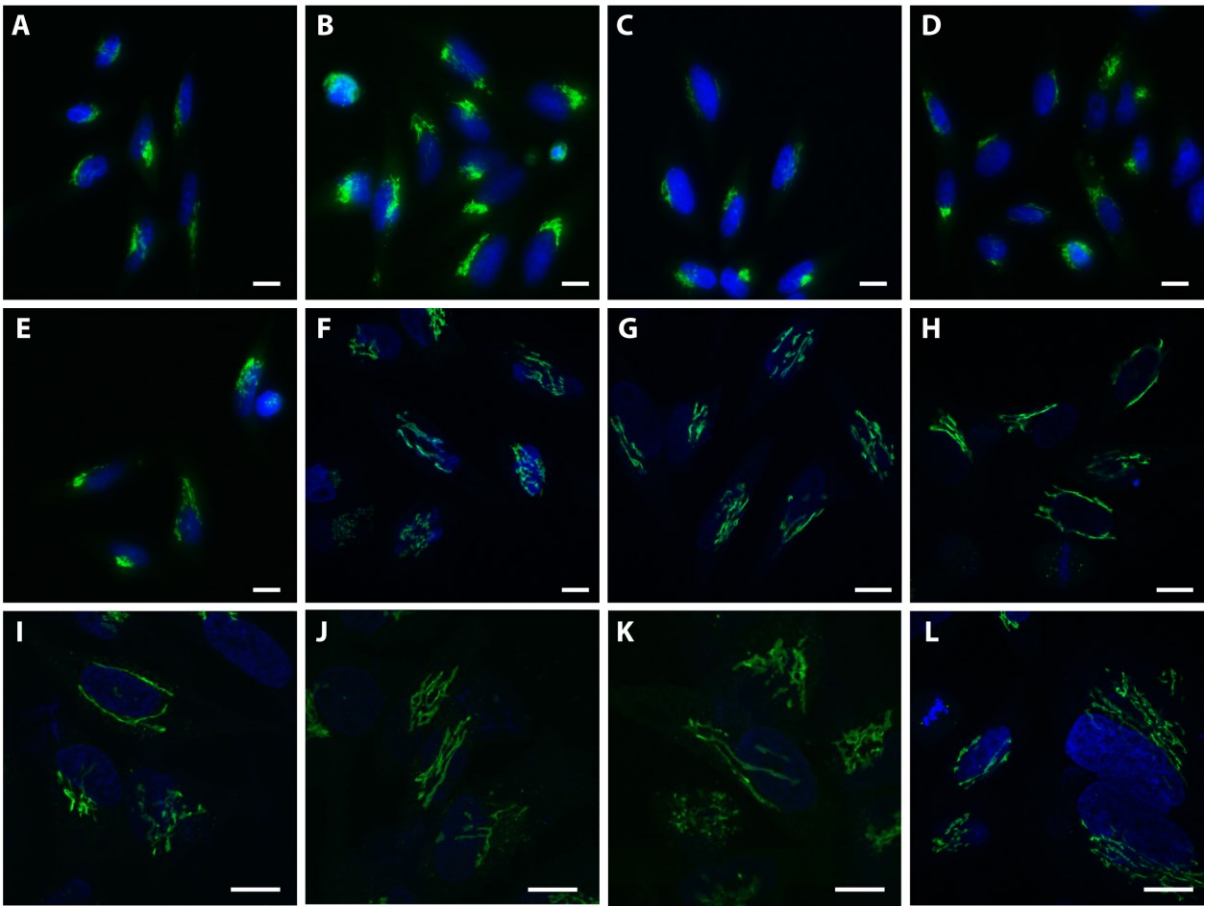

Figure 2: Heterogeneous reaction of cells to the same siRNA. Cells stably expressing GalNAc-T2-GFP were treated with siRPGRIP1 for 48 h before fixation, Golgi in green (GFP), nuclei in blue (DAPI). Various fields of view revealing a large heterogeneity for the morphology of the Golgi apparatus, varying from very condensed (A-E) to elongated (F-L); scale bar 10 µm.

For addressing such heterogeneity, light microscopy (LM) benefits from very large fields of view and from well-established protocols relying on automated functions. Thousands of recordings can therefore be achieved, leading to the ability to screen large populations for phenotypical changes (Simpson, Joggerst *et al.*, 2012). Electron microscopy (EM) on the other hand, even if not endowed with the same throughput, is the only technique offering high-resolution imaging for describing the complete subcellular organization. Looking at rare events

or addressing heterogeneous populations is made possible by correlative light and electron microscopy (CLEM).

Electron microscopy has undergone a renaissance within the last 10 years. Better, faster and easier techniques together with the possibility of combining different imaging modalities, have revived the interest to analyze samples from individual particles up to full organisms at nanometer resolution. Although big advances have been made in instrumentation and analysis when performing CLEM, the obligatory manual and tedious work limits the amount of data that can be acquired and quantified within a single assay. High-throughput acquisitions are standard in light microscopy, whereas electron microscopy is lagging behind. SBEM and FIB-SEM has made it possible to automatically section/mill and acquire hundreds of images throughout a region of interest. FIB-SEM is a powerful tool to get 3D information and offers the precision to image selected cells. However, since most biological samples are not homogeneous, for proper analysis of specific cells/regions, correlative light and electron microscopy is required. The combination of both techniques thus reveals rare events in the light microscope and looks at them at high-resolution in the EM (Figure 3).

In my PhD project, I have been combining a CLEM workflow to screen for specific phenotypes and then take advantage of the possibility to automate the FIB-SEM acquisition. The result is a CLEM pipeline, where we are able to select cells based on fluorescence microscopy and acquire multiple fields at high-resolution by EM. Since this would be a screening tool utilizing CLEM, both LM and EM had to be optimized. High-throughput screenings have been regularly used in the Advanced Light Microscopy Facility (ALMF, EMBL Heidelberg) (Erfle, Neumann *et al.*, 2007). These rely on siRNA libraries to screen for effects by knocking down certain proteins; however it has never been adapted to CLEM. Similar to what has been developed for high-throughput LM screens, we have integrated multiple knockdown conditions by spotting up to 32 siRNAs in one petri dish (Figure 6). The next step was to implement a feedback microscopy pipeline in order to analyze every single treatment at the LM level and to select phenotypic cells. Further automation enabled us to collect the necessary positional information to navigate in the FIB-SEM and acquire EM images of each one of the selected cells.

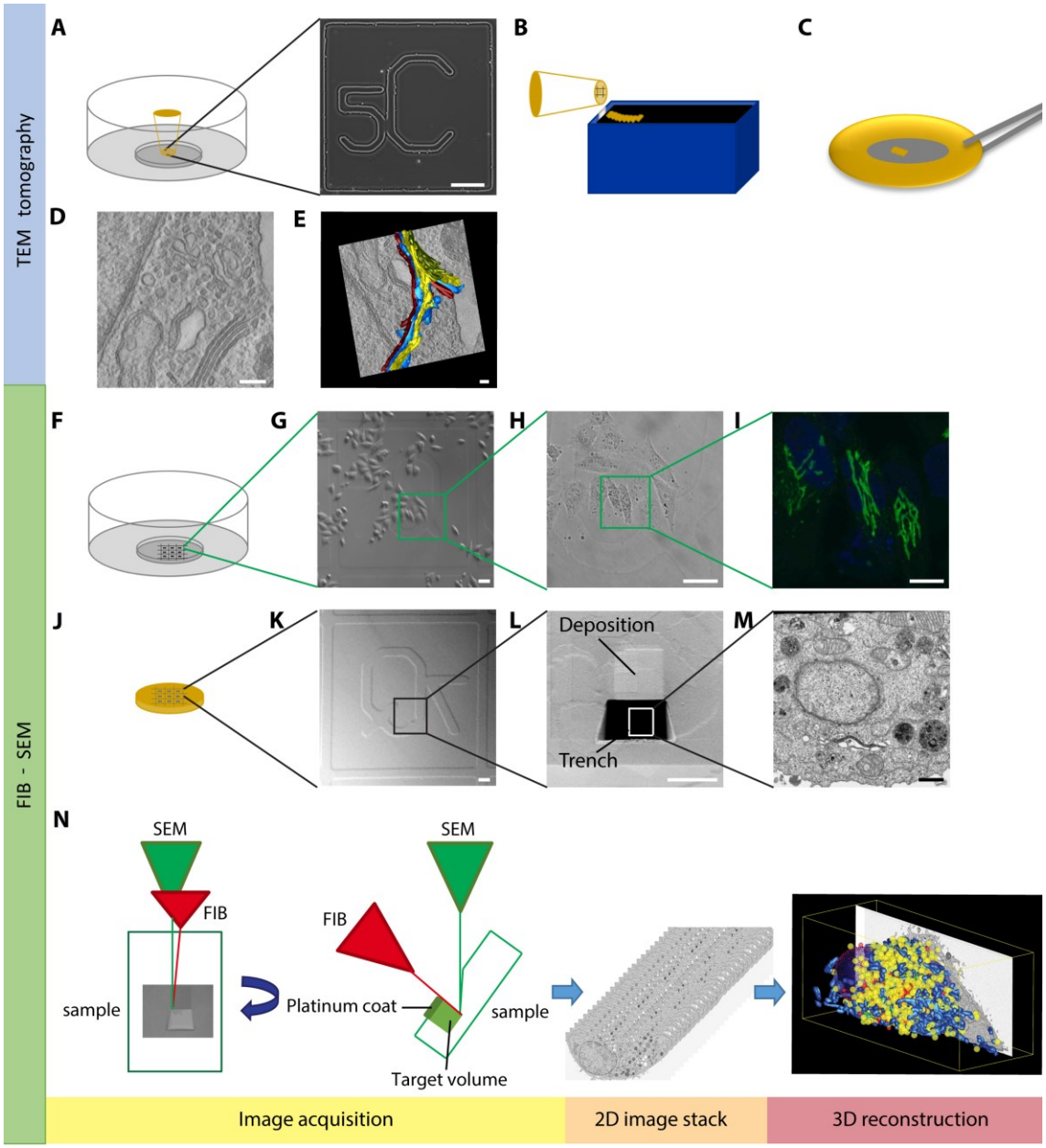

Figure 3: CLEM workflow for TEM tomography and FIB-SEM. A) Cells are grown on a gridded petri dish (MatTek, USA) that has a coordinate system for recording the positions of cells (scale bar 100 µm). To perform TEM tomography, sections of the selected region of interest are produced with a diamond knife (B) mounted on an ultramicrotome. C) Sections are collected on slot grids. D) TEM tomography (scale bar 200 nm), reveals the fine ultrastructure of organelles (*e.g.* Golgi cisternae), that can be modeled by manual segmentation (E); scale bar 150 nm. F) Cells are grown on gridded MatTek dish. To find back the same cell in the EM as in the LM, an overview image is acquired, G) 10x transmitted light (scale bar 20 µm). More detailed images of the cell of interest are acquired, H) 20x transmitted light (scale bar 20 µm), I) 63x fluorescence microscopy (405 and 488 nm; scale bar 10 µm). After EM processing the resin disk including cells is introduced into the FIB-SEM (focused ion beam-scanning electron microscope), J) disk with cells for SEM imaging. The surface of the sample is imaged K) SESI detector; scale bar 20 µm. To expose the sample and protect it while acquiring images, L) trench and deposition layer are done; scale bar 20 µm. M) Cross-section through cell (scale bar 500 nm). 3D imaging of biological samples inside the FIB-SEM. N) Set-up of FIB-SEM for image acquisition to acquire a stack of 2D images, which are used to either create a 3D-model or for sampling based quantification (Stereology).

2.1.1 The Golgi Apparatus

The Golgi apparatus has first been described in 1898 by Camillo Golgi from observations with a light microscope. The first ultrastructural information was revealed in the 1950s by EM (Dalton and Felix, 1954; Farquhar and Rinehart, 1954). Since the Golgi does not fit into a single 100 nm thick section, other techniques had to be used to visualize its full 3D-structure. In 1974 high voltage TEM and stereoscopy (EM section photographed at two distinct angles, after which the pairs were viewed with a stereoscope) were introduced to get 3D insights of the Golgi elements from 1 µm sections (Rambourg, Clermont *et al.*, 1974). Similar consecutive work contributed to the understanding of the fine architecture of the Golgi using an ultra-high voltage TEM (1 MeV) (Lindsey and Ellisman, 1985; Clermont, Rambourg *et al.*, 1995). As an alternative, different studies were carried out using serial thin sections (Beams and Kessel, 1968; Dylewski, Haralick *et al.*, 1984). In the 1990s, 3D-EM advanced significantly due to the possibility of high-voltage dual-axis tilt TEM tomography (Penczek, Marko *et al.*, 1995; Mastronarde, 1997), which allowed the analysis of thicker sections with high x/y resolution (Klumperman, 2011; Marsh, 2005; Noske, Costin *et al.*, 2008). Functional differences within the Golgi stack revealing the cis-trans-polarity were found by enzyme-activity-based cytochemical staining (Farquhar and Palade, 1981). The possibility to localize different proteins with antibodies also in EM made it possible to determine the location of the cytoplasmic coat complexes (Rabouille and Klumperman, 2005). Different protocols were developed to combine 3D-EM and protein localization (Trucco, Polishchuk *et al.*, 2004; Grabenbauer, Geerts *et al.*, 2005). To be able to combine time resolved information and ultrastructural information, light and electron microscopy was combined on the exact same sample (Mironov, Polishchuk *et al.*, 2008; van Rijnsoever, Oorschot *et al.*, 2008). From all of these different techniques a general knowledge of the mammalian Golgi organization has emerged (Griffiths, Quinn *et al.*, 1983; Quinn, Griffiths *et al.*, 1983; Griffiths, Pfeiffer *et al.*, 1985; Griffiths, 2000). It consists of stacked, disk-like membranes, called the cisternae, which are stretched longer in one direction than the other. In mammalian cells, there is a range of 4-11 cisternae (Rambourg, 1997) with a width of 0.7-1.1 µm (Rabouille, Misteli *et al.*, 1995; Pelletier, Stern *et al.*, 2002) and a membrane spacing of 10-20 nm. All cisternae are fenestrated with holes up to 100 nm in diameter (Klumperman, 2011). Studies in insulin producing β cells in mice estimated the volume of the Golgi to be 3.7-5.8 µm³, whereas the Golgi stack itself was counting 3.1-3.6 µm³ (Noske, Costin *et al.*, 2008). Besides the cisternae, the Golgi stack contains up to 2000 small vesicles, (Marsh, Mastronarde *et al.*, 2001). According to the enzyme

content and the orientation within a cell, the cisternae can be divided up into cis, medial and trans (Figure 4), whereas the maturation follows a cis-trans directionality (Glick and Luini, 2011). Importantly, the shape, size and volume of the Golgi stack changes depending on the cell type (Rambourg, 1997), the physiological conditions (Lee and Linstedt, 1999; Glick, 2000) and throughout the cell cycle (Lucocq, Berger *et al.*, 1995).

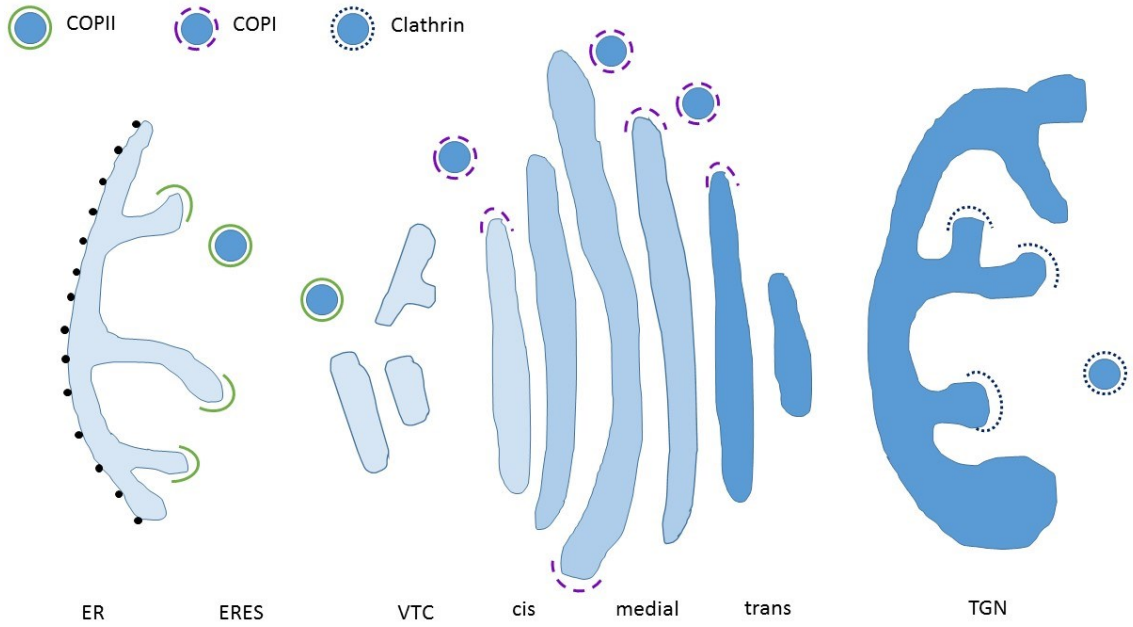

Figure 4: Schematic representation of the Golgi and associated membrane networks. (Based on (Klumperman, 2011)). Overview of the Golgi stack in relation to ER exit sites (ERES), vesicular-tubular clusters (VTCs) and trans-Golgi network (TGN) and the occurrence of COPII, COPI, and clathrin coated vesicles. Membranes are drawn as if cross-sectioned in side view.

Mammalian cells contain multiple Golgi stacks which are interconnected by a network of tubules forming the Golgi ribbon. Although lower animal cells and organisms can form Golgi stacks, they remain separated and are not interconnected (Kondylis and Rabouille, 2009). Even eukaryotic lineages lacking any morphologically recognizable Golgi still contain conserved Golgi proteins (Dacks, Davis *et al.*, 2003). The cis-side of the Golgi receives cargo from the ER, whereas the trans-side passes cargo to other distinct locations in the cell. The localization of the Golgi ribbon in the perinuclear region around the microtubule organizing center (MTOC) is closely relating the maintenance of Golgi structure and the cytoskeleton (Thyberg and Moskalewski, 1985; Goud and Gleeson, 2010). Newly synthesized proteins made for secretion or intracellular destinations enter the secretory pathway by translocation via the endoplasmic reticulum, using membrane-bound carriers which bud at distinct ER exit sites (ERES) mainly

located facing the cis-Golgi (Griffiths, Pepperkok *et al.*, 1995). Adjacent to the ERES are vesicular-tubular clusters (VTCs) which supply small amounts of tubulovesicular membranes to the cis-Golgi (Klumperman, 2000). After proteins have passed through the Golgi they are received by the trans-Golgi network (TGN), which sorts and shuttles proteins and lipids to different locations within the cell (Griffiths and Simons, 1986; De Matteis and Luini, 2008; Mellman and Simons, 1992). COPI coated vesicles are the carriers for intra-Golgi transport and retrograde transport from the Golgi to the ER. COPII mediates the export from the ER to either the ER-Golgi intermediate compartment (ERGIC) or the Golgi (Bonifacino and Glick, 2004). Clathrin-coated carriers are part of the anterograde transport mechanism from the TGN.

Despite intense and continuous research on this organelle since Camillo Golgi, there are still some open questions concerning the relationship between its morphology and function. For a complete review on the ultrastructure of the Golgi apparatus, refer to the article by J. Klumperman (Klumperman, 2011).

2.2 Results

2.2.1 Applying CLEM to measure the Golgi apparatus from selected cells

A pilot experiment performed in collaboration with Nurlanbek Duishoev (at the time of the experiments, Pepperkok lab, EMBL Heidelberg) demonstrated the importance of EM to study the consequences of protein knockdown (KD) on the phenotype of the Golgi apparatus, and how EM and furthermore CLEM are necessary to understand the complex morphology of this organelle. A specific phenotype of the Golgi organization was selected and analyzed by fluorescence microscopy. The cells treated with siRPGRIP1 (Retinitis Pigmentosa GTPase Regulator Interacting Protein 1) showed an elongation of the Golgi visible in the LM. The study of RPGRIP1 revealed that the depletion of RPGRIP1 lead to decreased centrosomal nucleation of microtubules and increased microtubule stability, which lead to Golgi reorganization (PhD thesis Nurlanbek Duishoev). Due to the limited resolution, it was not clear what the underlying ultrastructure and possible changes of the architecture of the cell would be (volume, stack composition, mini stacks, etc.). Therefore, we decided to investigate the ultrastructure of these elongated Golgi with EM, after selecting them with LM. Whereas the elongation of the Golgi ribbon was obvious at the LM level, fluorescence microscopy was not sufficient to reveal potential modifications of the Golgi intimate structure hence the need for a study at the EM level. After sample processing and targeting with CLEM (Figure 3 F to N), the selected cells were recorded by electron microscopy. One important observation in such experiment with siRNA is that although all cells were treated with the same siRNA they showed highly heterogeneous phenotypes. The elongation of the Golgi ribbon was the most prominent consequence of the KD, as revealed by unbiased image analysis. Nevertheless, other phenotypes were visible, ranging from normal to diffues, condensed, tubular and fragmented. One of the reasons for this diversity could be a variable transfection efficiency of the cells, an effect of the cell stage or intrinsic intercellular heterogeneity. Conventional EM investigation of an organelle morphology would emphasize the need for random, unbiased selection of the cells to be imaged (Lucocq, 1993; Gundersen, 1986; Lucocq, 2008). On such heterogeneous populations, a random approach would require an important survey through a large population of cells. If one would be interested to analyze multiple siRNAs, the very low throughput of such analysis would for sure preclude the use of EM. Therefore it was crucial to use CLEM to target specific sub-populations showing the elongated phenotype.

To correlate LM and EM on cultured adherent cells, we took advantage of the commercially available culture dish with a gridded coverslip (MatTek, P35G-2-14-C-GRID). This coordinate system is visible at the LM level, and because of its topology (the grid is etched at the surface of the coverslip) leaves an imprinted mark at the surface of the resin block after preparing the cells for EM (Figure 3 K). Volume acquisitions were first assessed by TEM tomography (Figure 3 A to E). At least 3 to 4 serial sections (300 nm thick) were necessary to cover one single Golgi stack in Z. On each section, tile acquisitions were necessary to cover the stack surface, at an adequate magnification (9400x-12000x). Therefore only a combination of stitched tiles and serial tomograms allowed the acquisition of a volume of about 2 μm^3 at a satisfying x/y resolution (1 nm/pixel) (Marsh, 2005). In figure 3 E, three serial tomograms were necessary to image a portion of a Golgi stack. The volume imaged is approximately 1 μm^3. The total time necessary for such analysis (acquisition, computing and segmentation) was about 1.5 weeks. We then performed the same correlative approach using automated serial imaging in a focused ion beam - scanning electron microscope (FIB-SEM) to aquire an isotropic dataset (Figure 3 F-M). This was done on control cells (n=3) and on cells with a protein knockdown (siRPGRIP1, n=3). The volume of the Golgi apparatus was extracted from the datasets via manual 3D modeling (control: 6 μm^3, knockdown 15 μm^3). Even though isotropic datasets are essential to analyze the connectivity of the organelles in the volume of the cell, *i.e.* here the Golgi ribbon, they suffer from a very low throughput: 9 weeks for 6 cells. Alternative approaches were sought to increase the speed of ultrastructural assessment. As explained later, stereology seems to be the most efficient solution so far (2.2.5).

2.2.2 Spotting siRNA on gridded dishes and automatically analyzing phenotypes

Large-scale phenotypic screens have been developed for investigating at the LM level the effects of siRNA on the Golgi apparatus morphology (Simpson, Joggerst *et al.*, 2012). We set out to adapt this strategy to our automated CLEM workflow in order to analyze multiple knockdowns in the same experiment, and to address efficiently the phenotype heterogeneity observed for many treatments (Figure 5). The principle of the screen would be to first perform automated LM to acquire multiple fields of view for every siRNA, to then conduct systematic image analysis on every imaged cell, in order to describe the changes in the Golgi morphology. Such analysis would identify morphological classes (fragmented, condensed, tubular, and diffuse) as shown in Figure 5. Our strategy is to then select cells from some of these classes to trigger the automated workflow as described below.

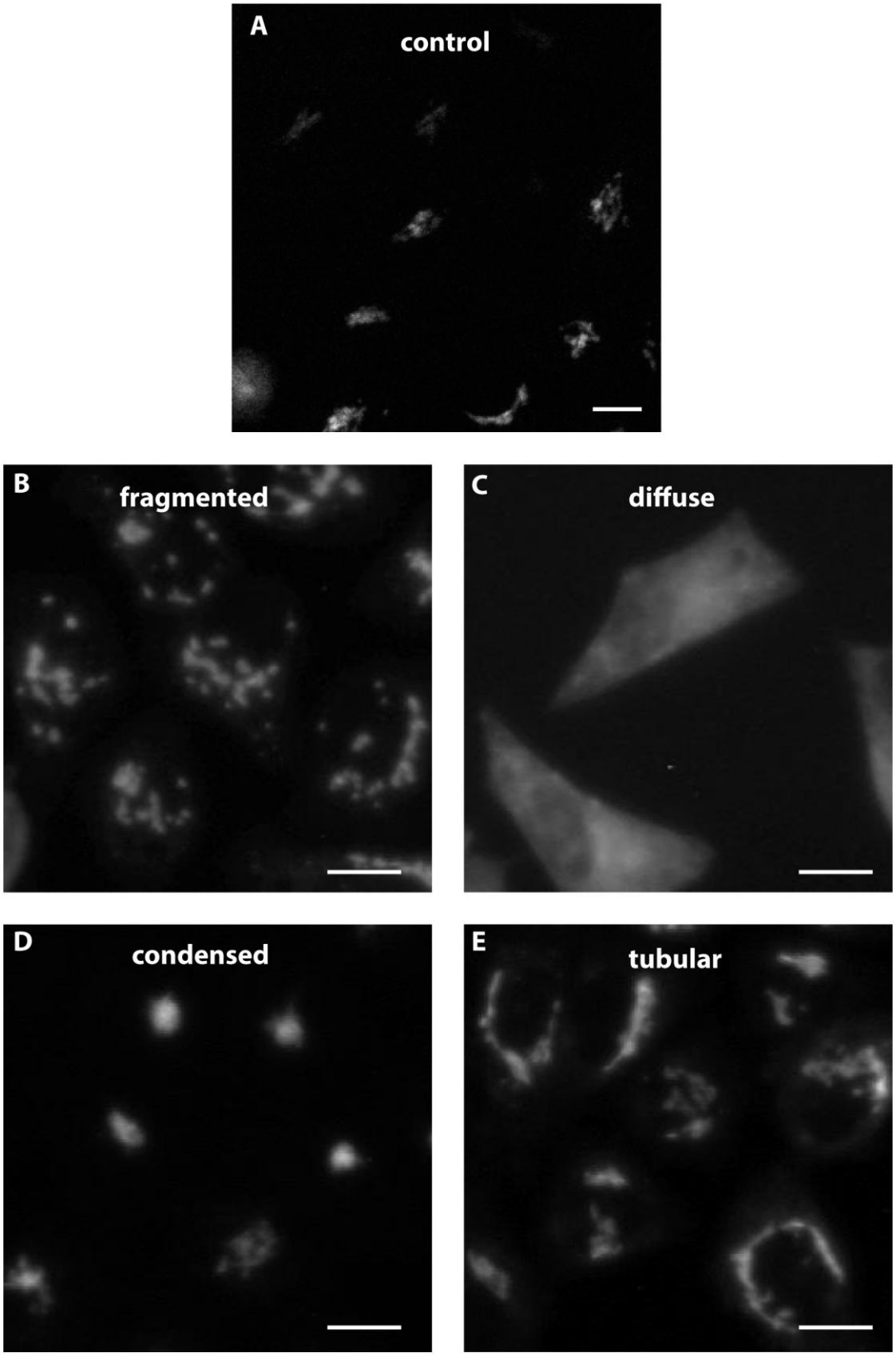

Figure 5: Representative images of the different phenotypes. A) Control Golgi (Neg9 knockdown); scale bar 5 µm. B) Fragmented Golgi; scale bar 10 µm B) Diffuse Golgi; scale bar 10 µm. C) Condensed Golgi; scale bar 10 µm. D) Tubular Golgi apparatus in GalNAc-T2-GFP cell line; scale bar 10 µm.

In collaboration with the ALMF, we developed a workflow where 32 individual siRNA were spotted on one MatTek dish. The different spots were labeled with gelatin coupled either to Oregon green 488 or Alexa 594 (Figure 6) to drive the systematic acquisition of individual fields of view. Three corners of the spot array were labeled in green and one in red, these were used to calibrate the positions of the other spots that were then pre-scanned. The acquired pre-scan images were analyzed in CellProfiler to extract different features of all cells, looking especially at the shapes of the nucleus and the Golgi apparatus. The image analysis was designed to select cells with the strongest phenotype representing the characteristics of the individual treatments. The cell positions were then transferred back to the confocal microscope, which automatically acquired high-resolution images of the target cells (40x z-stack, DAPI, GFP, Alexa 594) and lower magnification images to record the surrounding context of the cells, including the landmarks etched at the bottom of the culture dish (10x, DAPI, GFP, Alexa 594, transmitted and reflected light). For each image, the stage positions were recorded.

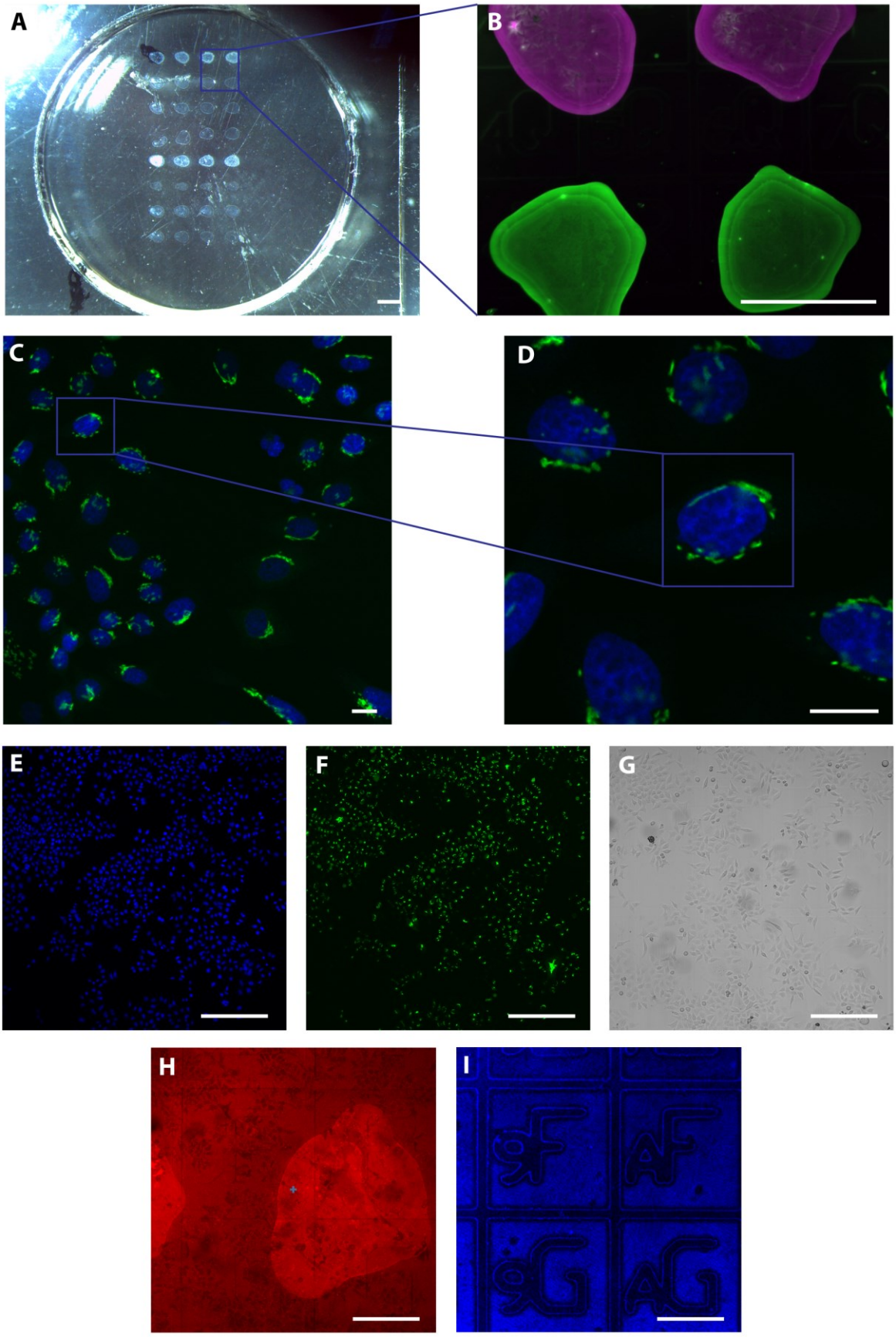

Figure 6: Spotted dishes and cells after 48 h knockdown of DNM1.

Figure 6 (previous page): A) Dry MatTek dish after spotting 4 x 8 (transmitted light), B) dry fluorescent labeled spots red recolored in magenta (gelatine coupled to Alexa 594 and gelatine coupled to oregon green 488); scale bar 1 mm. C) Prescan 10x image with selected cell; scale bar 20 µm. D) Average intensity z-stack selected cell; scale bar 10 µm. 10x images of E) Dapi, F) GFP, G) transmitted light, H) Alexa 594 and I) reflected light; scale bar 300 µm.

2.2.3 Image analysis of Golgi phenotypes

Using an adaptive feedback microscopy workflow (Tischer, Hilsenstein *et al.*, 2014), cells on the different siRNA spots were automatically imaged at low magnification. A small number of cells (3-5) representative for each siRNA treatment were identified using statistical image analysis, and the identified cells were re-imaged with scan settings at higher magnification as well as scan settings that show the location of the cell with respect to the spatial reference grid. All light microscopy imaging were performed on a motorized Leica SP5 confocal microscope (Leica Microsystems, Wetzlar, Germany) using 10x (Leica NA 0.4, dry UV) and 40x (Leica HCX APO U-V-I, NA 0.75, dry) objectives and the Leica HCS A software, known as Matrix Screener (Leica microsystems, Germany). The detailed light microscopy workflow proceeds as described in the methods section (2.3.4). Pre-scan images were analyzed using CellProfiler (Carpenter, Jones *et al.*, 2006). The cellular features computed with CellProfiler were further analyzed using custom scripts (https://github.com/tischi/HTM_Explorer) written in R (R Development Core Team, 2008). As a next step, we performed a z-score normalization of the four Golgi features, *i.e.* for each feature value we subtracted the mean and divided by the standard deviation of all cells subject to the negative control treatment. Each cell was characterized by a "morphological vector" that is comprised of four normalized features (looking at diffuse, condensed, fragmented and tubular elements of the Golgi).

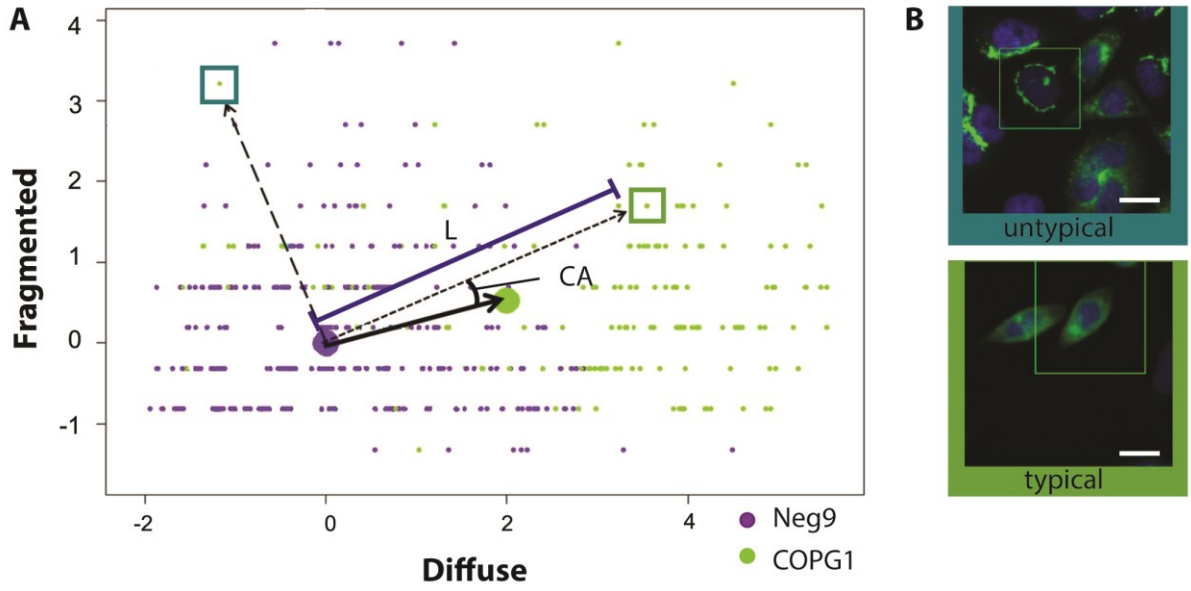

Figure 7: Image analysis finding typical cells for each treatment. Two morphological features were chosen to show the analysis diffuse and fragmented distribution of the GFP signal. A) Diagram showing diffuse and fragmented score for every cell. The length of the vector L for every cell characterizes how different the cell is to the negative control. The cosine of the angle CA between the average vector and the vector for the individual cell describes how typical the cell is for the treatment. B) Examples for untypical and typical Golgi; scale bar 10 µm.

The length L of each vector characterizes how "unusual" the Golgi of this cell appears relative to control cells (Figure 7). To further characterize the morphological changes induced by the different treatments, we computed the mean vector of all cells subjected to the same treatment. By construction, the mean vector of the negative control cells is (0, 0, 0, 0), whereas for the different treatments this vector points into the direction of the morphological changes that are typical for this treatment. Finally, for each cell we computed the cosine of the angle (CA) between the cell's morphological vector and the mean vector of the respective treatment. CA is +1 if the morphological changes of the cell point in the same direction as the treatment average and -1 if they point in the opposite direction. Combining L and CA we now have a mean to automatically select cells showing strong morphological changes (large L) that are typical (CA ~ +1) for a given treatment. In our experiments we only used selected cells with L>2.2 and CA>0.7 (Figure 7), based on thresholds set by manual inspection.

In summary, our image analysis gives us a library of cells corresponding to the different conditions that are then further analyzed by EM. Besides the detailed information of the cells, we collect low magnification images of the cellular context to be able to target the cells in the EM.

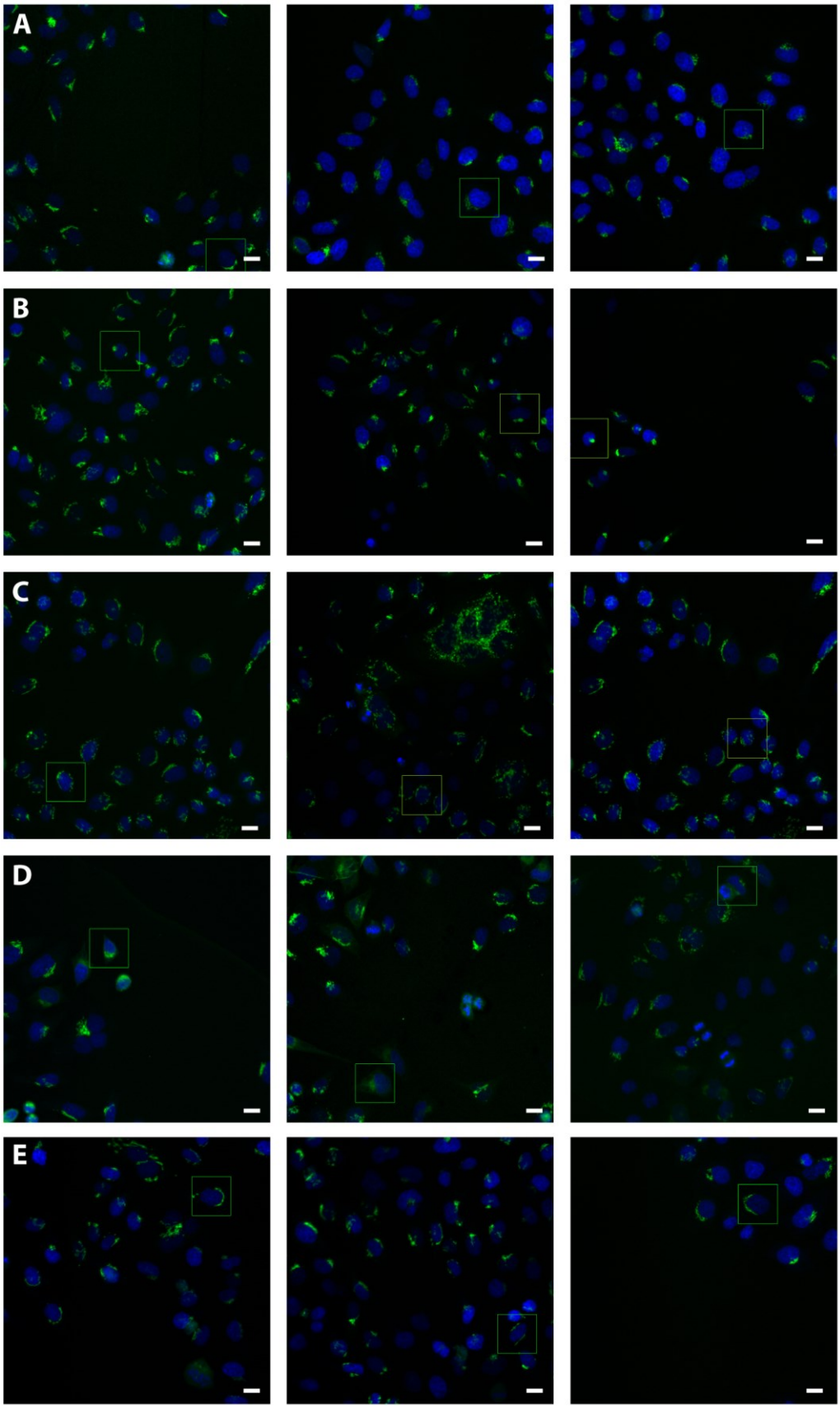

Figure 8: Phenotypic cells selected by the image analysis pipeline. Automatically selected cells on pre-scan images (10x objective) after 48 h of siRNA knockdown, A) Neg9 (control), B) C1S, C) DNM1, D) COPG1, E) ARHGAP44; scale bar 10 µm.

2.2.4 Automation strategy CLEM

CLEM is a very efficient way to select specific cells and to measure with high precision many features, for example, size, volume or stack composition of the Golgi apparatus. Nevertheless, manual approaches are tedious and time-consuming, and are usually addressing one cell at a time. New 3D-EM techniques like focused ion beam - scanning electron microscopy (FIB-SEM) make it possible to automate the acquisition of high-resolution datasets. So far this has only been applied to individual target volumes (Russell, Lerner *et al.*, 2016), often isotropic and has not been designed to acquire hundreds of regions of interest. As the study of one cell requires on average 10 days, it does not allow large population studies. To improve the throughput of our approach, we are developing ways to automate the data collection (Figure 9). Besides acquiring high-resolution images (z-stack) of our cell of interest, overview images showing the neighboring cells and the coordinate system (reflected light) were acquired. We then processed the sample for electron microscopy and used the MSite program to register our reference points in the SEM. Identifying the position of a cell of interest on a gridded coverslip is not a complex task, but automating this step is a prerequisite for programming automated multi-site acquisitions. Those points were found by using a line detection algorithm. The center points of the intersecting lines from the coordinate system were used as reference points. After acquiring the same reference points in the SEM (Figure 10), with the help of a transformation matrix, we could predict the position of selected cells in the SEM. This was done using a program (MSite) developed by José Miguel Serra Lleti (PhD student in Schwab team; EMBL Heidelberg).

Global as well as local strategies were applied to target as precisely as possible to the selected regions of interest (Figure 10 B). With global registration (the reference points are spread throughout a surface area of 1 cm^2) a targeting-accuracy of 30 to 50 µm could be reached. Using local reference points (in a field of view of 3 mm^2) an accuracy of less than 5 µm was achieved (Figure 10 B). The latest was expected to be precise enough to hit the cell of interest, but not enough for targeting subcellular structures. For this we are exploring the incorporation of further image analysis into the registration process. Following the transformation of the LM and SEM coordinates to find the position of our cells of interest, the samples were automatically prepared for a stereological, non-isotropic acquisition (as described below). The automated run is a succession of key functions that are normally achieved manually by interfering with the operating interface of the FIB-SEM. We had to programmatically take over the control of the machine to achieve a fully unattended run through the acquisition procedure

(Figure 9). When one task is completed, our application drives to the next cell and triggers a new acquisition. By doing so, each cell that has been selected at the light microscopy level can be retrieved automatically by the FIB-SEM. The image stacks are stored for further processing and analysis.

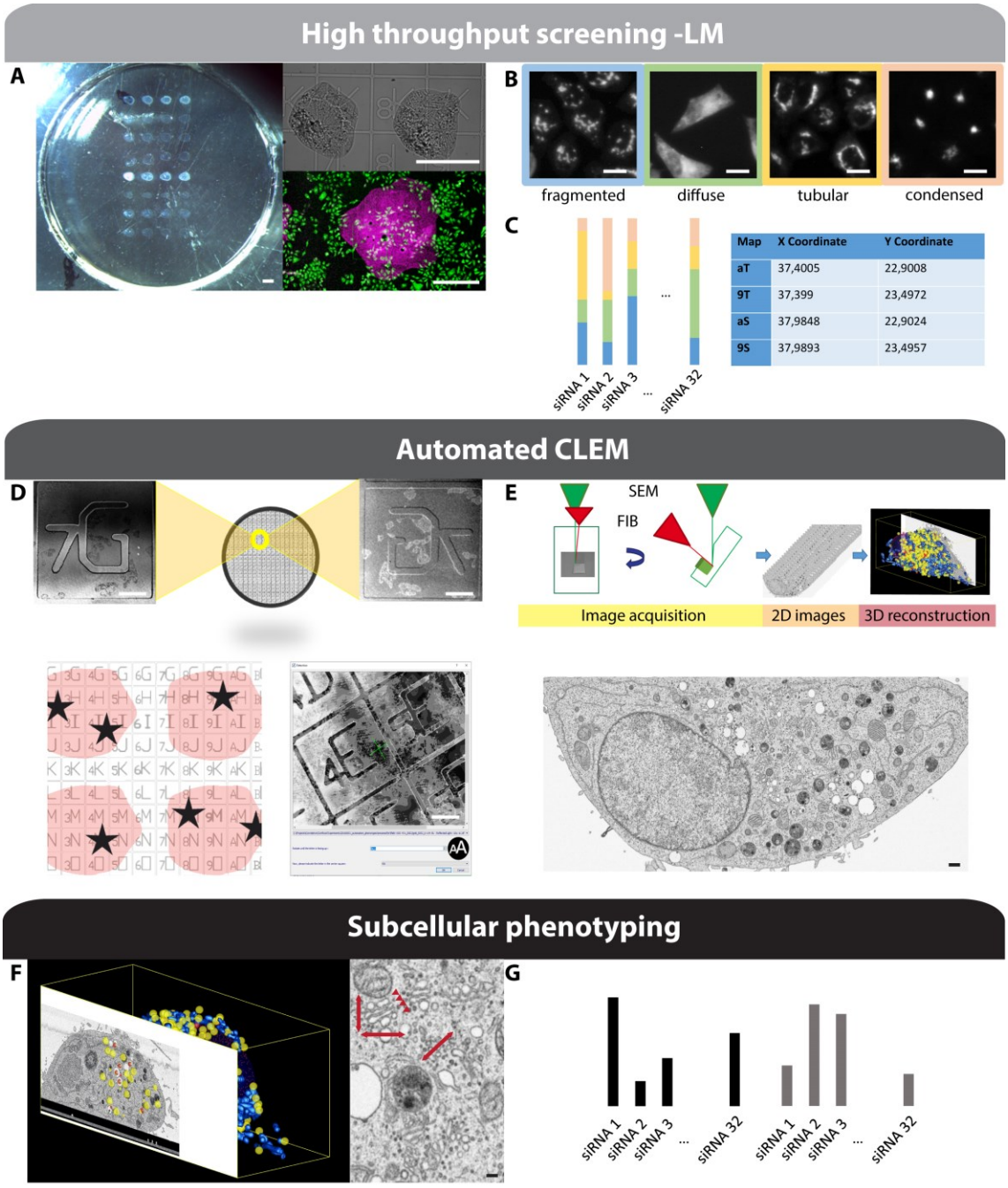

Figure 9: Automation strategy CLEM. Integration of multiple knockdowns. A) Spotted siRNA in the LM, transmitted (scale bar 600 µm) and fluorescent image (scale bar 300 µm). Automated image analysis, B) different Golgi phenotypes; scale bar 10 µm. C) Identification of phenotypic sub-populations. D) Automated navigation to phenotypic cells; scale bar 150 µm. E) Volume ultrastructure by automated serial imaging; scale bar 500 nm. F) Image analysis; scale bar 150 nm. G) Subcellular phenotyping.

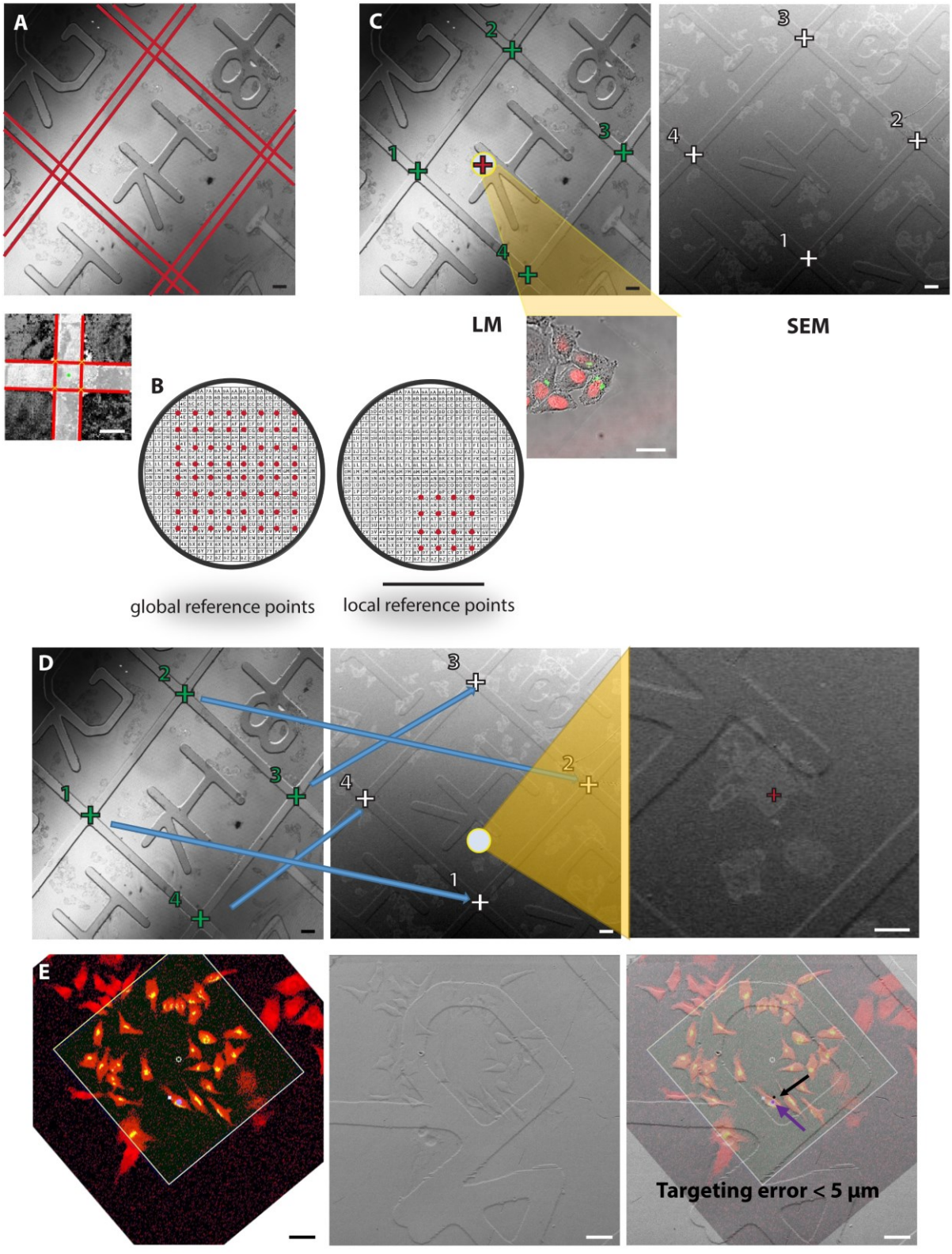

Figure 10: Coordinate transfer from LM to SEM. A) Line detection algorithm is run on the LM image, center of the intersections is used as a reference point. B) Global versus local distribution of reference points. C) Line detection and finding of reference points is done on LM and SEM images. D) A transformation matrix is used to predict where the cell coordinate from the LM is in the SEM. E) Overlay of LM and SEM image, predicted and real position of the ROI in the SEM; scale bar 20 µm.

2.2.5 Design of a stereological approach and image analysis

The major bottlenecks in FIB-SEM acquisition of isotropic datasets are the acquisition time and the amount of data generated. Imaging a full cell at a voxel size of about 10 nm x 10 nm x 10 nm takes 3 to 4 days, and generates 100 gigabytes of data. Our project aims to automatize the acquisition and measurement of hundreds of cells, however this is precluded by the current imaging conditions. Looking for an effective way to optimize the acquisition time, the volume of data and the analysis, we explored the potential of stereological tools compared to automated segmentation. We developed a semi-automated workflow for a high-pressure frozen HeLa cell, where all organelles were segmented (Tom Boissonnet, EMBL Monterotondo) using MIB (Microscopy Image browser), which is an "advanced image processing, segmentation and visualization software" (http://mib.helsinki.fi). It is used for cellular structure-function relationships of cells and cell organelles (Belevich, Joensuu *et al.*, 2016; Joensuu, Belevich *et al.*, 2014; Furuta, Yadav *et al.*, 2014; Majaneva, Remonen *et al.*, 2014). We also tried to apply this workflow to a cellbiological question, looking at the reformation of the nuclear envelope (NE) and the nuclear pore complex (NPCs) after mitosis (chapter 4). Although we were able to establish a semi-automated pipeline for some of the time points (Suruchi Sethi intern in the Schwab lab at that time, EMBL Heidelberg), we were not able to apply it for all and there was still quite a lot of manual supervision involved. Therefore we decided to use stereology to extract the morphology of organelles.

Stereology uses 2D information to estimate numbers, lengths, areas or volumes in the 3D space. In some instances, volumes and numbers are effeciently assessed by measuring from a relatively small set of serial sections through the same object. As the FIB-SEM offers the possibility to automate serial imaging, it has the potential to become a good sampling tool for stereology (Lucocq, Mayhew *et al.*, 2015; Ferguson, Steyer *et al.*, in preparation*)*. As a reference dataset, we decided to use an isotropic FIB-SEM volume, consisting of 1453 serial images from a high-pressure frozen cell. We then evaluated different stereological measures and compared different sampling schemes. This volume was manually segmented to get "ground-truth" measurements for different subcellular compartments (Figure 11).

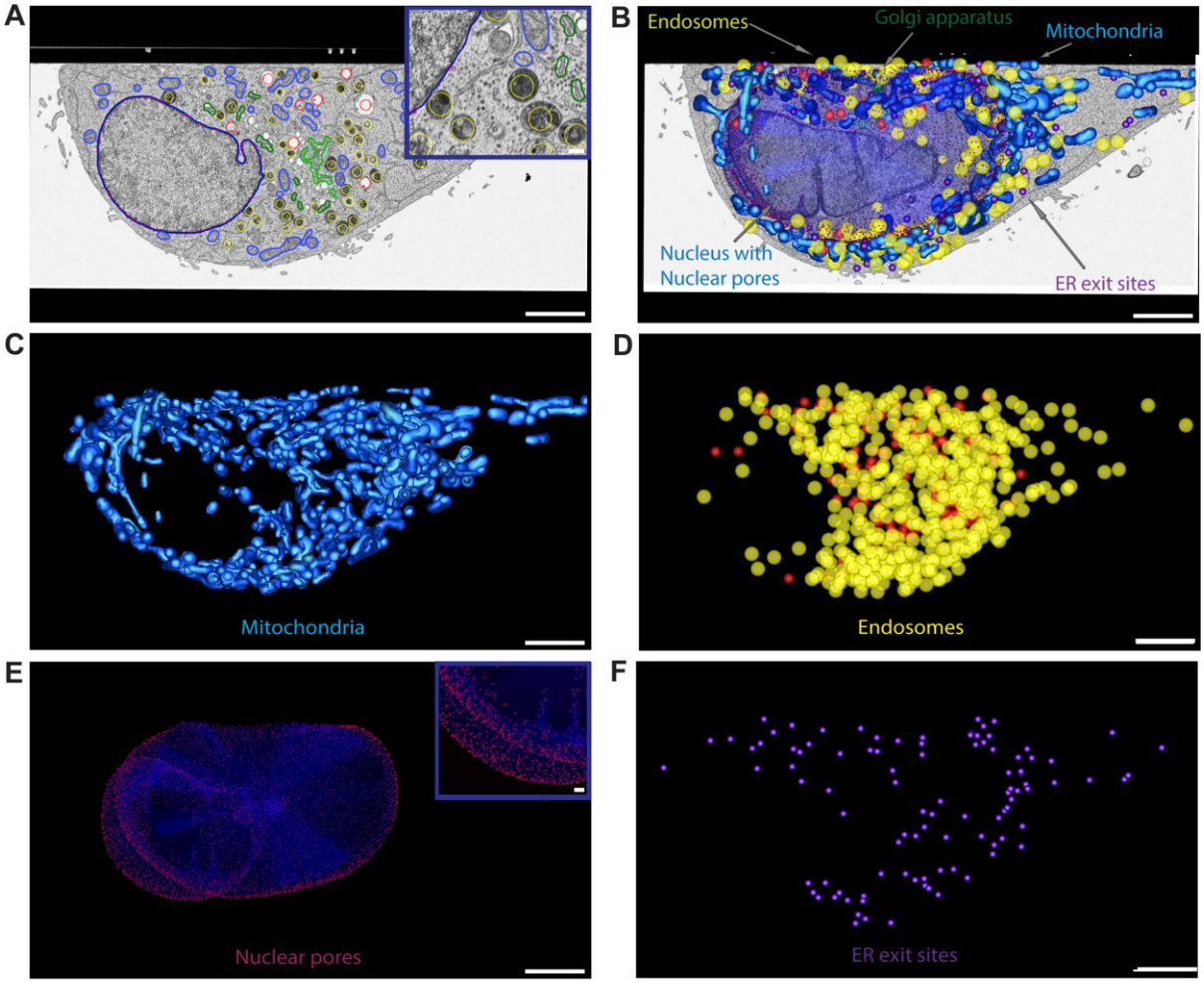

Figure 11: 3D-model of FIB-SEM dataset of high-pressure frozen GalNAc-T2-GFP cell. A) Representative image from the dataset of a GalNAc-T2-GFP stable cell, after high-pressure freezing and freeze substitution highlighting significant organelles: sorting endosomes = red, endosomes/lysosomes = yellow, Golgi apparatus = green, mitochondria = blue, nucleus = transparent blue, nuclear pores = pink, ER exit sites = purple; scale bar 5 µm (insert 500 nm). Reconstructed volume of 40 x 20 x 7 µm³ at 8 nm pixel size. B) 3D model of selected organelles. C) 3D modeling of the mitochondria. D) 3D representative of the endosomes/lysosomes (yellow), sorting endosomes (red). E) Representatives of the nuclear pores (insert scale bar 500 nm) and F) the ER exit sites; scale bar 5 µm.

We then used classical stereological probes on a fraction of evenly spaced sections taken from the isotropic dataset to measure the exact same features. We compared the results obtained for the mitochondria volume and for the endosomes/lysosomes number. For estimating the volume of the mitochondria we used the Cavalieri approach (Lucocq, 2008): A grid is placed on evenly spaced sections throughout the volume of interest (Figure 12 A). The total amount of points that fall onto the object (counts) is multiplied by the area associated with each point and by the distance between sections (Figure 12 A), which gives an estimate of the volume of the object of interest. We then evaluated the effect of the sampling frequency (*i.e.* the amount of serial

sections throughout the cell) on the volume estimate accuracy (Figure 12 B). We also tested if increasing the amount of counts per mitochondria (by keeping the grid spacing constant over increasing amounts of sections) would improve the measurement accuracy. In a first attempt, the grid spacing was kept constant (0.06 µm²) regardless of the number of sections. On average, each individual cross-section yielded 100 to 200 counts on mitochondria profiles. In order to approach an accurate estimate of the total volume, considering the heterogeneity of organelle distribution, at least 5-10 sections, meaning 1000 to 2000 counts were necessary. In a second attempt, the grid spacing was adapted to each set of serial section to be between 100-200 counts across the full set (Lucocq and Hacker, 2013). When five sections were selected, for example, a grid spacing of 0.2 µm² was used to reach 190 counts. Such a sampling strategy yielded an accuracy of 95 % when using 20 sections distributed across the volume of the mitochondria, for a total number of 100-200 counts and a grid spacing of 0.9 µm². Since different organelles have different sizes, the grid spacing has to be adapted to achieve 100 - 200 counts.

Counting objects requires a different set of stereological tools named disector (Gundersen, 1986). The disector consists of two parallel sections that are used to count particles (Figure 12 C). Only the particles appearing on one section (the reference plane), but not on the other (the look-up plane) are counted. Depending on the size of the particle/organelle the spacing of the disector has to be adapted to be closer than half the height of the smallest particle counted (Lucocq, 2008), regularly a spacing of ¼ - ⅓ of the smallest particle is used (Mayhew and Gundersen, 1996). To improve the counting efficiency the planes can be inverted (Figure 12 D) and the same counting scheme can be applied. Only particles that show up on the reference plane and disappear in the look-up plane are counted. To avoid overestimation the forbidden line rule is applied, where any particle touching the red line is not counted (Figure 12 E). With 10 sets of planes, we reached a counting accuracy of 95 % (SD = 1.58), when estimating the number of endosomes in this dataset. Taken together, these results prove that only a subset of serial sections is sufficient to reach measurement estimates with accuracy above 90 %.

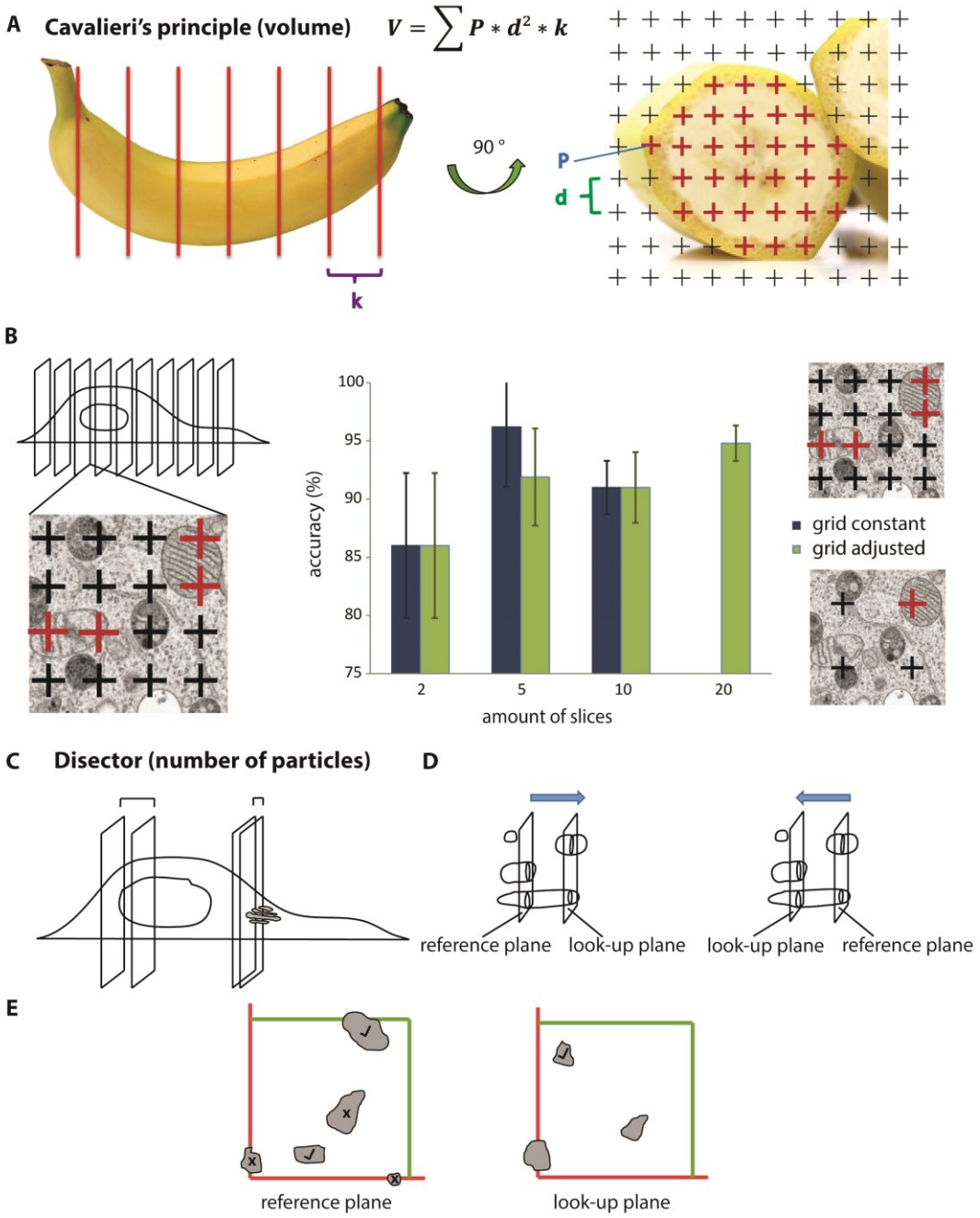

Figure 12: Stereological probe to estimate volume and number. A) Cavalieri principle to estimate volume. k = slice spacing, d = grid spacing, P = counts. B) The 3D modeled high-pressure frozen cell was used as the "ground-truth". To estimate the volume of the mitochondria 2, 5, 10 and 20 evenly spaced slices were used throughout the cell to count crosses lying on top of mitochondria. The total count multiplied by the area associated with every point and the z-spacing between slices was used to calculate the total volume. Keeping the grid spacing constant (increasing number of hits) was compared to adjusting the grid (keeping the counts between 100 and 200). With 20 slices and 200 counts a 95 % accuracy was reached. C) Estimating the number of particles uses the disector, two parallel sections that are situated closer than half the height of the smallest particle counted. D) One section (reference plane) is used to select particles and the other assesses which particles have disappeared (look-up plane), which are then counted. To improve the counting efficiency the planes can be inverted. E) Counted particles are marked with a check, discarded with a cross. To avoid overestimation the forbidden line rule is applied, where any particle touching the red line is not counted.

Thus, for such measures, isotropic datasets are not necessary, which represents a valuable advantage to dramatically reduce the acquisition time. Acquiring 20 serial sections, 1 µm apart, is performed in about 4 hours in the FIB-SEM, which includes exposing a cross-section of the cell (milling a trench and polishing the surface) and the acquisition of images throughout the region of interest. The same volume, acquired with isotropic voxels of 5 nm x 5 nm x 5 nm would require at least 2.5 days. We consider this as a key advantage when designing an approach where acquisition throughput is essential to achieve efficient screening. Moreover, we prove here that accurate estimates of volumes and number can be achieved by stereological tools and that they are much faster than the state of the art segmentation tools. Estimating the volume of the mitochondria in this dataset was performed in 0.5 hours with stereology; it took 16 hours to perform the segmentation of the isotropic dataset (manual segmentation using 3dmod). As a first case study we analyzed control Golgis and phenotypic Golgis (knockdown siRPGRIP1, chemically fixed) to assess the capabilities of traditional 3D modeling and quantification based on stereology. The fluorescence signal matches very well the 3D-model based on the EM data (Figure 13). Comparing the control with the phenotype, the composition of the Golgi did not change (Figure 13 E + J, Table 2), but instead of having individual substacks, the Golgi was stretching along the full length of the nucleus. The Cavalieri estimator was used to estimate the volume of the Golgi stack and compared to the numbers calculated based on the 3D-model (Table 14 G).

Table 2: Comparison of control and elongated Golgi

	Control Golgi	**Elongated Golgi**
Volume (µm³)	5.65	16.3
Amount of cisternae	2.45	2.34
Stack height (nm)	130.19	141.46

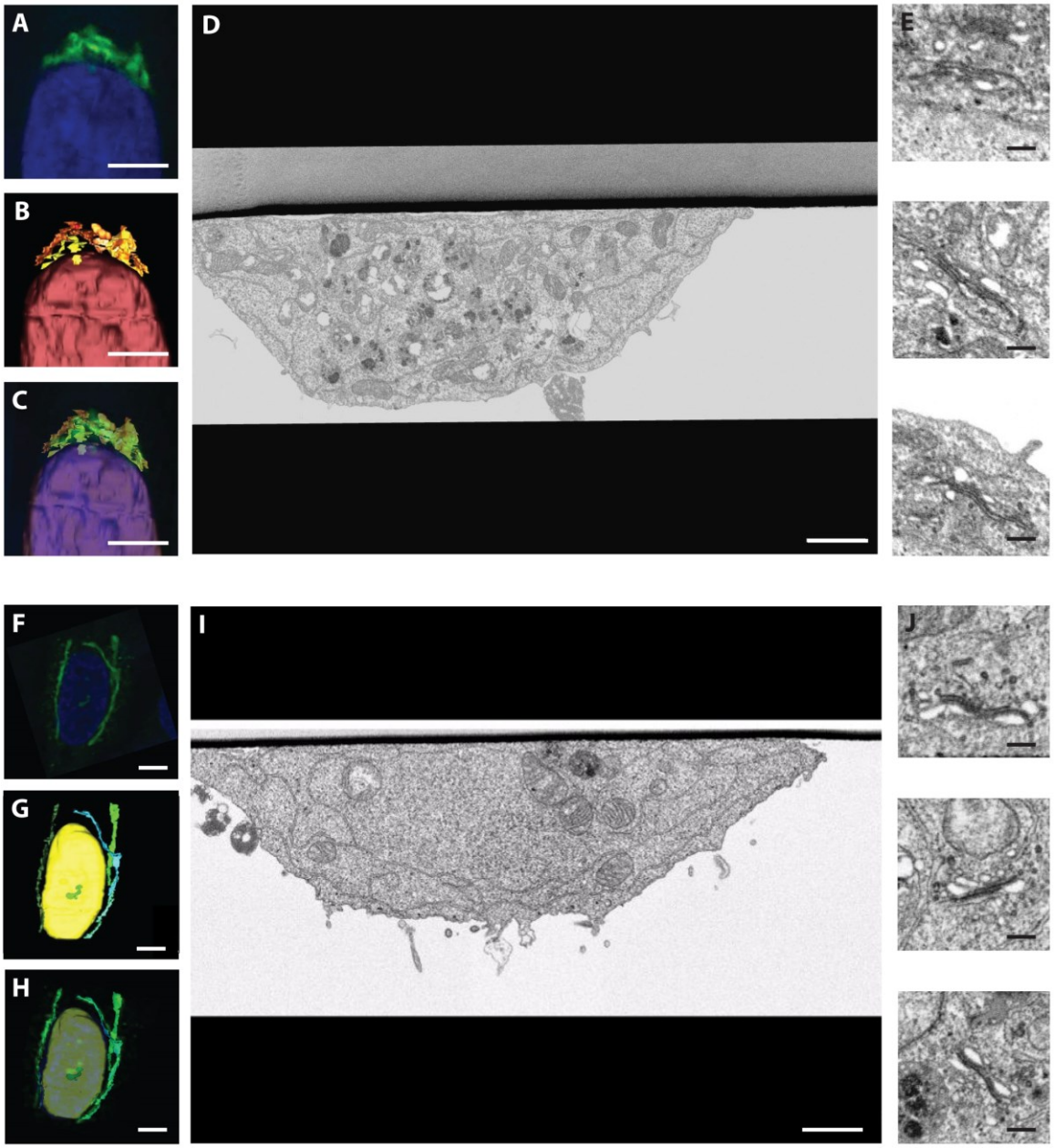

Figure 13: Comparison of control and phenotypic cell. Cells were chemically prefixed, imaged with confocal imaging and then further processed in a Ted Pella BIOWave Microwave. Datasets were acquired at isotropic 8 nm x 8 nm x 8 nm voxel size. Both datasets were aligned using Track-EM2. The 3D-modeling was done in IMOD (Boulder). A) - F) Neg9 siRNA was used as a negative control, to look at a control Golgi after 48 h knockdown. A) LM image. B) Model based on EM images. C) Overlay LM and model; scale bar 5 µm. D) EM image; scale bar 1 µm. E) EM images of the Golgi stack; scale bar 200 nm. F) - J) siRPGRIP1 was used as a phenotypic siRNA changing the morphology of the Golgi seen in the LM. F) LM image. G) Model based on EM images. H) Overlay LM and model; scale bar 5 µm. I) EM image; scale bar 1 µm. J) EM images of the Golgi stack; scale bar 200 nm.

The elongated Golgi had almost three fold larger volume (17.1 μm^3) than the control Golgi (5.89 μm^3), which was extracted from the 3D-model. In the segmentation, as well as the

stereological analysis, only cisternae were taken into consideration. A cisterna was defined as a membranous structure at least three times longer in one direction than the other. The volume based on the Cavalieri estimator showed only 4-5 % difference compared to the volume calculated from the 3D-model. The elongated Golgi had a calculated volume of 16.3 µm³, 4.2 % difference to segmented volume, and the control Golgi 5.65 µm³, 4.7 % difference to segmented volume, This illustrates that stereology can give very precise estimates even with only 20 sections and 200 counts. For different questions a total error of the stereological estimate of 5-10 % is sufficient enough to analyze data and to then compare differences between phenotypes or treatments (Yang, 2000; Gundersen, Jensen *et al.*, 1999; Lucocq, 2008).

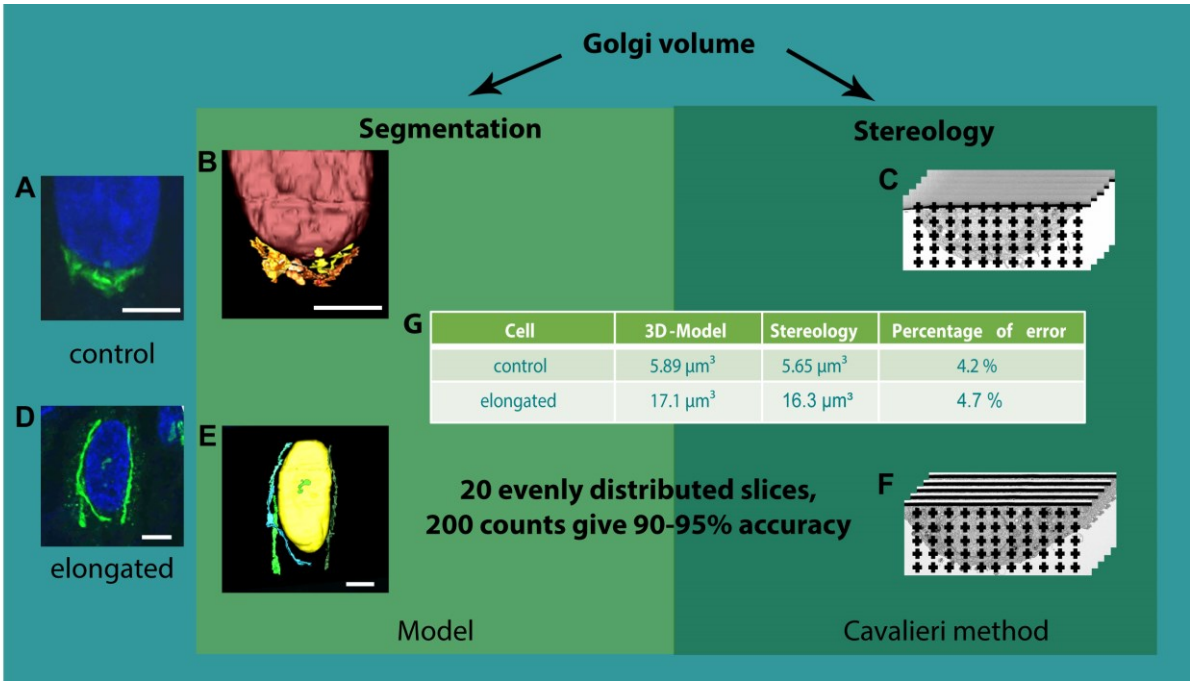

Figure 14: Comparison 3D-modeled data with stereology. The following criteria were used to identify the Golgi apparatus: enclosed membranous structure with multiple cisternae, where the longest axis is at least double the length of the other. The same individual did both types of analysis. GalNAc-T2-GFP cell treated with siNeg9: A) 63x FM image (GalNAc-T2-GFP to visualize the Golgi apparatus, DAPI to visualize the nucleus. B) Model of segmented EM images of negative control. C) Randomly placed systematic set of sections (EM images) through negative control. GalNAc-T2-GFP cell treated with siRPGRIP1: D) 63 x FM image. E) Model of segmented EM images of elongated phenotype. F) Randomly placed systematic set of sections (EM images) through elongated phenotype. G) For a control Golgi and a phenotypic Golgi the volume was compared using segmentation and stereology; scale bar 5 µm.

As a second stage we have started looking at 10 conditions (10 different siRNAs), a positive (COPB1) and a negative control (Neg9). The LM was done following the adaptive feedback microscopy pipeline described in 2.3.4**.** From the acquired cells, 2 were selected randomly, acquired in the FIB-SEM and analyzed with the stereological toolbox for the Golgi (Ferguson, Steyer *et al.*, in preparation). The following observations are preliminary and will be complemented in a near future, as soon as the development of the fully automated workflow is completed.

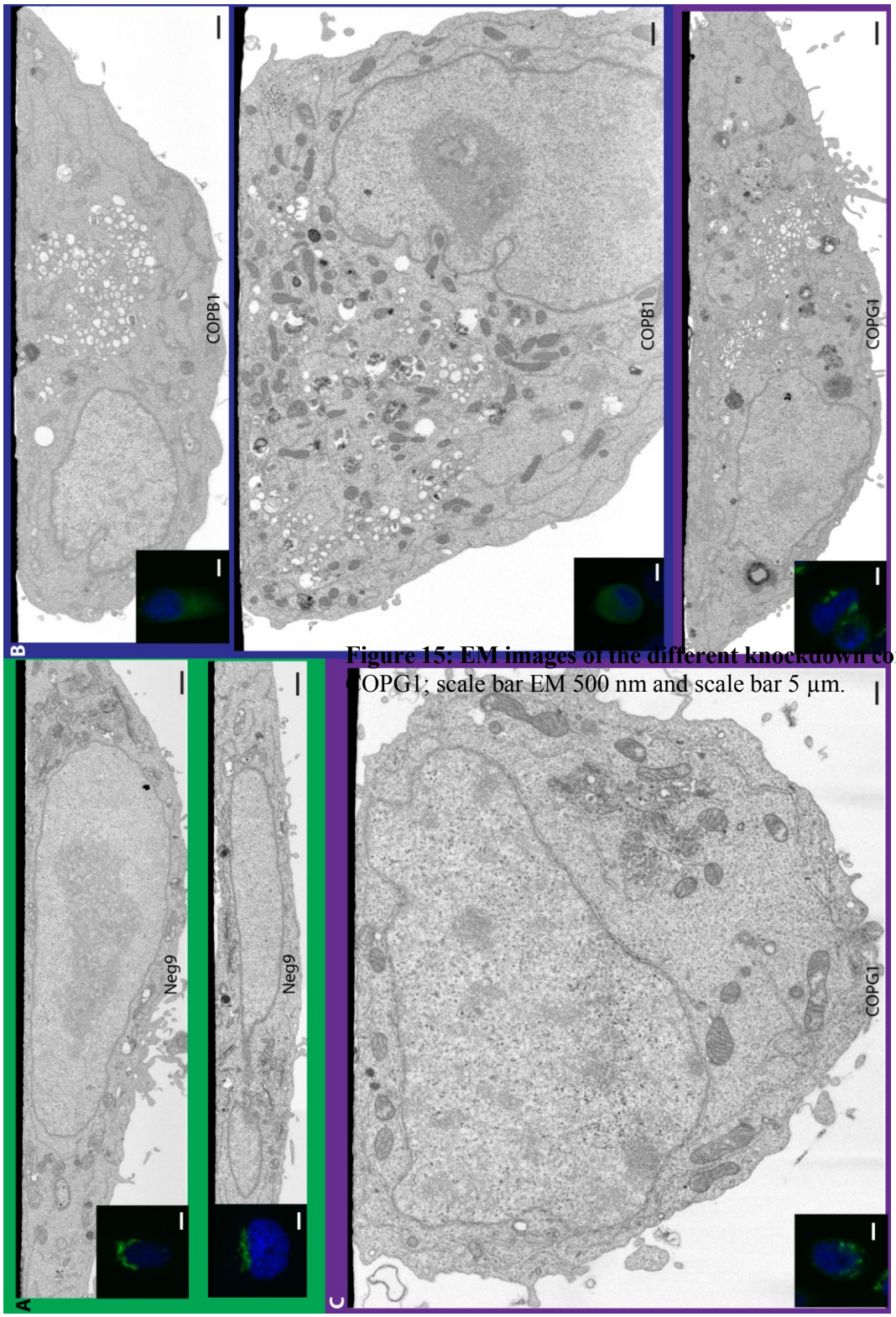

Figure 15: EM images of the different knockdown conditions and the correspon
COPG1; scale bar EM 500 nm and scale bar 5 µm.

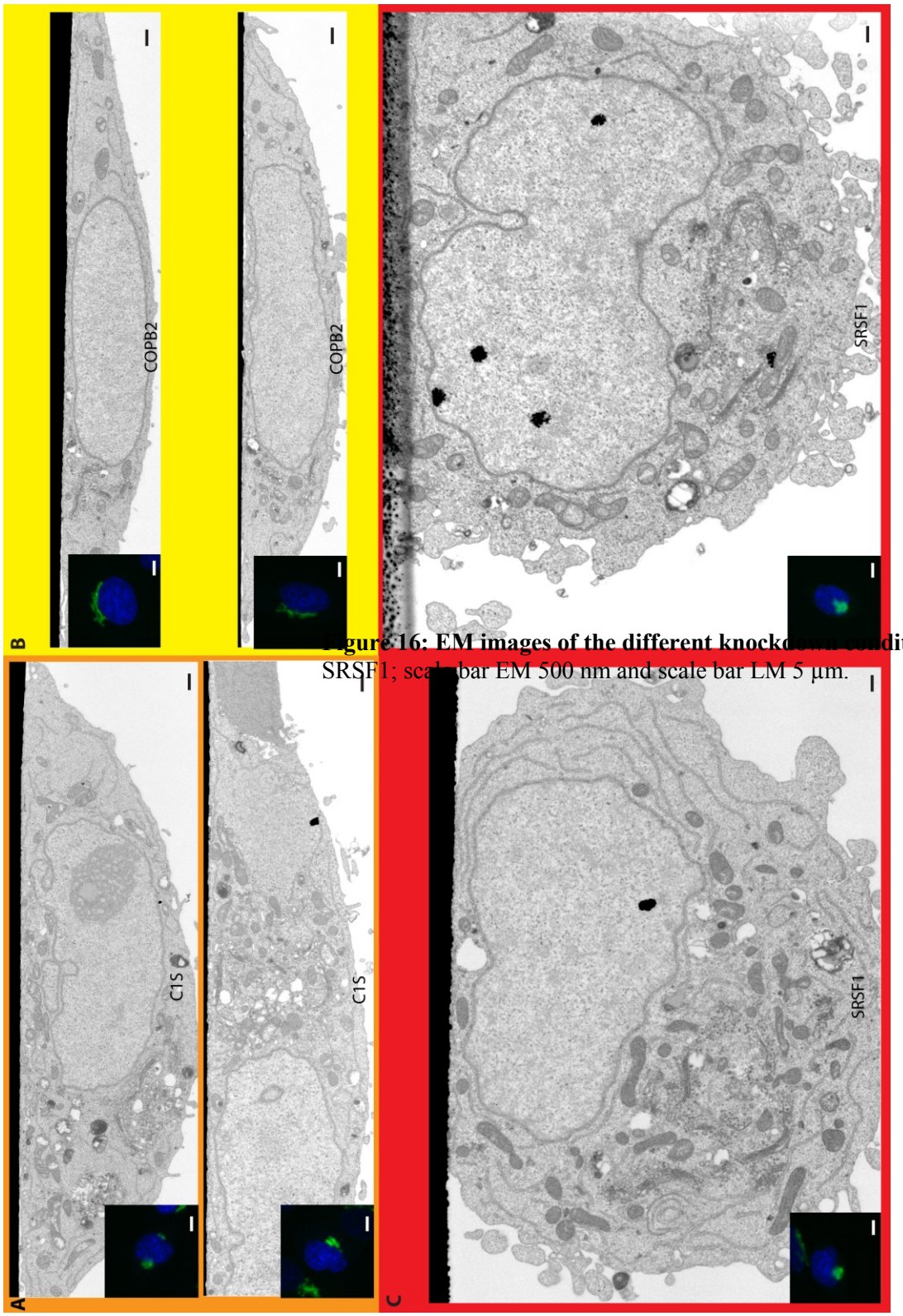

Figure 16: EM images of the different knockdown conditions and the correspond
SRSF1; scale bar EM 500 nm and scale bar LM 5 µm.

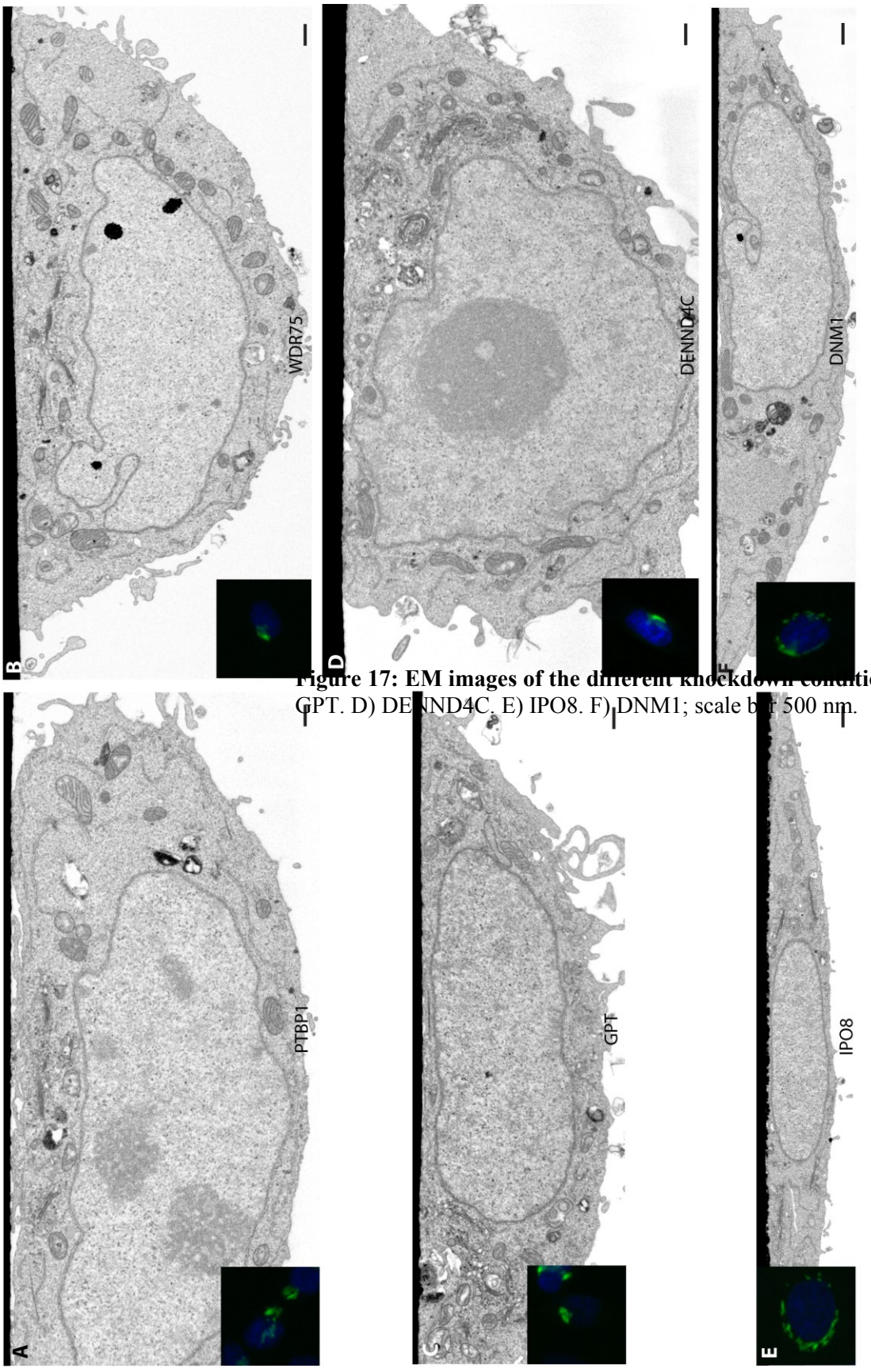

Figure 17: EM images of the different knockdown conditions and the correspond
GPT. D) DENND4C. E) IPO8. F) DNM1; scale bar 500 nm.

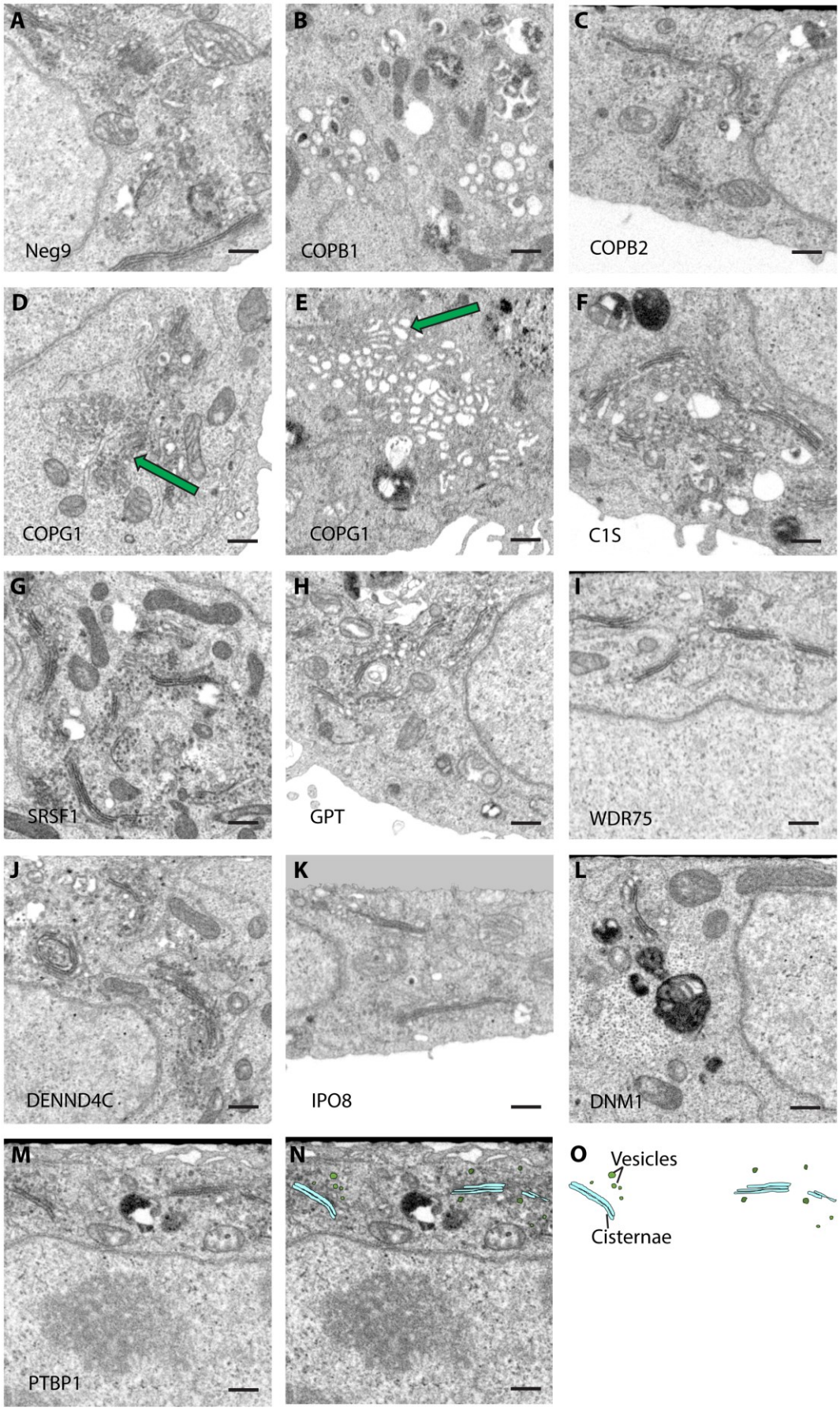

Figure 18: EM images of the Golgi stack in all treatments.

Figure 18 (previous page): A-M) EM images of the Golgi in different protein knockdown conditions. Green arrow pointing to small vesicles < 100 nm in D and > 100 nm vesicles in E. N) Overlay EM image and representation of cisternae (light blue, arrow) and vesicles (green, arrow head); scale bar 500 nm. O) Representation what was considered cisternae/vesicles.

A total of 6 different measurements were taken for all the treatments (Figure 19). Our positive control COPB1 did not show any cisternae, instead a lot of vesicles bigger than 100 nm. In one of the cells from the COPG1 knockdown, another protein from the COP family, similar large vesicles (> 100 nm) were visible (Figure 18 E), while in the second one a few individual cisternae were left, surrounded by many small vesicles (< 100 nm; Figure 18 D). While the phenotypic analysis in the LM classified these two cells in the same category (Figure 15), the variability seen for the ultrastructure of the Golgi would require further analysis on more cells (Figure 16, Figure 17). Although the knockdown was classified as diffuse, there were still some defined structures visible in the LM, which seemed to correspond to the different vesicle agglomerations seen in the EM. Although COPB2 showed a reduction of cisternal volume, amount of cisternae and stack height (Table 3), it did not look similar to COPB1/G1 in the LM. Parallel observations made at the LM revealed that the COPB2 phenotype could take up to three days to appear. Further assays would therefore be necessary to complete the ultrastructural analysis of this specific knockdown. Compared to the negative control, SRSF1 knockdown induced an increased volume of the cisternae (about 23 %), which was explained by an increased average amount of cisternae, also corresponding to an increased stack height. Cells treated with the C1S or the PTBP1 siRNA on the other hand presented a decreased total cisternae volume despite a slightly higher number of cisternae. PTBP1 cells showed a decreased stack height, closer packing of the cisternae, which would explain the change of volume. COPB2, SRSF1, C1S as well as WDR75 cells had a higher surface density of cisternal membranes compared to the negative control. In the case of SRSF1 and C1S this seems to be done through increased numbers of cisternae. WDR75 on the other hand had a decreased volume with the same amount of cisternae, which also would indicate closer stacking of the cisternae. Another possibility would be larger cisternae (larger width), which was not measured this time, but could be investigated in the future.

Table 3: Comparison of the treatments to the negative control. Blue = decrease, yellow = increase, white = no difference, pink = not existing in that sample, also indicated by arrows.

Volume cisternae	Volume vesicles Ø < 100 nm	Volume vesicles Ø 100 – 350 nm	Amount cisternae	Stack height	Surface density cisternae
COPB1 ↓	COPB1 ↑	COPB1 ↑	COPB1 ↓	COPB1 ↓	COPB1 ↓
COPB2 ↓	COPB2 →	COPB2 x	COPB2 ↓	COPB2 ↓	COPB2 ↑
COPG1 ↓	COPG1 ↑	COPG1 ↑	COPG1 ↓	COPG1 ↓	COPG1 ↓
C1S ↓	C1S ↓	C1S x	C1S ↑	C1S →	C1S ↑
SRSF1 ↑	SRSF1 ↑	SRSF1 x	SRSF1 ↑	SRSF1 ↑	SRSF1 ↑
GPT ↓	GPT ↓	GPT x	GPT ↑	GPT →	GPT ↑
WDR75 ↓	WDR75 ↓	WDR75 x	WDR75 →	WDR75 →	WDR75 ↑
DENND4C →	DENND4C ↓	DENND4C x	DENND4C ↑	DENND4C →	DENND4C →
IPO8 →	IPO8 ↓	IPO8 x	IPO8 →	IPO8 ↓	IPO8 →
DNM1 ↓	DNM1 ↓	DNM1 x	DNM1 ↑	DNM1 ↓	DNM1 →
PTBP1 ↓	PTBP1 ↓	PTBP1 x	PTBP1 ↓	PTBP1 ↓	PTBP1 →

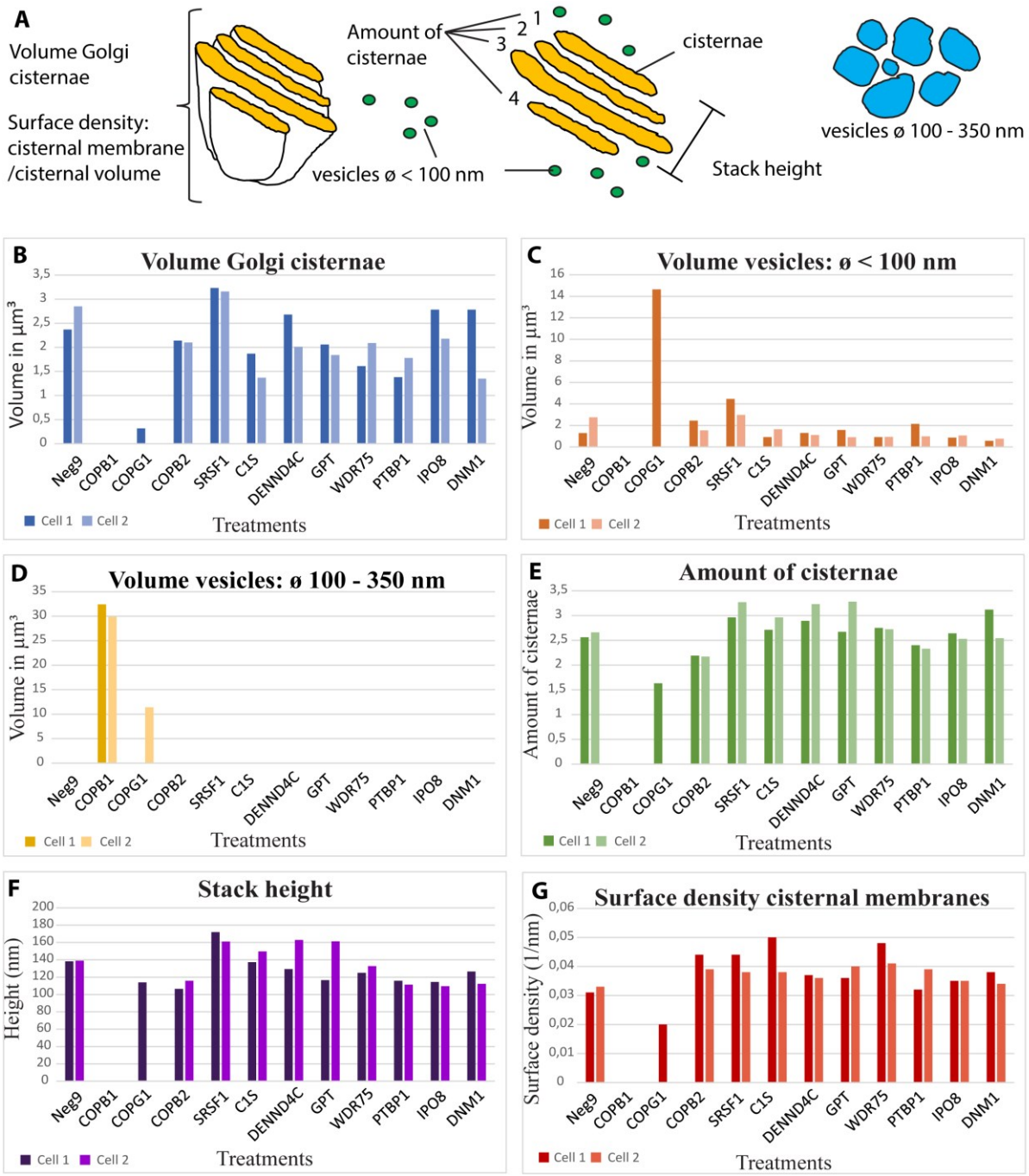

Figure 19: Quantification of Golgi phenotypes using stereology. Two cells for every treatment, plus negative (Neg9) and positive control (COPB1) were selected by the LM-pipeline and acquired in the FIB-SEM. Different values were quantified using different stereological tools (Figure 21). A) Illustration of the different measures taken. B) Volume of the cisternae. C) Volume of vesicles < 100 nm in diameter D) Volume of vesicles 100–350 nm in diameter. E) Average amount of cisternae. F) Average stack height. G) Average surface density of cisternal membranes.

As a summary, we have developed an automatic CLEM workflow on heterogeneous samples, combining multiple treatments in one dish, feedback microscopy and screening for a specific phenotype on the LM level. So far, this has been followed by targeting the cells manually and acquiring them manually as well. As a next step, we will use the MSite program to automatically target the same cell that has been selected by LM, after processing in the EM, acquiring the 3D-EM data automatically and analyzing the data with stereological probes (Figure 21). The spotting of up to 32 different siRNA in one MatTek dish was the first step to allow higher throughput. After 48 h of knockdown, the cells were lightly fixed and imaged in the confocal microscope. With an image analysis pipeline, the pre-scan images were analyzed and cells that were untypical compared to the negative control, but typical for their treatment were selected. From this pool, 3 to 5 cells were randomly chosen for EM analysis. This ensured a selection as objective as possible. Heavy fixation, dehydration and embedding in resin was then carried out in a microwave to speed up the sample processing time (from a couple of days to 1.5 h). Importantly, cells from all 32 different siRNA treatments were processed together, which makes the sample preparation more comparable. The sample was introduced into the FIB-SEM and the program developed by José Miguel Serra Lleti acquired overview images to match with the images from the LM and predict where the regions of interest are inside the EM.

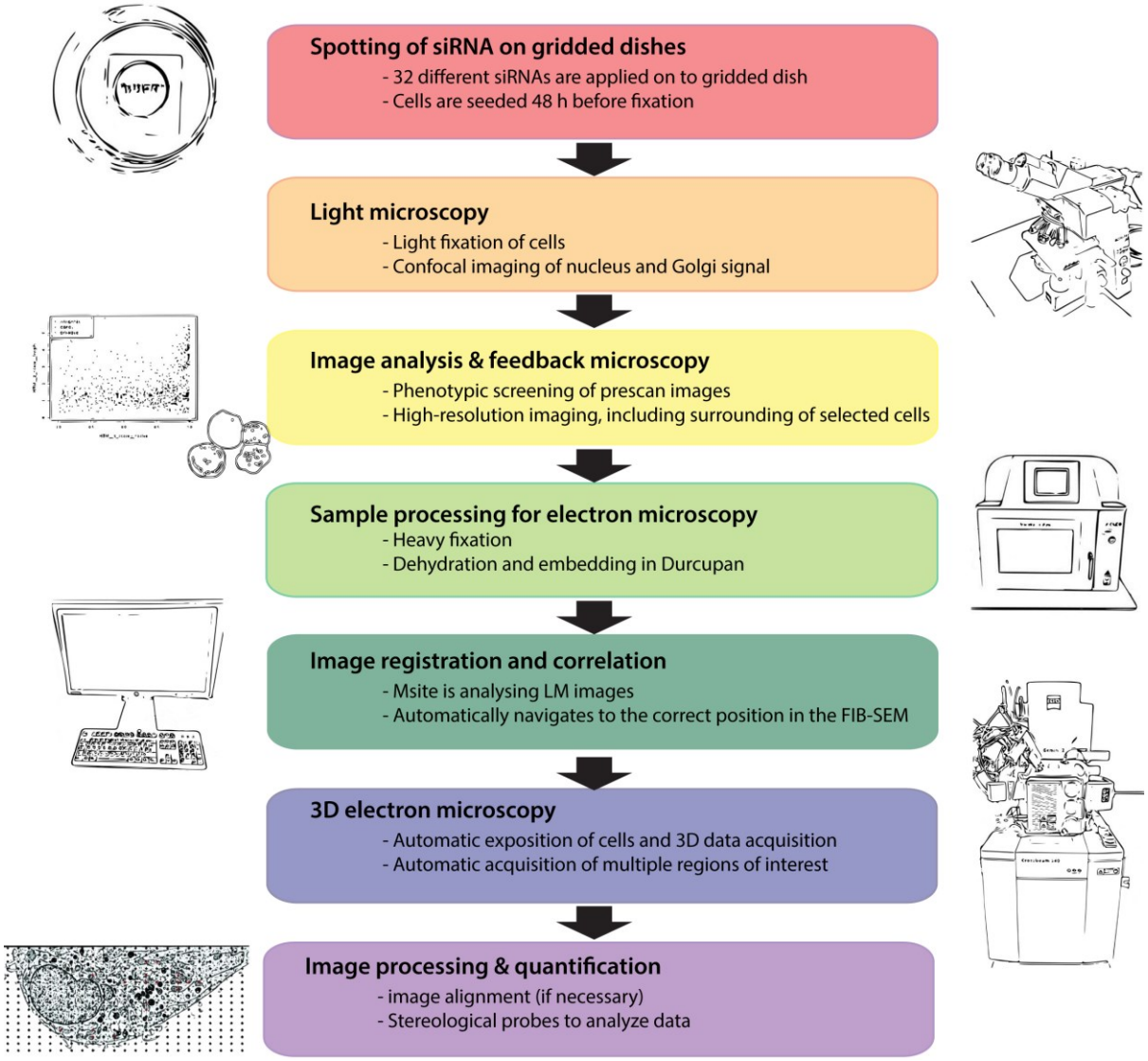

Figure 20: Workflow automatic CLEM. Real images of the different steps of the workflow were acquired and turned into cartoons using cartoonize.net.

MSite will iteratively drive the FIB-SEM stage to the different positions, expose a cross-section, and acquire the region of interest (ROI) by first milling and then imaging. Upon completion of the first ROI, MSite will drive to the next position and trigger a new acquisition. At this stage the region of interest could be acquired isotropically, which would slow down the acquisition speed. However, since we have evaluated that for our purposes 20 sections are enough to get quantitative and precise measures, we will only acquire 20-40 sections throughout our region of interest. From those 20 sections we will calculate the cisternal volume, the volume of vesicles, the stack composition, the stack thickness and the surface density of cisternae (Ferguson, Steyer *et al.*, in preparation), as was done for the manually acquired cells above. After implementing the last things missing in out automatic pipeline, we

will continue acquiring more datasets. Instead of spending days to weeks with modeling one dataset, we can achieve the analysis with the stereological tools within one hour. With the acquisition of 24 cells from 12 different treatments we could confirm that our sampling scheme seems to be good to extract numbers. It took 12 days for the acquisition and 4 days for the analysis. Still, we need to acquire more cells from different samples to make the measurements robust, to also be able to do statistics. Therefore, the use of stereology speeds up our full workflow in two areas, the acquisition and the analysis. We have estimated that with this workflow we could acquire and analyze 100 cells in less than 3 months instead of 3 years if CLEM was done manually on full resolution volumes.

2.3 Methods

2.3.1 Sample preparation for Correlative Light and Electron Microscopy (CLEM)

Since light and electron microscopy require different sample preparation techniques, multiple fixation protocols were tested to find the best conditions for both imaging modalities. The best results were achieved with the following protocol: Cells grown in a MatTek dish (gridded-bottom dish, P35G-2-14-C-GRID) were lightly fixed with a mixture of 0.5 % glutaraldehyde, 4 % formaldehyde and 0.05 % malachite green in 0.1 M PHEM buffer for 14 min at 250 W in a TedPella microwave. After pre-fixation the cells were treated with 150 mM glycine in PHEM buffer (240 mM PIPES, 100 mM HEPES, 8 mM $MgCl_2$, 40 mM EGTA in H_2O, pH 6.9) to quench the glutaraldehyde induced auto-fluorescence and afterwards stained with DAPI (1 µg/ml) for 5 min.

2.3.2 Cell culture and transfections

HeLa Kyoto cells stably expressing GalNAc-T2-GFP (Storrie, White *et al.*, 1998) were maintained in Dulbecco's Modified Eagle's Medium (DMEM, Sigma Aldrich, St. Louis, USA) culture medium containing 10 % fetal calf serum, 100 U/ml penicillin and 100 µg/ml streptomycin and 2 mM L-Glutamine, incubated at 37 °C and 5 % CO_2. Cell selection was applied using 500 µg/ml Geneticin (G-418 sulfate, Gibco Life Technologies) for every passage of the cells. Cells were incubated on siRNA spotted gridded MatTek dishes (MatTek cooperation) and incubated for 48 h in DMEM medium without phenol red. The cells were kept in 0.1 M PHEM buffer during imaging until they were heavily fixed.

2.3.3 Spotting of siRNAs

siRNAs changing the morphology of the Golgi apparatus (Simpson, Joggerst *et al.*, 2012) used in this study were obtained from Ambion/ThermoFisher as Silencer Select reagents, please see Supplemental data (Table 7), for siRNA IDs and sequences.) They were used in a pre-screen in order to find the most promising candidates for further CLEM experiments. 96-well plates (glass-bottom) were coated with siRNA transfection mixes (Erfle, Neumann *et al.*, 2007). Afterwards, HeLa Kyoto cells stably expressing GalNAc-T2-GFP (3400 cells /well) were seeded using an automated cell seeding device (Multidrop / ThermoFisher). Cells were imaged on a ScanR microscope (Olympus, UPlanSApo 20x 0.7 Ph2, DAPI, GFP and transmitted light). The plates contained two control siRNAs targeting COPB1 a subunit of the vesicular coat protein complex COPI. In addition to non-silencing negative control siRNA (XWNEG9) and

COPB1 as a positive control, the 14 siRNAs (Table 8) showing the most prominent phenotypes were chosen for further CLEM experiments. These siRNAs were spotted onto a gridded MatTek dish (P35G-2-14-C-GRID) using a contact spotter (ChipWriter Pro- Bio-Rad Laboratories) resulting in a layout of 4 x 8 spots (Erfle, Neumann *et al.*, 2007). The array contained a total of 6 controls, as follows: 3 spots of negative control siRNA (XWNEG9), 2 spots of siRNA against ECT2 (transfection control) and 1 spot of siRNA against COPB1. The other spots contained siRNA that target genes showing a Golgi phenotype after RNAi knockdown. 175000 cells were seeded onto the spotted MatTek dishes and fixed with a light fixation (0.5 % glutaraldehyde, 4 % formaldehyde in 0.1 M PHEM) after 48 h.

2.3.4 Light Microscopy hardware and software

After the MatTek dish was mounted on the LM stage we interactively located the four siRNA corner spots based on their green/red fluorescence using a 10x lens. At each corner, we used a home-made GUI-based software tool to request the stage position from the microscope. This software tool then generated a list of stage positions (2x2 sub-positions within each siRNA spot) that were passed to the Leica Matrix Screener software. 10x objective, 680x680 pixels, zoom 6, FOV 258 µm x 258 µm, 4x averaging, sequential scan for excitations 405 nm (DAPI-labeled nuclei), 488 nm (GalNAc-T2-GFP), 594 nm (A594-labeled gelatin). Prior to each acquisition a software autofocus on the DAPI signal was performed. The image analysis pipeline (http://cellprofiler.org/releases/) was configured to segment nuclei based on the DAPI signal and then create cell ROIs by radial dilation of each nuclear ROI. Within each cell ROI the GalNAc-T2-GFP signal was used to compute four intensity-independent features characterizing different typical alterations of Golgi morphology: “diffuse”, “fragmented”, “tubular” or “condensed” (Figure 5). Diffuse was designed to characterize the fraction of seemingly unbound GalNAc-T2-GFP. The diffusiveness of a cell was computed as the integrated GalNAc-T2-GFP signal after a morphological gray-scale opening divided by the integrated GalNAc-T2-GFP signal. Tubularity was designed to detect cells with elongated Golgi structures. To compute tubularity, morphological gray-scale openings of the GalNAc-T2-GFP signal were computed at different orientations using linear structural elements. The tubular signal in each pixel was computed as the difference between the orientations that yielded the maximum and the minimum response of this filter. The tubularity of a cell was computed as the integrated tubular signal divided by the integrated GalNAc-T2-GFP signal in this cell. Fragmentation was designed to characterize the number of seemingly unconnected (diffuse) Golgi structures. To this end, locally bright signals were enhanced by a top-hat filter

and then binarized by an automated thresholding method. In each cell, Golgi fragmentation was measured as the number of connected components in the binary image. The condensation of the Golgi was measured via the form factor, which is 1 for a perfectly circular object. First, cells expressing too little GalNAc-T2-GFP were rejected based on the integrated GalNAc-T2-GFP signal. Next, mitotic cells were rejected based on the coefficient of variation (CoV) of the DAPI signal, using the observation that, due to chromosome condensation, mitotic cells have a higher DAPI CoV than interphase cells.

For each of the cells selected by image analysis the following automated scan job pattern is triggered: (a) cell coordinates are passed to the microscope and the stage is positioned such that the selected cell is centered on the optical axis, (b) software autofocus on DAPI signal of the target cell using 40x objective, (c) high-resolution Z-stack acquisition (9 slices, 10.1 µm range) with 40x objective, 512x512 pixels, zoom 5, FOV 77.5 µm x 77.5 µm, channels 405 nm/488 nm, (d) imaging of the spatial context of the cell including the etched coordinate grid with the 10x objective, 1024x1024 pixel, zoom 1.2, FOV 1.29 mm x 1.29 mm, channels 405 nm/488 nm/594 nm fluorescence, transmitted/reflected light. Communication with the microscope software is implemented in python using a library of functions that communicate with the Leica Matrix Screener software (Tischer, Hilsenstein *et al.*, 2014).

2.3.5 Automation/Targeting Software MSite

The MSite program is first used to rename the images and run a line detection and letter recognition algorithm on the reflected light images. In the FIB-SEM an image of the coordinate system is taken using the SESI (Secondary Electron Secondary Ions) detector and the orientation and the letter of this position are indicated in the software. From an internal grid map, which corresponds to the coordinate system layout, the MSite program moves the stage to the approximate position of the center of the first square, in which our cell of interest is located. An image is acquired and the line detection algorithm acquires the reference points, which are the intersection of the coordinate system. After doing this for every region of interest (ROI), the most local reference points for every cell are taken to predict the correct position of the cell using a transformation matrix. To align the electron-beam and the ion-beam, a square is burned on the surface of the sample. The geometrical relation between the two beams is used to move the stage to the coincidence point, where both beams are hitting the same point on the sample surface. A cross-section through the ROI is exposed and the alternating run of milling and image acquisition is started automatically. After the acquisition of one position is

accomplished, the MSite program moves the stage of the FIB-SEM to the next ROI, where a new acquisition is started.

2.3.6 Electron microscopy processing

The entire EM processing was done using a Ted Pella BIOWave microwave (Table 4). We prefixed the cells according to (2.3.1).

Table 4: Microwave malachite Green Protocol for fixation of monolayer cells. Green = fixation (aldehydes), orange = post-fixation (osmium tetroxide), blue = post-staining (tannic acid), yellow = post-staining (uranyl acetate), red = dehydration with graded EtOH series

Step#	Description	User Prompt (on/off)	Time (Hr:min:sec)	Power (Watts)	Temp (°C)	Load Cooler (off/auto/on)	Vacuum/ Bubbler Pump	SteadyTemp pump (on/off)	SteadyTemp (°C)
Protocol #8 Malachite Green Fixation									
1	MalGreen GA fix	Off	0: 2: 0	100	50	Off	vacuum on	On	23
2	MalGreen GA fix	Off	0: 2: 0	0	50	Off	vacuum on	On	23
3	MalGreen GA fix	Off	0: 2: 0	100	50	Off	vacuum on	On	23
4	MalGreen GA fix	Off	0: 2: 0	0	50	Off	vacuum on	On	23
5	MalGreen GA fix	Off	0: 2: 0	100	50	Off	vacuum on	On	23
6	MalGreen GA fix	Off	0: 2: 0	0	50	Off	vacuum on	On	23
7	MalGreen GA fix	Off	0: 2: 0	100	50	Off	vacuum cycle	On	23
	2 bench washes								
8	PHEM Buffer	On	0: 0: 40	250	50	Off	Off	On	23
9	PHEM Buffer	On	0: 0: 40	250	50	Off	Off	On	23
10	Osmium	On	0: 2: 0	100	50	Off	vacuum cycle	On	23
11	Osmium	Off	0: 2: 0	0	50	Off	vacuum on	On	23
12	Osmium	Off	0: 2: 0	100	50	Off	vacuum on	On	23
13	Osmium	Off	0: 2: 0	0	50	Off	vacuum on	On	23
14	Osmium	Off	0: 2: 0	100	50	Off	vacuum on	On	23
15	Osmium	Off	0: 2: 0	0	50	Off	vacuum on	On	23
16	Osmium	Off	0: 2: 0	100	50	Off	vacuum cycle	On	23
	2 bench washes								
17	PHEM Buffer	On	0: 0: 40	250	50	Off	Off	On	23
18	PHEM Buffer	On	0: 0: 40	250	50	Off	Off	On	23
19	Tannic Acid	On	0: 1: 0	150	50	Off	vacuum cycle	On	23
20	Tannic Acid	Off	0: 1: 0	0	50	Off	vacuum on	On	23
21	Tannic Acid	Off	0: 1: 0	150	50	Off	vacuum on	On	23
22	Tannic Acid	Off	0: 1: 0	0	50	Off	vacuum on	On	23
23	Tannic Acid	Off	0: 1: 0	150	50	Off	vacuum on	On	23
24	Tannic Acid	Off	0: 1: 0	0	50	Off	vacuum on	On	23
25	Tannic Acid	Off	0: 1: 0	150	50	Off	vacuum cycle	On	23
	2 bench washes								
26	PHEM Buffer	On	0: 0: 40	250	50	Off	Off	On	23
27	Water	On	0: 0: 40	250	50	Off	Off	On	23
28	Water	On	0: 0: 40	250	50	Off	Off	On	23
	2 bench washes								
29	UA	On	0: 1: 0	150	50	Off	vacuum cycle	On	23
30	UA	Off	0: 1: 0	0	50	Off	vacuum on	On	23
31	UA	On	0: 1: 0	150	50	Off	vacuum on	On	23
32	UA	Off	0: 1: 0	0	50	Off	vacuum on	On	23
33	UA	Off	0: 1: 0	150	50	Off	vacuum on	On	23
34	UA	Off	0: 1: 0	0	50	Off	vacuum on	On	23
35	UA	Off	0: 1: 0	150	50	Off	vacuum cycle	On	23
36	Water	On	0: 0: 40	250	50	Off	Off	On	23
37	Water	On	0: 0: 40	250	50	Off	Off	On	23
38	25% ETOH	On	0: 0: 40	250	50	Off	Off	On	23
39	50% ETOH	On	0: 0: 40	250	50	Off	Off	On	23
40	70% ETOH	On	0: 0: 40	250	50	Off	Off	On	23
41	90% ETOH	On	0: 0: 40	250	50	Off	Off	On	23
42	100% ETOH	On	0: 0: 40	250	50	Off	Off	On	23
43	100% ETOH	On	0: 0: 40	250	50	Off	Off	On	23
44	100% ETOH	On	0: 0: 40	250	50	Off	Off	On	23
Protocol #11 - Resin infiltration									
1	Resin 1:4	On	0: 3: 0	250	50	Off	vacuum cycle	On	23
2	Resin 1:2	On	0: 3: 0	250	50	Off	vacuum cycle	On	23
3	Resin 100	On	0: 3: 0	250	50	Off	vacuum cycle	On	23
4	Resin 100	On	0: 3: 0	250	50	Off	vacuum cycle	On	23

After confocal imaging, we strongly fixed this time with 2.5 % glutaraldehyde, 4 % formaldehyde, 0.05 % malachite green in 0.1 M PHEM buffer, and postfixed with 0.8 % $K_3Fe(CN)_6$, 1 % OsO_4 in 0.1 M PHEM. The sample was then stained successively with 1 % tannic acid and 1 % uranyl acetate (both aqueous) to enhance contrast. Samples were dehydrated in a graded series of ethanol (50 %, 70 %, 90 %, 95 %, 2x 100 %) and embedded

in Durcupan (Sigma-Aldrich, USA). To compare fixation methods, cells were also grown on etched sapphire disks, then high-pressure frozen and freeze-substituted in 1 % OsO_4, 0.1 % uranyl acetate and 5 % H_2O (Walther and Ziegler, 2002) in acetone. Samples were dehydrated in ethanol and embedded in Durcupan and polymerized in the oven for 96 h at 60 °C. The etched patterns from the MatTek dish (Hanson, Reilly *et al.*, 2010) or the sapphires were later used to target the cell of interest in the EM (Walther and Ziegler, 2002; Spiegelhalter, Tosch *et al.*, 2010). To be able to select hundreds of cells from one large sample from different treatments we decided to do chemical fixation in a petridish, where the final sample diameter is 1.2 cm, compared to 3 mm diameter of samples frozen in the high-pressure freezer.

2.3.7 Sample preparation High-Pressure Freezing

Sapphire disks were carbon coated with a finder grid and baked in the oven overnight at 100 °C. Before seeding the cells on sapphire disks, they were exposed to UV-light for 20 min. The samples were processed in a high-pressure freezer (HPM 010; ABRA Fluid AG, Widnau, Switzerland). The cells were immersed in 1-hexadecene as a cryo-protectant right before freezing. The samples were freeze substituted using an automatic freeze substitution unit (Leica EM AFS). They were incubated with 1 % OsO_4, 0.1 % uranyl acetate and 5 % H_2O in 100 % acetone at -90 °C for 24 h (Villinger, Gregorius *et al.*, 2012). The temperature was raised from -90 °C to -30 °C (5 °C/h), kept at -30 °C for 3 h and raised to 0 °C (5 °C/h). The samples were washed with 100 % acetone, infiltrated with increasing concentrations of Durcupan in acetone (25 %, 50 % and 75 %, in the microwave 3 min each at 250 W) and finally embedded in 100 % Durcupan. The polymerization was carried out at 60 °C for 4 days.

2.3.8 FIB-SEM on cell monolayer

The central disk of the MatTek dish was broken out using heat shock. The resin disk, containing the samples, with the imprint of the coordinate system on the surface was mounted on conductive carbon sticker (12 mm, Plano GmbH, Germany) that were placed on SEM stubs (6 mm length, Agar Scientific). To reduce the amount of charging, the samples were surrounded by silver paint and gold coated for 180 sec at 30 mA in a sputter coater (Quorum, Q150RS). The samples were introduced into the Auriga 60/Crossbeam 540 (Zeiss, Germany) and positioned so that the sample was facing the SEM at an angle of 36° and the FIB at an angle of 54°. The program MSite is interfacing with ATLAS 3D being part of Atlas5 software from Fibics (Ottawa, Canada), to navigate to the correct positions and to prepare the ROI for imaging. The FIB is used at two current intensities for creating a cross-section: 15 nA to reach

a depth of 20 µm from the block surface, and 3 nA for polishing the cross-section before imaging. For imaging, the FIB milling was operated with 1.5 nA, the SEM imaging and the FIB milling was operating simultaneously (Narayan, Danielson *et al.*, 2014). The SEM images were acquired at 1.5 kV with the Energy selective Backscattered (EsB) detector with a grid voltage of 1100 V, analytical mode at a 700 pA current, setting the dwell time and line average to add up to 1.5 min per image.

2.3.9 Stereology

From every siRNA treatment, three cells were randomly selected by the image analysis program (HTM explorer, R). They were chosen because they were typical for every individual treatment and very different to the negative control. For all estimations 20 evenly spaced sections throughout the datasets were used. Inside the FIB-SEM, images were acquired evenly throughout our volume of interest with a spacing of 50 to 100 nm. The grid spacing was chosen to achieve a total of 100 to 200 points on top of our structure of interest. Since the cells are always acquired in a distinct orientation, 90° to the attachment plane, cycloids instead horizontal/vertical crosses were used to ensure unbiased estimations (Lucocq, 1993). The Golgi tool box (Ferguson, Steyer *et al.*, in preparation) is used to characterize the Golgi phenotypes by looking at volume of cisternae, volume of vesicles, stack composition, stack thickness an the surface density of cisternae (Figure 21). Cisternae were defined as membranous structures devoid of ribosomes and one axis being at least three fold bigger than the other axis.

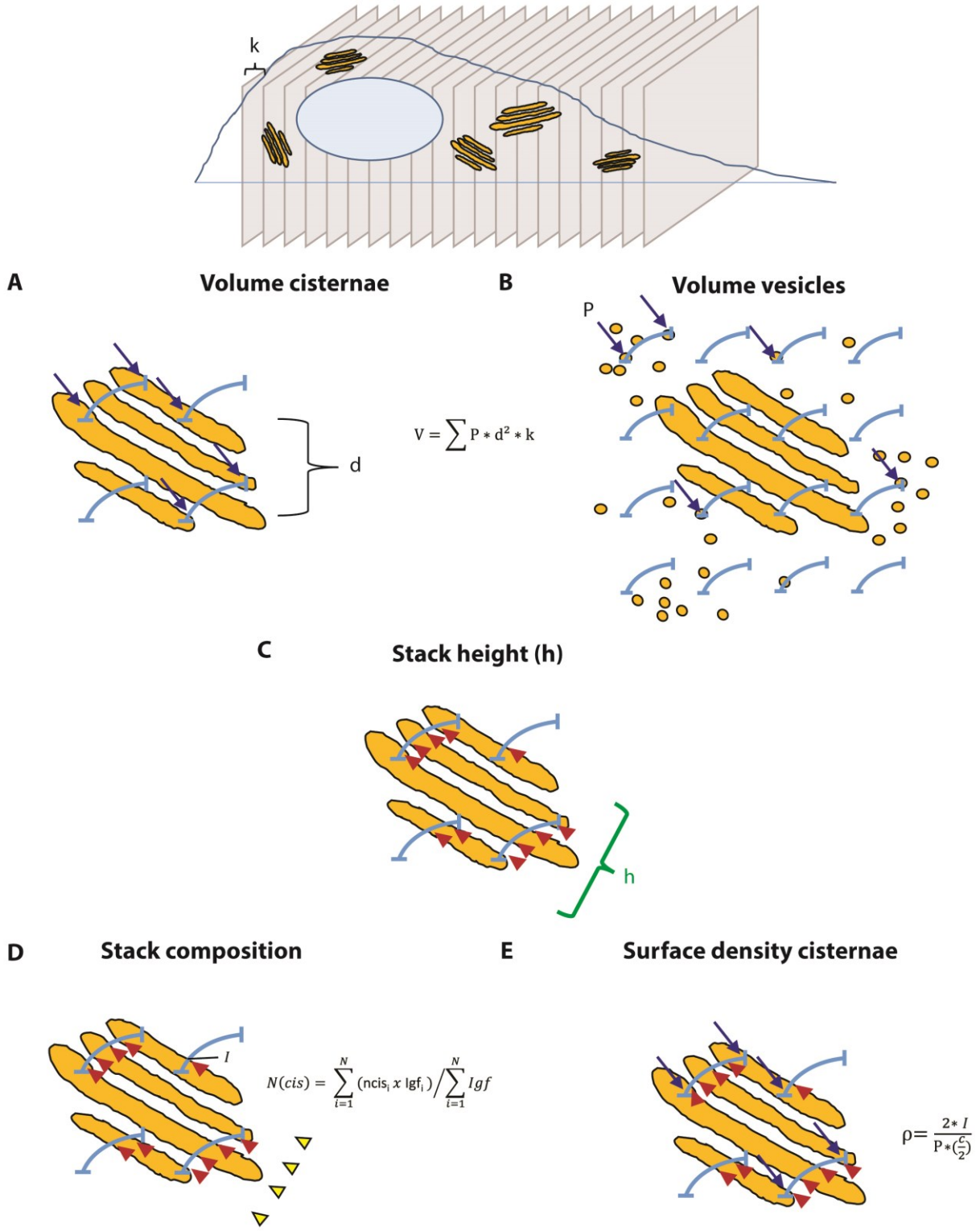

Figure 21: Stereology toolbox. Different stereological tools were used specifically to quantify effects of different treatments for the Golgi apparatus. A) Volume of cisternae. B) Volume of vesicles. C) Stack height. D) Stack composition (amount of cisternae). E) Surface density of vesicles. Cycloids (light blue) were used for unbiased estimation. Arrows (dark blue) indicate point counts, which were used for volume/surface density estimations. Arrow heads (red) highlight line intersections, which were used to select a measurement position (stack height and stack composition) and to estimate the surface density (adapted from Ferguson, Steyer et al., in preparation).

We used different stereological tools to quantify various parameters of the Golgi apparatus in our selected phenotypes (Figure 21). Some of the tools being very general, like the volume estimation by Cavalieri, but also some very specific ones for the Golgi apparatus, like the stack composition, which are described in a toolbox for the Golgi (Ferguson, Steyer *et al.*, in preparation). As mentioned above we used cycloids to ensure unbiasedness in our estimations. The volume of the cisternae as well as the volume of the vesicles was estimated as described above, multiplying the total amount of points that fall onto the object (blue arrows) by the area associated with each point and by the distance between sections (Figure 12 A, Figure 21 A/B). Besides changes in the volume, we also looked at changes within the Golgi stack concerning the stacking. The stack height and the amount of cisternae could vary, therefore we looked at the height of the Golgi stack (Figure 21 C) and evaluated the stack composition (Figure 21 D). Wherever the cycloid hit a Golgi stack (red arrow head), the height of the Golgi stack was measured orthogonal to the longest axis. From all measurements an average was calculated. The same unbiased counting tool of cycloid crossing cisternae was used to count the amount of cisternae counted orthogonal to the longest axis of the cisternae (yellow arrow heads, Figure 21 D). The amount of cisternae (1, 2, 3, 4…) was totaled individually, products were summed and divided by the total number of cisternae, giving the average number of cisternae (Lucocq, Berger *et al.*, 1995). While focusing on the Golgi stack itself, we also looked at the amount of membranes within over the cisternal surface. Therefore, we looked at the surface density of the cisternae. For calculating surface densities two measures were combined. The total amount of intersections of the cycloid with cisternae was counted to estimate the length of membranes. To estimate the surface area the total amount of points falling on cisternae were counted. Combining both values we calculated the surface density for cisternae.

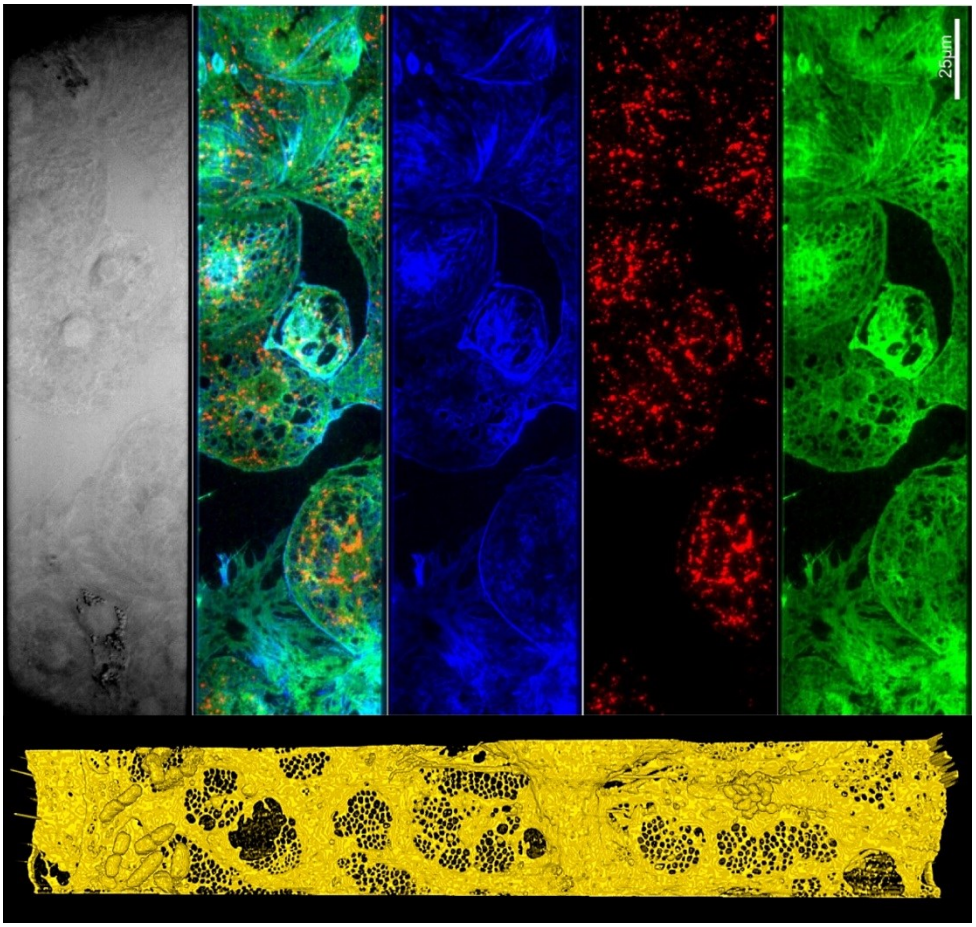

Chapter 3: CLEM on photonics chips

Cover image: Liver sinusoidal endothelial cells being imaged on a waveguide with different wavelengths (top) and the 3D modeling of the FIB-SEM data.

3.1 Introduction

In the previous chapter, we have seen how a coordinate system, when embedded in the culture dish (gridded MatTek), could serve as a seed to automate the correlation between fluorescence imaging and FIB-SEM. We have successfully used it with widefield and with confocal imaging. Interestingly, we are collaborating with a Norwegian group (Lab of Balpreet Singh Ahluwalia, Department of Physics and Technology, University of Tromsø) that is developing new super-resolution modalities, relying on an engineered culture substrate that integrates part of the light microscopy device. Our idea was to further customize this chip in making it compatible with CLEM, with the long-term goal to fully automate super-resolution FIB-SEM imaging in a high-throughput fashion.

So far, super-resolution systems are expensive and take up quite a lot of space and can normally not easily be moved to another location. Present optical nanoscopy (Hell and Wichmann, 1994; Betzig, 1995; Moerner and Kador, 1989), super-resolution microscopy, uses a complex microscope setup to illuminate the sample and a simple glass slide to hold the sample. The lab of Balpreet Singh Ahluwalia is striving to reverse this situation. They have started to develop a complex photonic integrated circuit (PIC) which generates a paradigm shift in the field of super-resolution microscopy; making it accessible to any lab, anywhere. The PIC both holds and illuminates the sample so that it can acquire super-resolved images (30-50 nm resolution in x/y), even if used with a simple standard microscope. The light from an external laser is coupled into the waveguide via an objective lens. The light then travels through the waveguide (SiO_2) by internal reflection, similar to total internal reflection microscopy (TIRF). The emitted signal from fluorochromes is collected by a standard upright microscope. The possibility to acquire super-resolved images on-chip was shown in 2015 (Helle, 2015) using STORM as a proof-of-principle. The waveguides on the photonics chip generate an evanescent field which illuminates the sample (cells or tissue sections) along the waveguide strip with only minimal loss of excitation light (Shen, Huang *et al.*, 2014). The evanescent field shows a high signal-to-noise ratio and low photo-toxicity, which facilitates imaging of living cells (Agnarsson, Jonsdottir *et al.*, 2011). However, the optical properties of the evanescent field limit the field of view to 100 -150 nm above the waveguide.

Ahluwalia's group long-term vision is to enable the widespread of affordable multi-modality optical nanoscopes (dSTORM, STED, LSM and EM) by retrofitting any standard fluorescence microscope with this new PIC technology. This will empower a large community of researchers, physicians, and industrial end-users to use chip-based optical nanoscopes to generate new technological and scientific breakthroughs. Together with our colleagues, we set out to develop a workflow for CLEM on-chip, and we aimed to optimize the chip itself, as well as the sample preparation for this purpose. In this collaboration, Ahluwalia's Lab was designing the photonics chips/LM imaging. The biological model, the liver sinusoidal endothelial cells (LSECs) was delivered by Peter McCourt (Vascular Biology Research Group, Department of Medical Biology, University of Tromsø). The EM facility (Randi Olsen, Advanced Microscopy Core Facility, Institute of Medical Biology, Faculty of Health Sciences, University of Tromsø) helped with developing a workflow and sample preparation to do CLEM on-chip.

Table 5: Pro and contra of waveguide imaging

Waveguide imaging	Pro	Contra
	Only thin section (z) illuminated	Only 150-200 nm in z illuminated
	High signal-to- noise ratio	
	Low photo-toxicity	
	Light can be guided in pattern	Light cannot reach everywhere
	Large field of view	

LSECs are the building blocks of the sinusoidal wall in the liver. They can be considered as selective sieves for substances passing from the blood to fat-storing and parenchymal cells and the other way around. As a second function the LSECs are considered to be scavenger cells, since they clear the blood from different macromolecules (Smedsrod, De Bleser *et al.*, 1994; De Leeuw, Brouwer *et al.*, 1990). Therefore, they show high endocytic capacities. As a morphological feature that has been reported to act as a filter, the cells are highly fenestrated (Wisse, De Zanger *et al.*, 1985). To be able to better understand the structure-function relationship of the LSECs, also in the context of bacteria/virus in the bloodstream, it is very interesting to look at the cells at the highest resolution possible both at the LM and at the EM level.

3.2 Results and Discussion

Since the cellular structures and the morphology of the LSECs were of interest, full isotropic correlative light and electron microscopy data were acquired as a first proof-of-principle and, in a later step, assessing the possibilities for automation in acquiring multiple regions of interest on one chip automatically (similar automation used in chapter 2). For both parts of the project, it was required to keep track of the imaged cells when moving from FM to EM. To facilitate this, it became necessary to add landmarks to the surface of the photonics chip in order to retrieve the same cell in both imaging modalities.

The photonics chip consists of different inorganic layers of material (Figure 22). Si_3N_4 is used as the supporting material on which the strip of "waveguide" (height 150 nm, width 100 µm), also consisting of Si_3N_4, is placed. To avoid any interference between two neighboring waveguides they are separated laterally by 20 µm layer of p-Si. To enable the correlation, we have designed a specific chip that would present landmarks for CLEM. SiO_2 was used to form 1.5 µm tall alphanumerical landmarks, where the pixel size of the design of the landmarks is 1 µm (Figure 22).

Importantly the landmarks should be visible in both imaging modalities. We have seen in chapter 2 that removing a gridded coverslip from the block after resin embedding was leaving correlative landmarks at the surface that were used to relocate the cells of interest. Whilst this is an easy task when dealing with petri-dishes or coverslips, it was cumbersome with the PICs. Approaching the cells from the top (Figure 24) after flat embedding and laser branding, as described in the chapter 4, was not an option either, because the photonics chip was opaque and did not allow imaging in a standard LM to first locate the landmarks. Finding an alternative was thus necessary. Elaborating on a solution presented by others (Kizilyaprak, Bittermann *et al.*, 2014), we explored the possibility to reduce the amount of resin covering the cells. The goal of this is two-fold: on one hand, the covering layer of resin should leave the landmarks exposed for direct visualization by LM and SEM, and on the other hand, the physical properties of the resin should be compatible with stable imaging inside the resin. For these reasons the main properties were the fluidity of the liquid mixture of resin (the more fluid the better), and the hardness of the polymerized block (the harder the better) (Figure 25 and Figure 26).

A

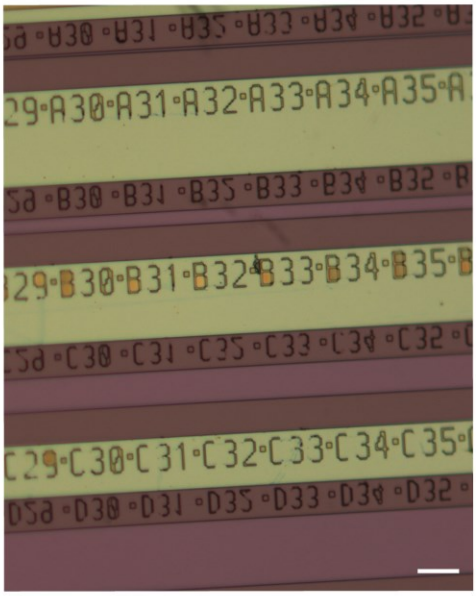

B

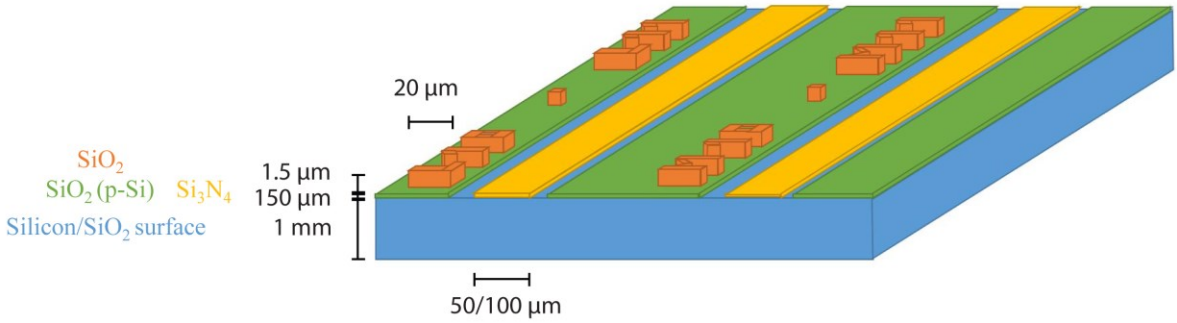

Figure 22: Layout of a landmarked photonics chip. A) Stereoscopic view on the landmarked chip prototype; scale bar 20 µm. B) Scheme of the landmarked chip: blue = SiO_2 substrate, green = SiO_2 (p-Si) absorbing layer, orange = SiO_2 landmarks, yellow = Si_3N_4 waveguide.

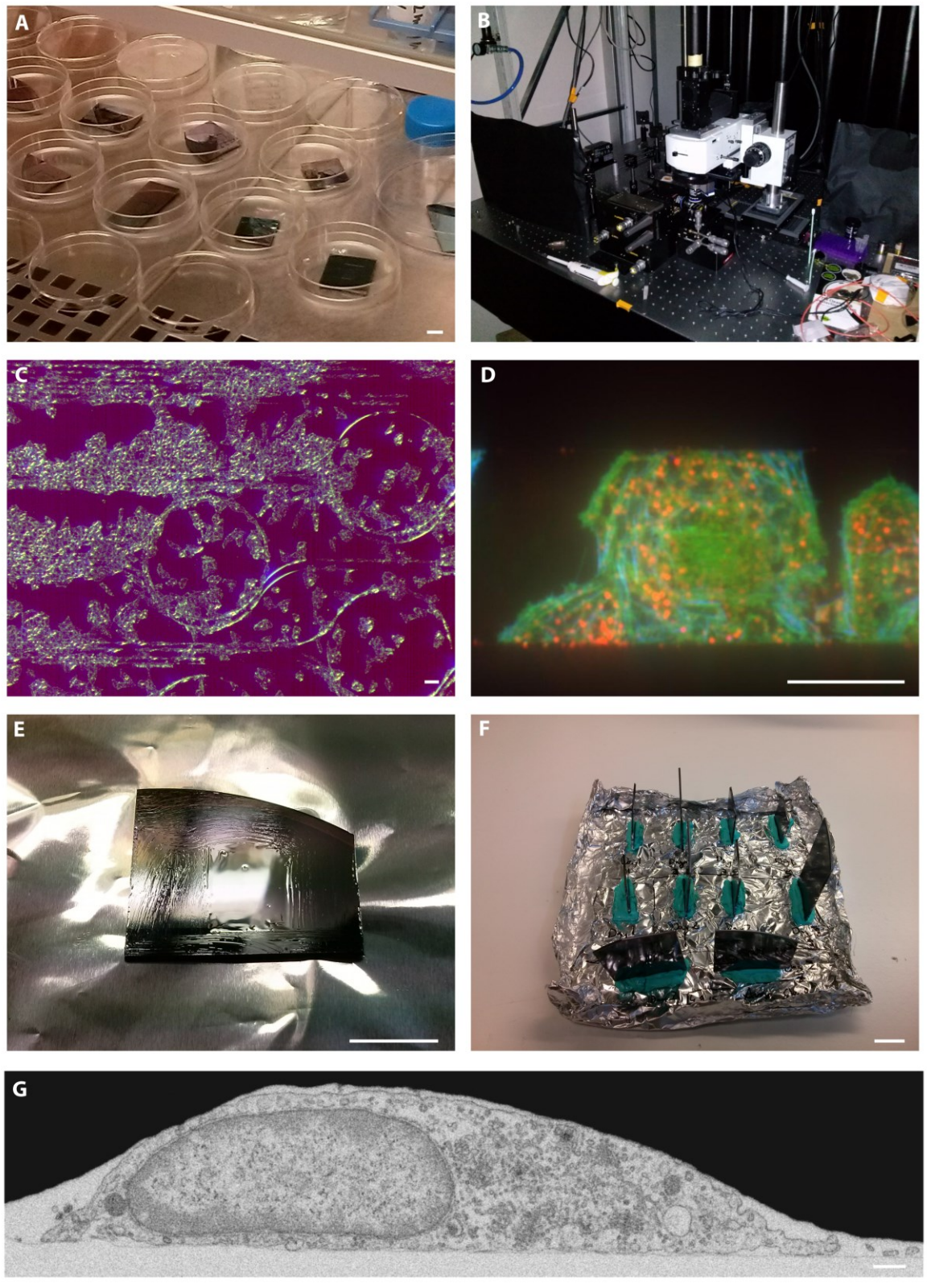

Figure 23: Improving the fixation for cells processed on chip. A) Cells being seeded on photonics chips; scale bar 1 cm. B) Waveguide imaging microscope build by Øystein Helle Ivar in the lab of Balpreet Singh Ahluwalia. C) Cells on top of waveguide structures; scale bar 40 µm. D) Composite image of LSEC on waveguide (red = lysosomes, green = cell membranes, blue = actin skeleton); scale bar 25 µm. E) Photonics chip with LSECs during EM processing (after resin infiltration); scale bar 1 cm. F) Set-up for resin polymerization of photonics chips; scale bar 1 cm. G) Cross-section through LSEC, EsB detector, 5 nm pixel size; scale bar 500 nm.

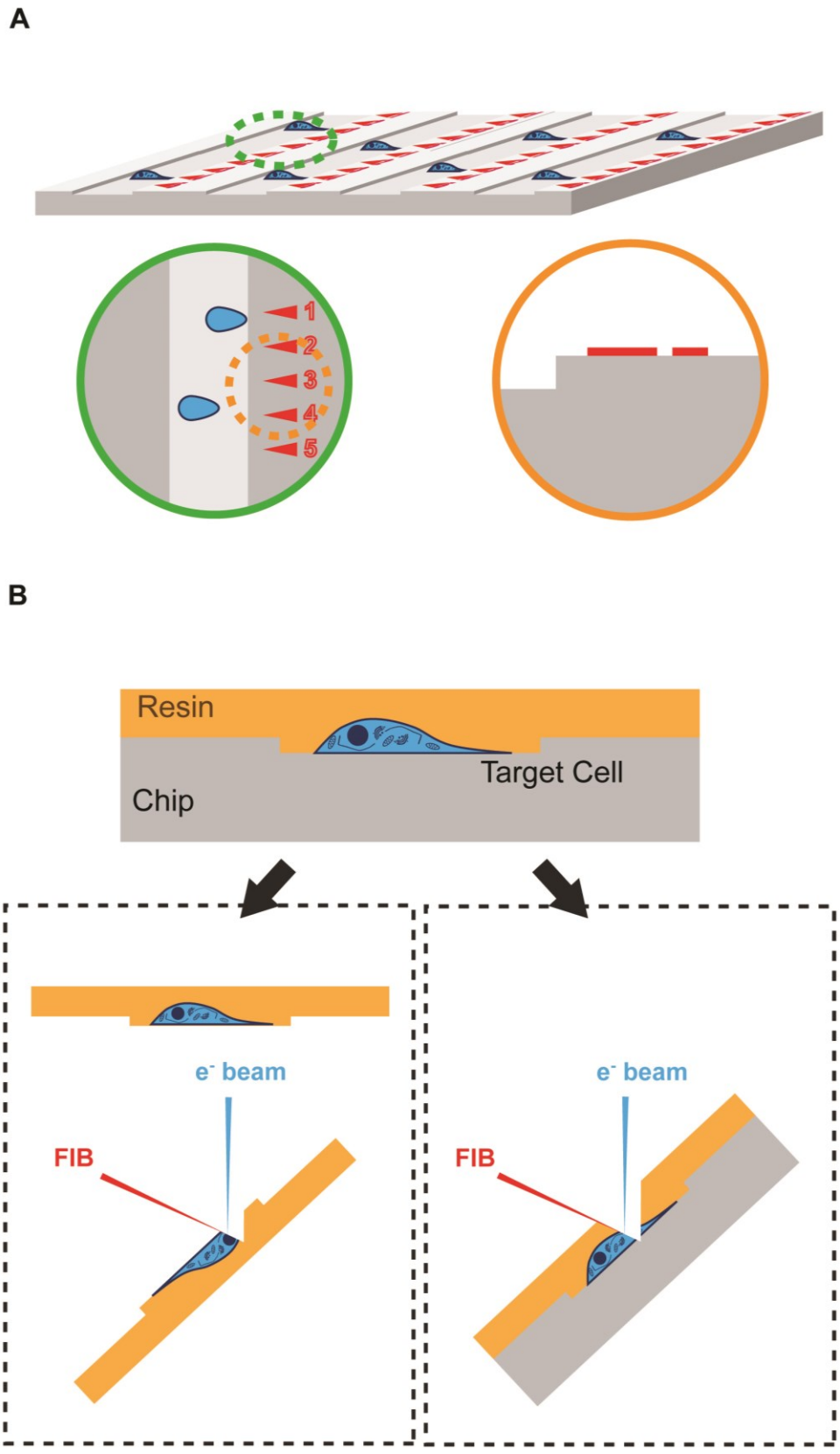

Figure 24: Set-up of the photonics chip with landmarks. A) Chip with landmarks and waveguides on which cells are growing. B) Cell embedded in resin on top of chip. Taking off resin embedded cell from chip and milling from the bottom (left) or directly milling from the top (right).

Several resins enabled the visualization of the landmarks, but only in the regions without cells. We tried the less viscous Spurr (Spurr, 1969), which is mostly used for plant material, and that has been successfully used for FIB-SEM imaging (Kremer, Lippens *et al.*, 2015), and we tested the combination of Spurr with EPON (Bhawana, Miller *et al.*, 2014). Because Spurr resin can easily be drained away after the infiltration, its use made it possible to directly see the cells in the SEM (Figure 25 D and E), but it did not allow stable, continuous milling in the FIB-SEM **(**Figure 26 B). Due to strong interactions of the FIB with the resin and the biological material, a very hard resin is required to achieve steady, stable milling/acquisition. The interaction between the resin and the beam are actually causing a "waving" effect, (due to local shrinkage/expansion at the block surface, (Figure 26 B)). Initially, we used very hard EPON, but since it was producing artefacts while milling, we switched to Durcupan resin. Together with the resin formulation, we also experimented with different techniques to drain the resin from the sample. The first step was to tilt the photonics chips 90° and use gravity to let the resin drain (Figure 23 F). Since Durcupan is very viscous this did not lead to sufficient results. We thus tried manual removal of the resin with absorbent paper, which also did not give satisfying results. The combination of centrifugation for 30 min and slightly increasing the temperature to 30 °C helped to reduce the layer of resin on top of the cells to less than 2 µm, which made the landmarks visible in the SEM and allowed faster targeting (Figure 25 B inset). This part was essential for the manual targeting of the cells as well as opening up the possibility for automated targeting.

Table 6: Characterization of different resins

Resin	**Topological information**	**Visibility grid**	**Stability FIB-SEM**
75 % Durcupan	yes	yes	no
90 % Durcupan	yes	yes	yes
100 % Durcupan	no	no	yes
Hard Spurr	yes	no	no
Extra Hard Spurr	no	no	no
Hard Spurr + 100 % Durcupan	yes	yes	no

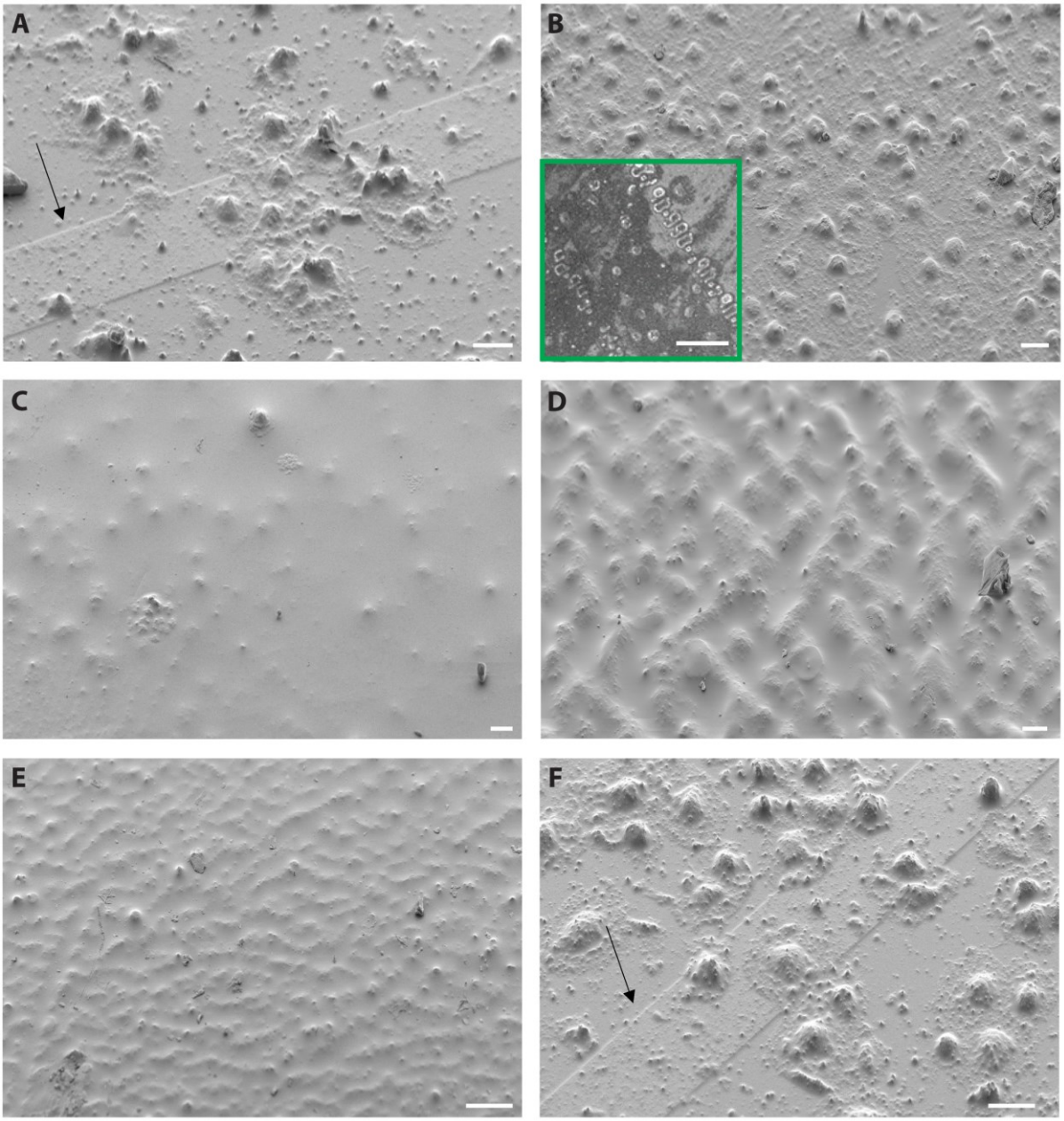

Figure 25: SEM view on photonics chip with LSECS comparing different resins. Final resin embedding step: A) 75 % Durcupan; scale bar 20 µm. B) 90 % Durcupan; scale bar 20 µm. Inset LSECs on landmarked waveguide with 90 % Durcupan; scale bar 50 µm. C) 100 % Durcupan; scale bar 20 µm. D) Hard Spurr; scale bar 20 µm. E) Extra hard Spurr; scale bar 100 µm. F) Hard Spurr + 100 % Durcupan; scale bar 20 µm. Black arrows point to the waveguide on the photonics chip. Processing of the cells was done by Randi Olsen from the EM facility at Tromsø University, Norway.

Even with this centrifugation, the use of pure resin formulations was not sufficient to obtain proper results (Table 6). It is finally with 90 % Durcupan in 100 % EtOH that we managed to drain enough resin (Figure 23 G) while preserving good cutting properties in the FIB-SEM (Figure 26 C).

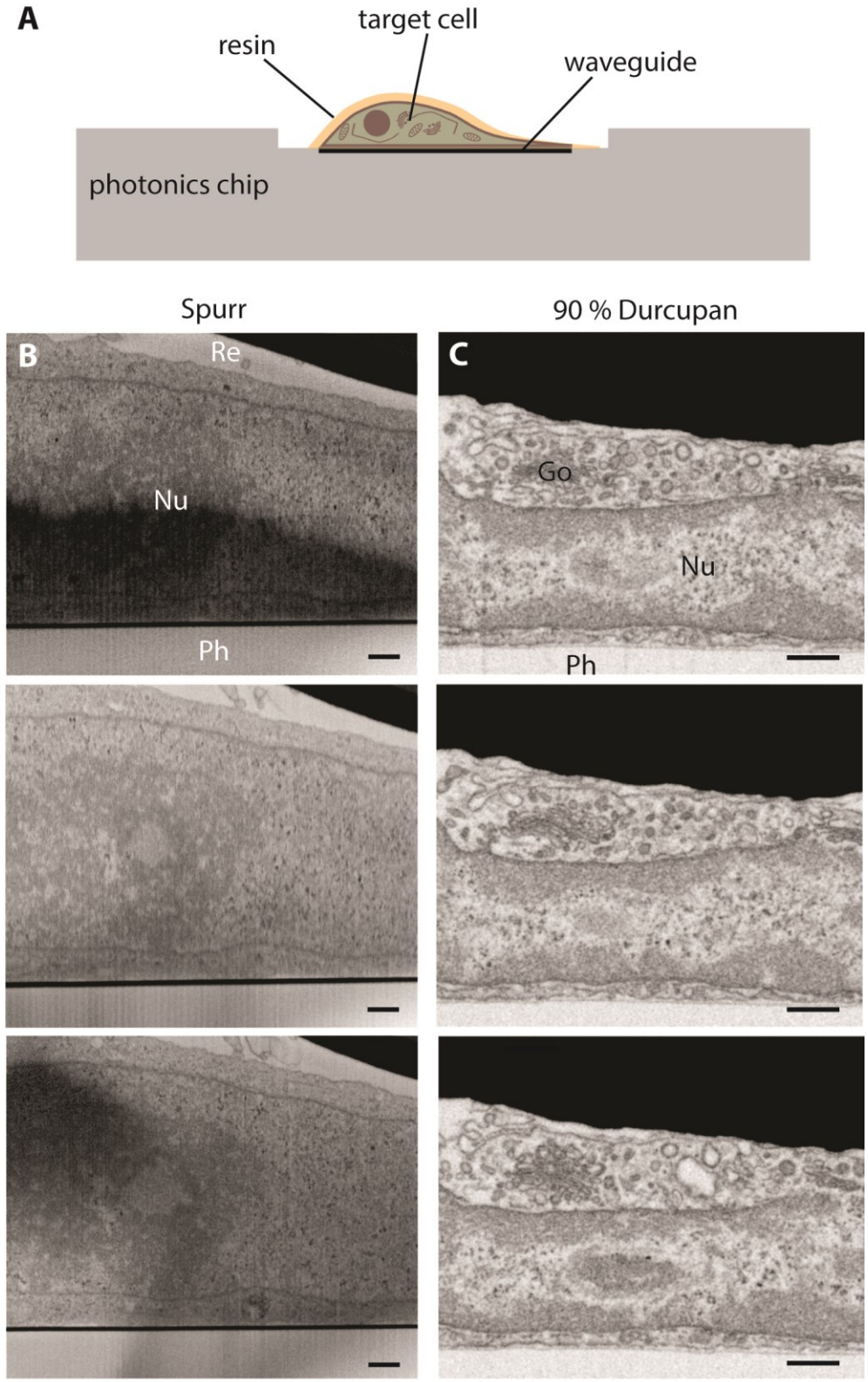

Figure 26: Comparison of milling behavior of different resins on photonics chip. Image series every 50 nm. A) Scheme of cell on photonics chip embedded in resin. B) LSEC on top of photonics chip embedded in Spurr (imaging: 5 nm x 5 nm x 10 nm); scale bar 500 nm. B) LSEC on top of photonics chip embedded in 90 % Durcupan (imaging: 5 nm x 5 nm x 8 nm); scale bar 500 nm. N = nucleus, Ph = photonics chip, Re = resin, G = Golgi apparatus.

One important goal of a CLEM experiment is to use information from both imaging modalities to target specific cells, but also to precisely identify organelles or subcellular structures. Fluorescently tagged affinity markers are powerful for distinguishing such features when used in LM and can serve as reference points for registering LM and EM images. (Figure 23 D and 27 A). To get the best ultrastructural preservation possible, we did not want to use permeabilizing reagents that allow certain dyes to enter the cell. The actin staining (Phalloidin 488) and the membrane stain (CellMask^{TM} orange) can enter the cell without permeabilization. Fluorescently-labeled, formaldehyde-treated serum albumin (AF647-FSA) was used to follow endocytosis. In the FM images, the CellMask^{TM} orange revealed the rims of the fenestrations of the LSECs, which was used to overlay and register the FM data to the EM images (Figure 27 C). A FIB-SEM stack of 2000 images was acquired at the ROI, with a 5 nm x 5 nm x 8 nm voxel size. By simple thresholding in Amira (FEI) and by looking at the x/z surface instead of the x/y slicing plane, the fenestration of the LSECs became nicely visible (Figure 27 B). To be able to identify the compartments where the FSA had gone to, the lysosomes/endosomes were segmented in Amira, because they are potential end points of the FSA trafficking (Figure 27 E). The overlay with the LM images was a little bit more challenging, because a proportion of lysosomes identified by EM did not show up as a signal in the LM. Besides the clear separation of the individual lysosomes by the EM, this could not confidently be done with the LM data (300 - 350 nm resolution). In the end, we could show as a proof-of-principle a CLEM pipeline from waveguide imaging on the LM on LSECs to getting ultrastructural information from the FIB-SEM acquisition of the same cell. This has great potential linking super-resolution imaging on a photonics chip to full cellular architecture as seen in the FIB-SEM. Future projects might involve looking at different steps of virus entry into the cells. So far, all the targeting was done manually, but with the development of our CLEM workflow (chapter 2) in combination with the precise landmarks on the chip, such approaches will be fully automated (chapter 2).

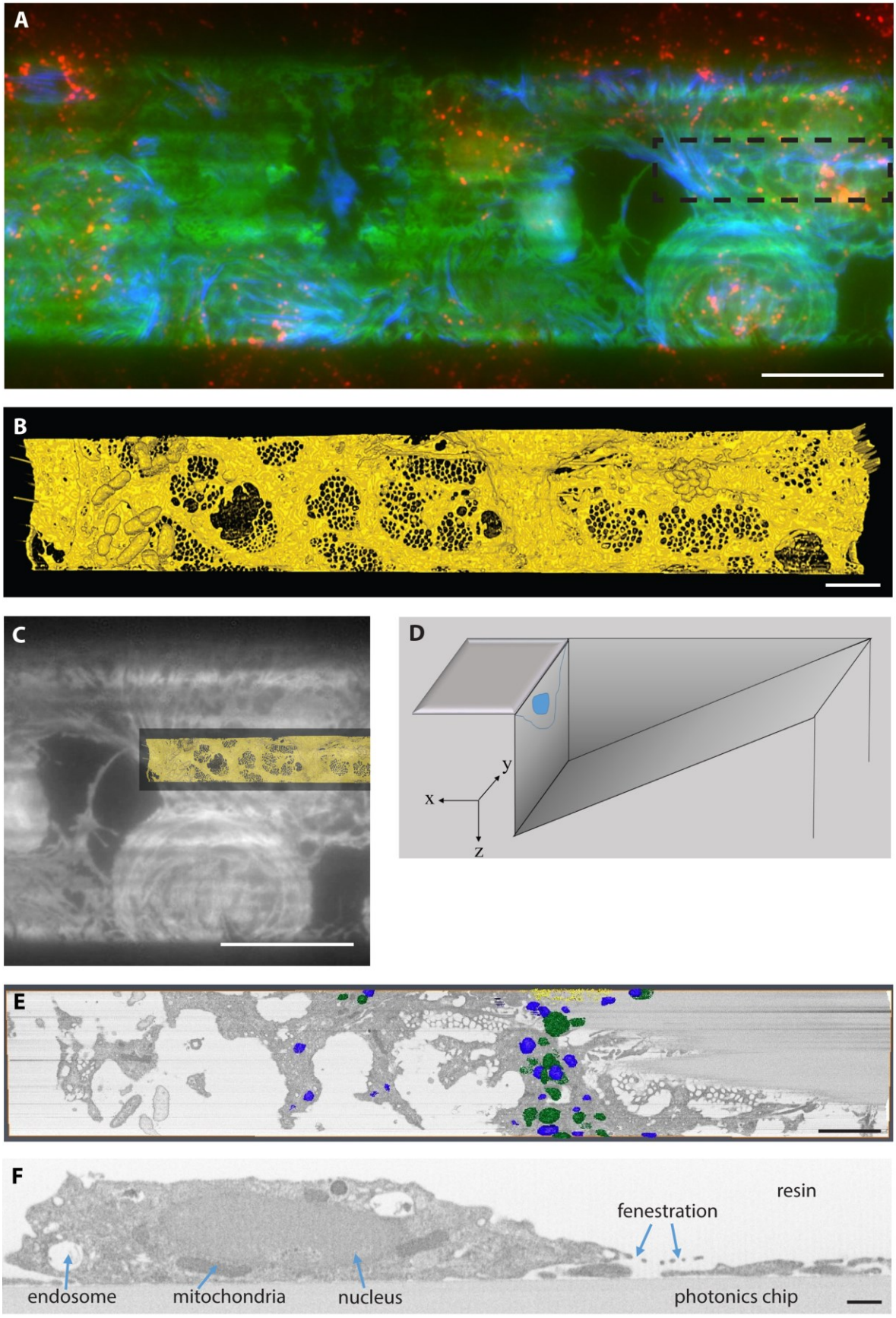

Figure 27: Workflow CLEM on chip.

Figure 27 (previous page): A) Overlay different channels light microscopy (green = cell mask orange, blue = actin, red = lysosomes)dotted square is the acquired region in the FIB-SEM and corresponds to B; scale bar 20 µm. B) Model of EM data segmented in IMOD and visualized in Amira; scale bar 2 µm C) Overlay 60x CellMask^{TM} orange (gray) with model of EM data (yellow). D) Labeling scheme of the different axis of a dataset inside the FIB-SEM. E) Virtual slice through EM data with modeled lysosomes in Amira (blue = electron dense, green = empty); scale bar 2 µm. F) EM image of LSEC; scale bar 500 nm.

3.3 Methods

3.3.1 Cell extraction and staining

Rat liver sinusoidal endothelial cells (LSECs) were prepared by collagenase perfusion of the liver, low speed differential centrifugation and Percoll gradient sedimentation (Smedsrod and Pertoft, 1985), followed by the depletion of Kupffer cells (KC) by seeding the nonparenchymal fraction onto plastic culture dishes. The KCs are faster to attach, therefore the suspension is enriched with LSECs. After coating the waveguides with fibronectin (which was not necessary for our experiments with HeLa cells), the cells are incubated for 1 h at 37 °C. Non-attached cells were washed off, which was followed by another 1h of incubation. To follow the endocytosis pathway cells were treated with fluorescently-labeled, formaldehyde-treated serum albumin (AF647-FSA, 50 µg/ml) for 1 min at 37 °C, washed with PBS, and incubated at 37 °C for 2 h. The cells were washed once and fixed with 2.5 % glutaraldehyde, 4 % formaldehyde and 0.05 % malachite green in 0.1 M cacodylate buffer for 15 min at RT. The plasma membrane was stained by incubating the cells for 10 min at RT with CellMask^{TM} orange 561 (1.25 ng/ml in PBS). The actin filaments were stained by incubating cells for 45 min at 37 °C with Alexa Fluor 488 Phalloidin (1:40 dilution in PBS).

3.3.2 Waveguide imaging

The waveguides with the fixed cells were imaged on a custom-made microscope, where light is coupled to the waveguide by illuminating it from the side. Cells were imaged with a 4x, 20x and 60x (1.2 NA, water immersion) objectives. After imaging, the chips were submerged again in fixative containing 2.5 % glutaraldehyde, 4 % formaldehyde, 0.05 % malachite green in 0.1 M cacodylate buffer.

3.3.3 Waveguide processing for electron microscopy

All processing was done in a Ted Pella microwave with a cold stage. Because the PIC were overheating upon microwave processing, the samples were placed directly on the cold stage, set to 4 °C, and the vacuum chamber was inverted on top. The cells were fixed for 14 min (2 min vacuum on-off-on-off-on-off-on, 100 W) and washed two times with 0.1 M cacodylate buffer. Post-fixation was done with 1 % Osmium tetroxide, 1 % $K_3Fe(CN)_6$ in 0.1 M cacodylate. The cells were post-stained with 1 % tannic acid and 1 % uranyl acetate. Samples were then dehydrated in ethanol and embedded in Durcupan. To be able to remove as much resin as possible, the resin exchange steps went up to 90 % Durcupan in EtOH and not 100 %

Durcupan. The chip was centrifuged for 30 min at 37 °C to further remove excess resin and polymerized in the oven for 96 h at 60 °C. The chips were then cut to a final size of 1 cm² to fit the SEM stubs.

3.3.4 FIB-SEM acquisition

FIB-SEM imaging was performed as described in 2.3.8.

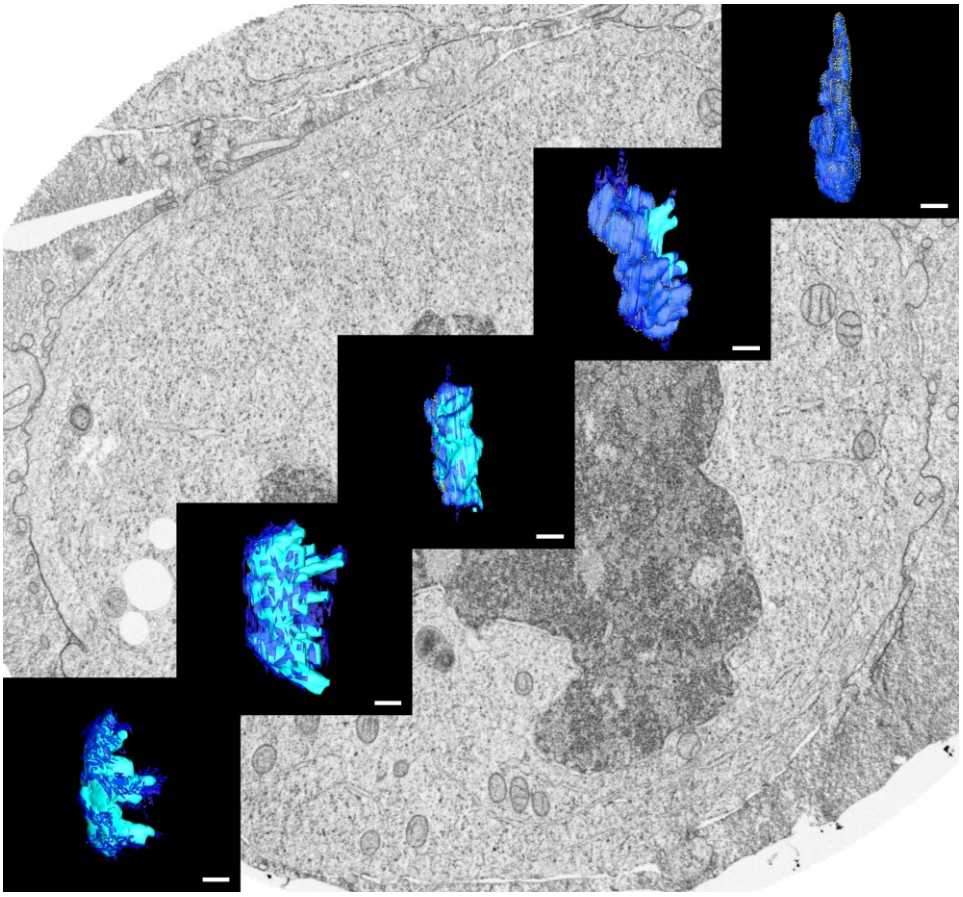

Chapter 4: Nuclear envelope assembly during mitosis

Cover image: EM image of mitotic cell in the background with 3D models of HeLa cells at different time points throughout anaphase (light blue chromosomes, dark blue NE).
The QR code is a link to the supplementary videos (#2), also available following this link: **http://tinyurl.com/Steyer-videos**

4.1 Introduction

In the previous two chapters, we have seen how CLEM could be used on adherent cultured cells to screen for large populations and image as many selected cells as possible. By doing so, the need to screen for large surfaces or the use of a photonics chip for doing super-resolution imposed the choice of chemical fixation as a method to prepare the samples for EM.

However, CLEM is also adapted to other fixation methods, such as high-pressure freezing. Whilst requiring culture substrates of rather small diameter (5 mm compared to >10 cm with chemical fixation), HPF is the method of choice for preserving the ultrastructure (Steinbrecht and Müller, 1987).

To challenge the capabilities of CLEM combined with volume EM imaging in this context, we decided to collaborate with the Ellenberg lab (EMBL, Heidelberg). The project of investigating the re-formation of the nuclear envelope and the nuclear pores upon mitosis is challenging on different levels asking for local (TEM tomography) and global imaging (FIB-SEM) to answer different questions. Since TEM tomography has a very limited field of view, we chose the FIB-SEM for its ability to image the complete cellular architecture at high-resolution. Indeed, volume imaging allowed us to simultaneously visualize the ER, the chromosomes (core and non-core region), the distribution of the nuclear pore complexes (NPCs) and the newly formed nuclear envelope (NE) and its connections to the ER. Moreover, when used in a CLEM workflow, we were able to capture rare events in anaphase, such as the very few connections between the ER and the NE or the fenestration of the seldom sheets of ER attaching to the chromosomes that will probably give rise to the newly formed NE.

This project was also a good opportunity to explore the solutions for image analysis in order to improve the segmentation and quantification of various subcellular compartments. One of the technical challenges was the sample itself. Mitotic cells are only loosely in contact with the substrate, therefore they are more likely to detach during the EM processing and be lost. Moreover, unlike fully adhered cells, they are hardly visible at the block surface when observed in the scanning EM, while we have seen in chapter 2 (Figure 10 C-E), that having access to the cell profile could enhance the chances to precisely locate the cells of interest before starting a FIB-SEM run. Since high-pressure freezing is keeping samples closer to native state than chemical fixation, this is very interesting to explore potential ways to adapt high-pressure freezing for our automated CLEM pipeline.

In all eukaryotic cells, the NE plays a crucial role in separating the nucleoplasm from the cytoplasm. The NPCs function as gateways between the inside and the outside of the nucleus, enabling selected travelling of macromolecules (Rabut, Lenart *et al.*, 2004). Structural biology has been elucidating the structure of the NPC in great detail using cryo-electron microscopy (Kosinski, Mosalaganti *et al.*, 2016; von Appen and Beck, 2016), but it is still not fully understood how the different components assemble and disassemble in time and space. Although many sub-complexes and different configurations have been studied on a more static basis, looking at time points is more difficult. For this reason, the assembly process of the NPCs has been highly debated in the field.

In the last 15 years, two distinct models have emerged that describe the timing of the NPCs assembly (Wandke and Kutay, 2013). In the enclosure model, the NPCs assemble on top of the bare chromosomes before the ER encloses around them to form the NE (Wandke and Kutay, 2013). In the insertion model, the ER forms the NE first followed by the insertion of the NPCs. Another highly debated topic is the formation of the ER that is wrapping the chromosomes. Different studies have suggested that ER tubes (Anderson and Hetzer, 2007) or sheets (Lu, Ladinsky *et al.*, 2009) are enclosing the chromosomes. Earlier *in vitro* studies with purified *Xenopus* egg extracts were even implying vesicles being responsible for the formation of the NE. More recent studies have shown evidences that ER sheets are responsible for the reformation of the NE during mitosis (Lu, Ladinsky *et al.*, 2011). However, so far no conclusive evidence has been provided that shows how the nuclear pores form at the end of mitosis and how the ER forms the NE.

Here, a combined approach was taken using electron tomography (Shotaro Otsuka, Ellenberg lab, EMBL) to have a closer look at the local morphology of the forming NPCs, and FIB-SEM to look at the global changes to the ER, NE and the chromosomes. Correlative light and electron microscopy uniquely allows to follow the progression of the anaphase *in vivo* using LM, and then freeze the cells at specific time points using HPF for subsequent high-resolution imaging using electron microscopy. Correlative light and electron microscopy was used to first image specific time points (with 12 seconds temporal resolution) throughout anaphase in the LM. The cells were then HPF to arrest the ultrastructure and were later found back in the electron microscope. This opened up the possibility to look at the detailed changes the chromosomes are going through, the shape of the ER/NE, the formation of the nuclear pores as well as their absolute number and the connections to the ER. This is the first time-resolved study zooming in on the formation of the nuclear pores and the NE during mitosis at the ultrastructural level also looking at the full cellular context at high-resolution.

4.2 Results and Discussion

We have combined the power of fluorescence microscopy (FM) to target specific time points during mitosis with electron tomography (done by Shotaro Otsuka, Ellenberg Lab, EMBL Heidelberg), to look at the composition of the nuclear pore, and FIB-SEM to look at the global changes of the chromosomes, ER, nuclear envelope (NE) and the nuclear pores (Figure 29 and Figure 30).

Two strategies were followed to target individual cells by CLEM. As we decided to fix them by high-pressure freezing, the correlation coordinate system had to be adapted to the sapphire disks, the culture substrate of choice for HPF. We have used carbon coated coordinates systems (Figure 28 A and B) or laser etched sapphire disks (Figure 28 E and F). Whilst the etched marks are transferred to the block surface, and are therefore visible in the scanning EM, the carbon layer does not produce any topology. For this reason, we had to introduce an intermediate step when transmitted light microscopy is used to visualize the coordinate system in the resin block and to reproduce part of the landmarks by laser etching (Figure 28, B-D). The precision of the targeting was such that many mitotic cells, at different time points of the anaphase, could be recovered for in depth analysis.

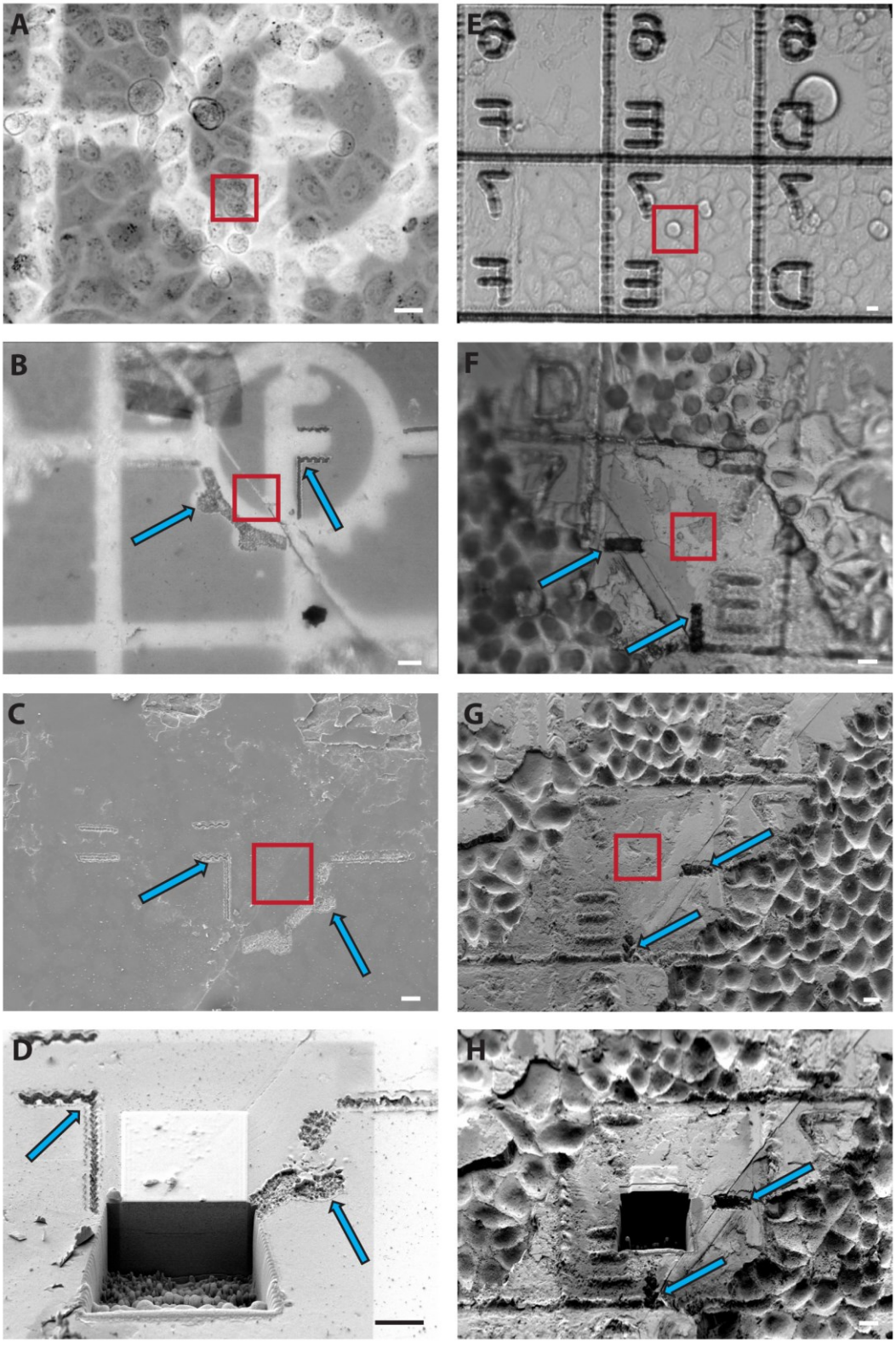

Figure 28: Branding to target cells in the SEM. Targeting 6.3 min mitotic cell on a sapphire disk coated with carbon finder grid (A-D), branding is indicated by blue arrows: A) LM image of cells. B) LM image after branding. C) SESI image inside SEM of branding. D) SESI image of deposition and trench; scale bar 20 µm. Targeting 3.1 min mitotic cell on etched sapphire disk (E-H): E) LM image of cells. F) LM image after branding. G) SESI image inside SEM of branding. H) SESI image of deposition and trench; scale bars 20 µm.

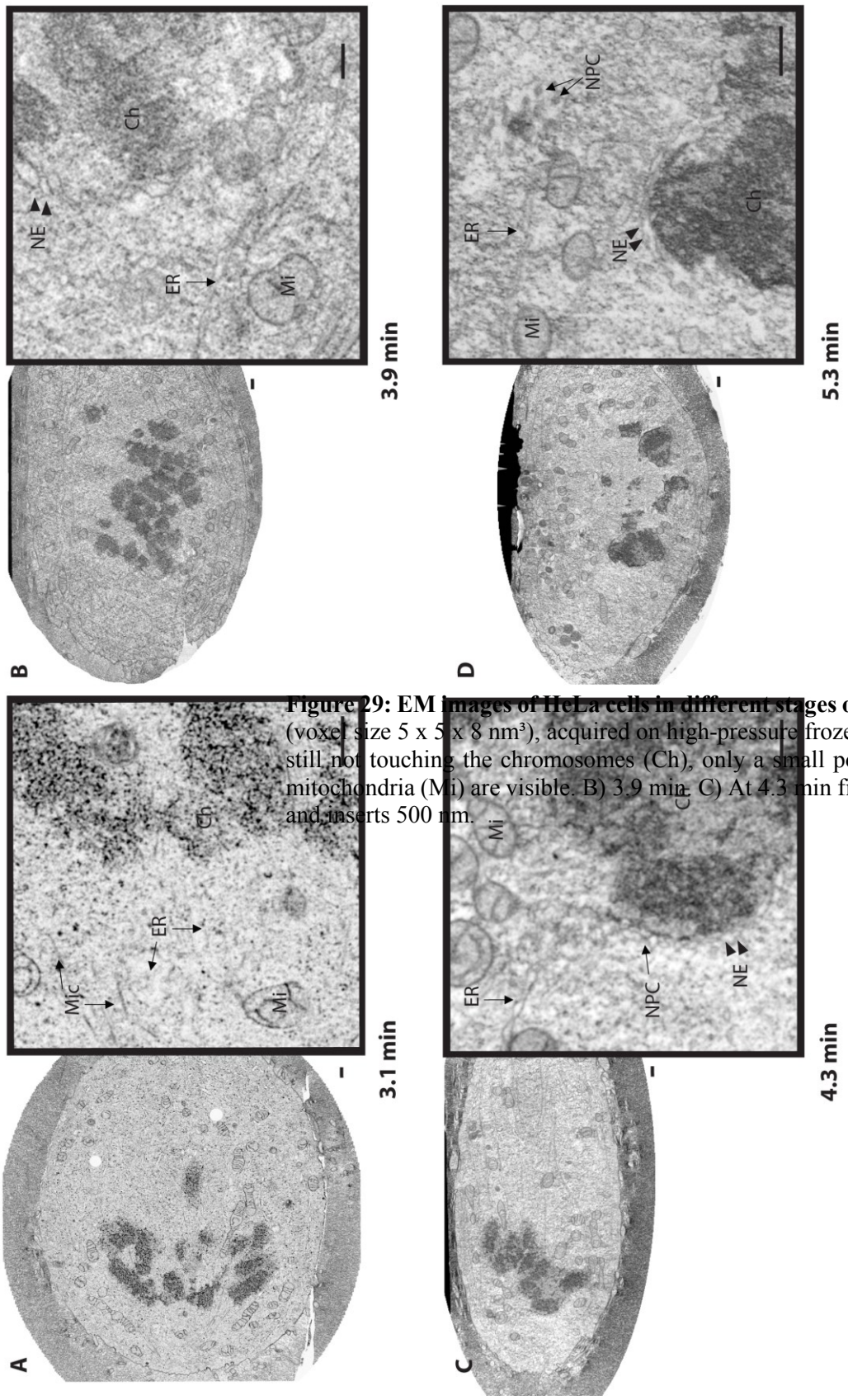

Figure 29: EM images of HeLa cells in different stages of anaphase 3.1 min - 5.3 min.
(voxel size 5 x 5 x 8 nm³), acquired on high-pressure frozen, freeze-substituted cells at d
still not touching the chromosomes (Ch), only a small portion has attached as nuclear
mitochondria (Mi) are visible. B) 3.9 min. C) At 4.3 min first nuclear pores (NPCs, arrow
and inserts 500 nm.

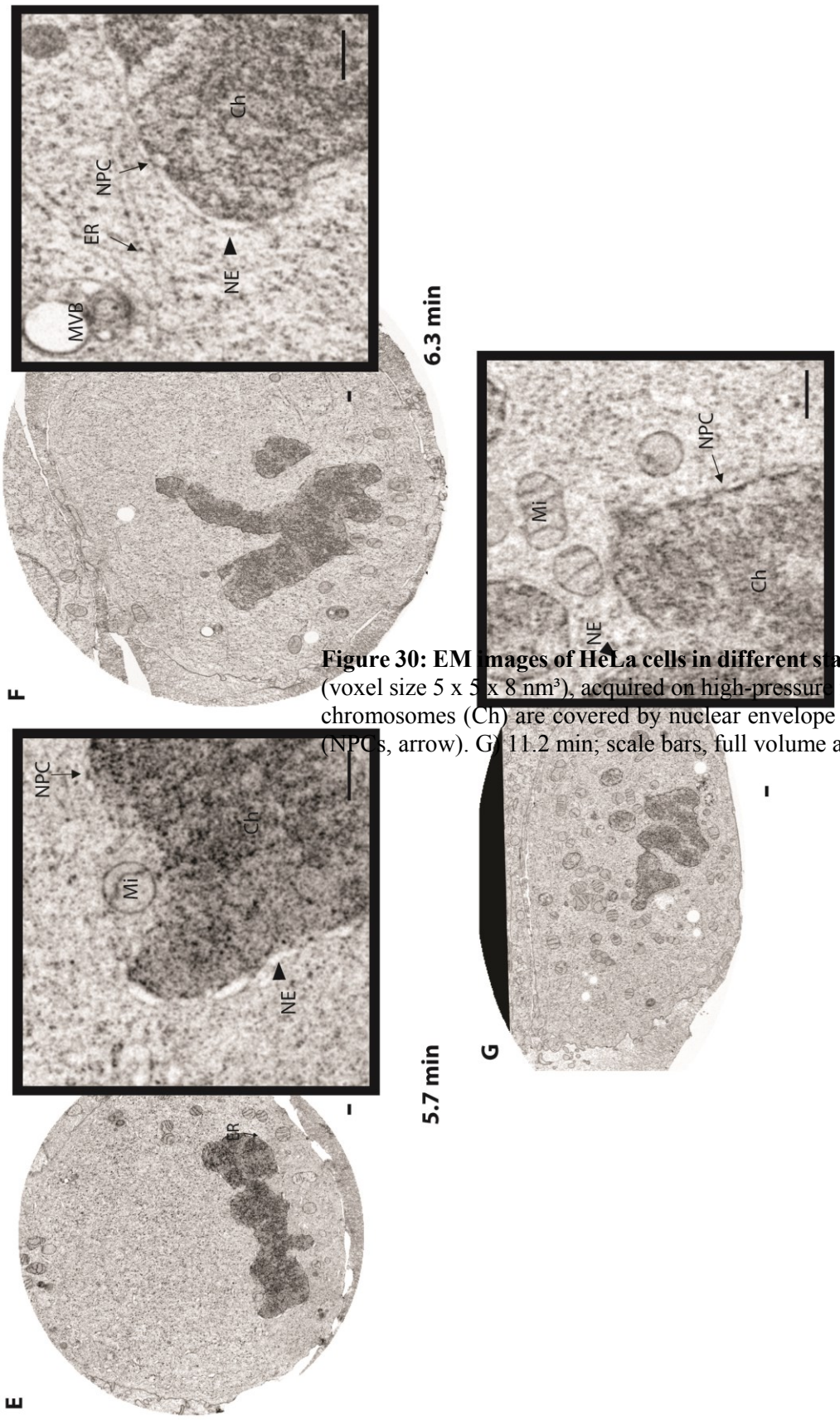

Figure 30: EM images of HeLa cells in different stages of anaphase 3.1 min - 5.3 m
(voxel size 5 x 5 x 8 nm³), acquired on high-pressure frozen, freeze-substituted cells a
chromosomes (Ch) are covered by nuclear envelope (NE, arrow head). Microtubule
(NPCs, arrow). G: 11.2 min; scale bars, full volume and inserts 500 nm.

At 3.1 min time point after anaphase onset (Figure 32: panel A), the two sets of chromosomes were still quite close together. The ER was organized in an extensive network of sheets located underneath the plasma membrane and presenting fenestrations of variable diameter (ranging from 40-2000 nm). Since there were still microtubules between the chromosomes, no ER elements were found at the core region in between the chromosomes. At 4.3 min into anaphase (Figure 29 B) the chromosomes were pushed further to the outside and made more contacts with the ER. At 4.3 min, there were only 42 pores visible on a NE surface area of ~84 µm². At around 5.3 min into anaphase (Figure 29 C), the ER was covering half of the surface of the chromosomes with ~163 µm² NE and 10 times more pores had assembled (359 at 5.3 min). Interestingly, the nuclear pores were not distributed homogeneously along the newly formed NE, but rather appeared first in the non-core regions that were covered by ER. At 5.3 min, there were only two connections to the ER. Moreover, the connections were made by fenestrated ER sheets touching the non-core regions. After 6.3 min (Figure 29 D), about 90 % of the chromosome surface was covered with ~847 µm² NE and the number of nuclear pores had increased by a factor of 5 (1744 at 6.3 min, Figure 33 B). Then, outer core regions were also covered with NE, but the core region between the sets of sister chromosomes were still devoid of NE. After 11.2 min, the entire surface of the chromosomes was covered with ER/NE and the nuclear pores were starting to spread a more homogeneously across the nuclear surface (Figure 29 E). Over the time course of anaphase, we first saw naked chromosomes that were getting closer to the fenestrated ER. After about 4.3 min, the ER started wrapping the chromosomes and we started seeing nuclear pores in the NE. Within the next 3 min there was a massive increase of nuclear pore number and almost the entire chromosome were being covered with NE within 11.2 min.

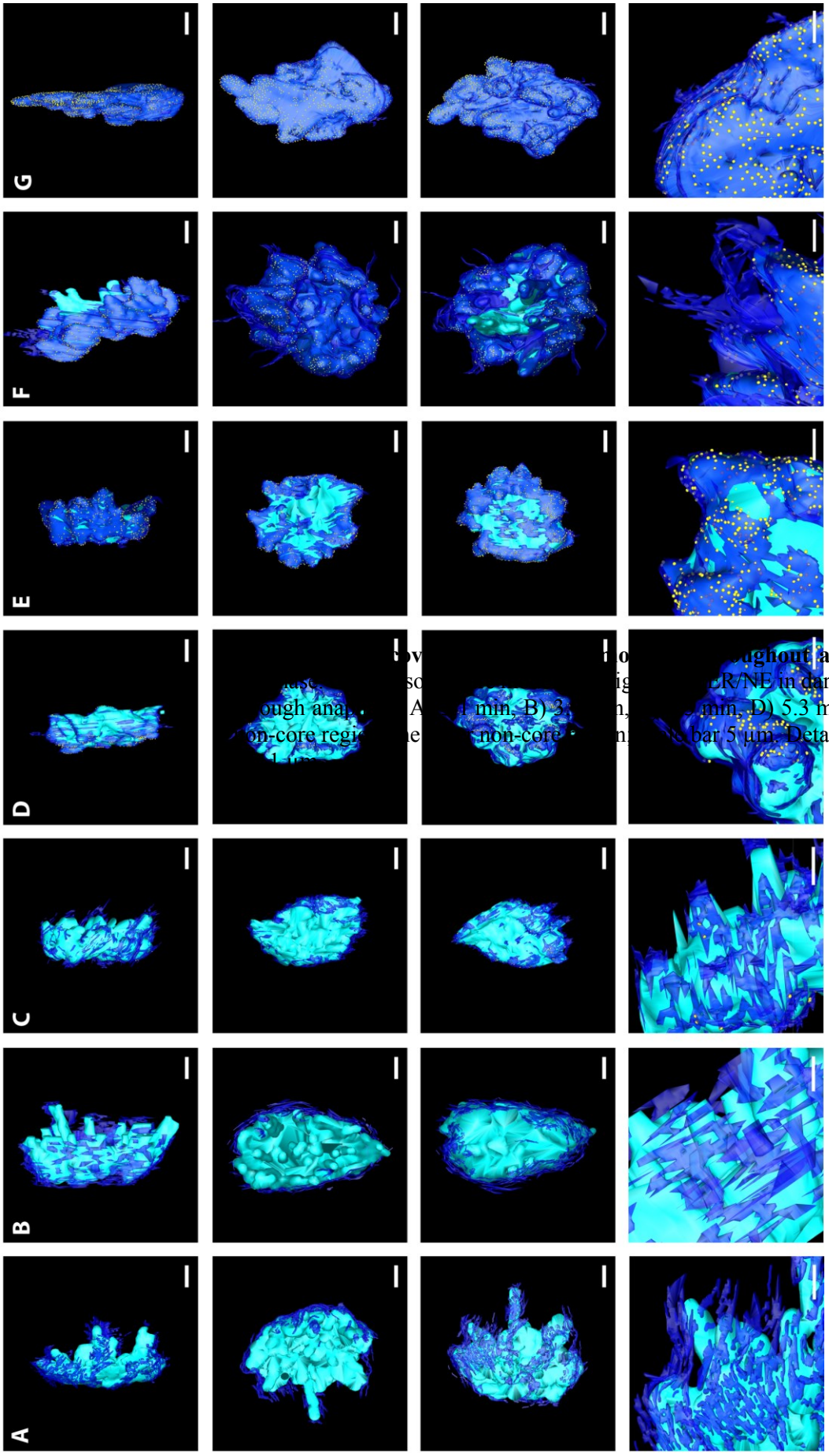

ughout anaphase. Models based on
ER/NE in dark blue and nuclear pores in ye
min, D) 5.3 min, E) 5.7 min, F) 6.3 min ar
bar 5 µm. Detailed look at the fenestration o

Together with the overall changes of the chromosomes and ER/NE, we also investigated the local changes of the ER and the assembly steps of the nuclear pore complex. The ER exists mainly as fenestrated sheets in HeLa cells, and the size of the holes vary considerably. When the ER starts touching the chromosomes at around 3.1 min, the size of the holes began to decrease and at around 4.3 min the smaller holes were being filled with nuclear pore proteins.

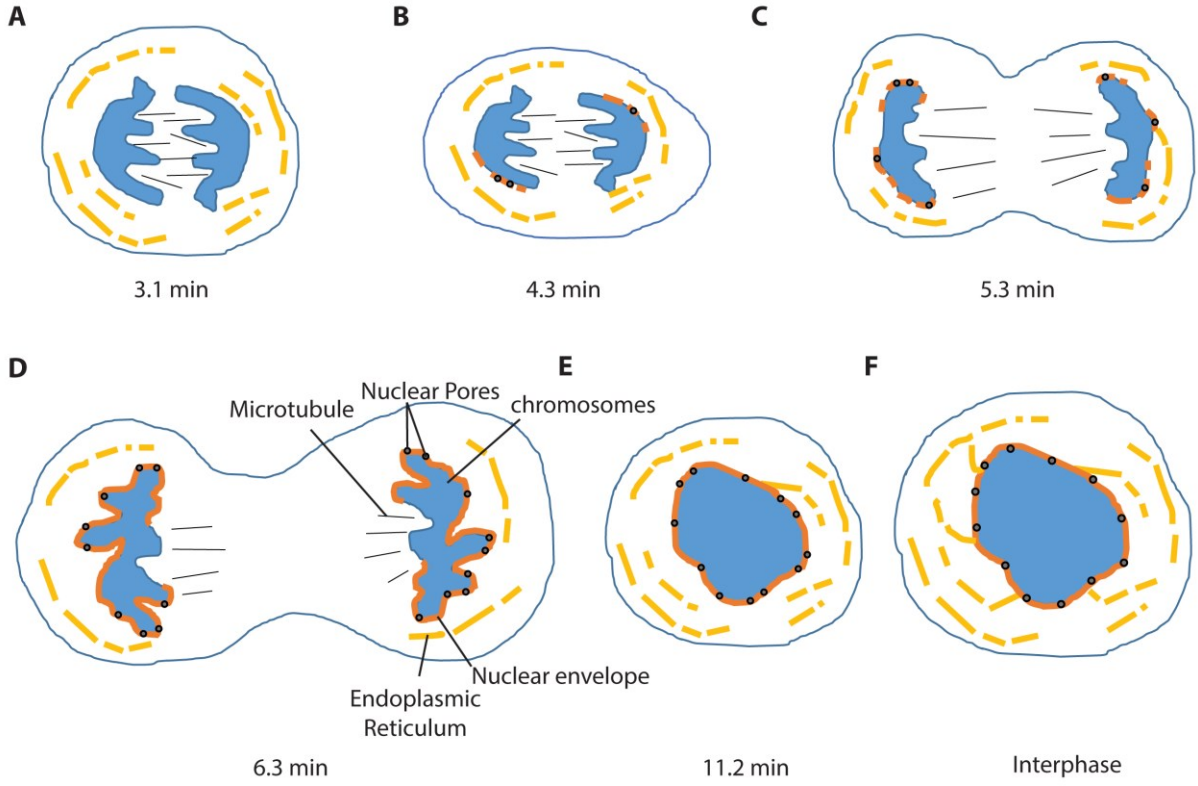

Figure 32: Changes of ER, chromosomes and nuclear pores throughout anaphase based on our observations. A) At 3.1 min into anaphase ER (yellow) is getting closer to the chromosomes (blue). B) At 4.3 min into anaphase the microtubules kept on pushing the chromosomes to the outside and ER was starting to form the NE (orange) attached to the chromosomes, first nuclear pores appeared (black dots). C) At 5.3 min the chromosomes were covered with more NE (orange) and more NPCs were especially at the non-core regions, there were some connections to the ER. D) At 6.3 min most of the chromosomes, except the core region facing the sister cell was covered with NE. E) At 11.2 min the nucleus was fully enclosed by NE and most NPCs were apparent. F) In Interphase there were quite a lot of connections between the ER and the NE (~110 connections).

The first nuclear pore proteins that are assembling are the NUP 107-160, followed by NUP 93, NUP 62 and NUP 153. NUP 358 arrives only at the very end of mitosis (Antonin, Ellenberg *et al.*, 2008). This mechanism of the nuclear pore complex assembly seems to be quite different to the process during interphase. Previous work has shown that during interphase, a mini-pore is formed at the nucleoplasmic side inside an intact nuclear membrane (Otsuka, Bui *et al.*, 2016). Progressively, the mini-pore is growing and the two membranes of the NE are pushed together until the mature pore arises. During mitosis, however, our findings indicate that the

fenestrated ER, which contributes to the NE formation, progressively fills its openings with NPC components. There was no point in time when we saw a fully closed NE without holes or nuclear pores. It is still possible that pores precursors are first forming on the bare chromosomes. However, we cannot confirm or reject this hypothesis since the resolution of neither FIB-SEM nor TEM tomography was high enough to distinguish electron density of putative nuclear pores from the density of the chromosomes. From a kinetic point of view, it seemed to be more achievable to have the pre-made holes in the NE, than to create 2500 pores *de novo* within 10 min. During interphase, for example, the production of 2500 pores and their insertion into the NE takes about 50 min (Otsuka, Bui *et al.*, 2016). Another striking difference between anaphase and interphase cells was the amount of connections between the ER and the NE. While we have estimated the amount of ER/NE connections to be in the order of 110 (from FIB-SEM data obtained on two independent cells) during interphase, at the different time points in anaphase there were only between 1 and 12 (Figure 33 C). Another compelling difference between anaphase and interphase was the distribution of nuclear pores. At the beginning of anaphase, nuclear pores appeared first in the non-core regions and seemed to distribute more evenly until the end of anaphase. The manually segmented models of the full cell, ER/NE, chromosomes and nuclear pores were used for a general understanding of the organization of these parts during the different time points in anaphase (Figure 32).

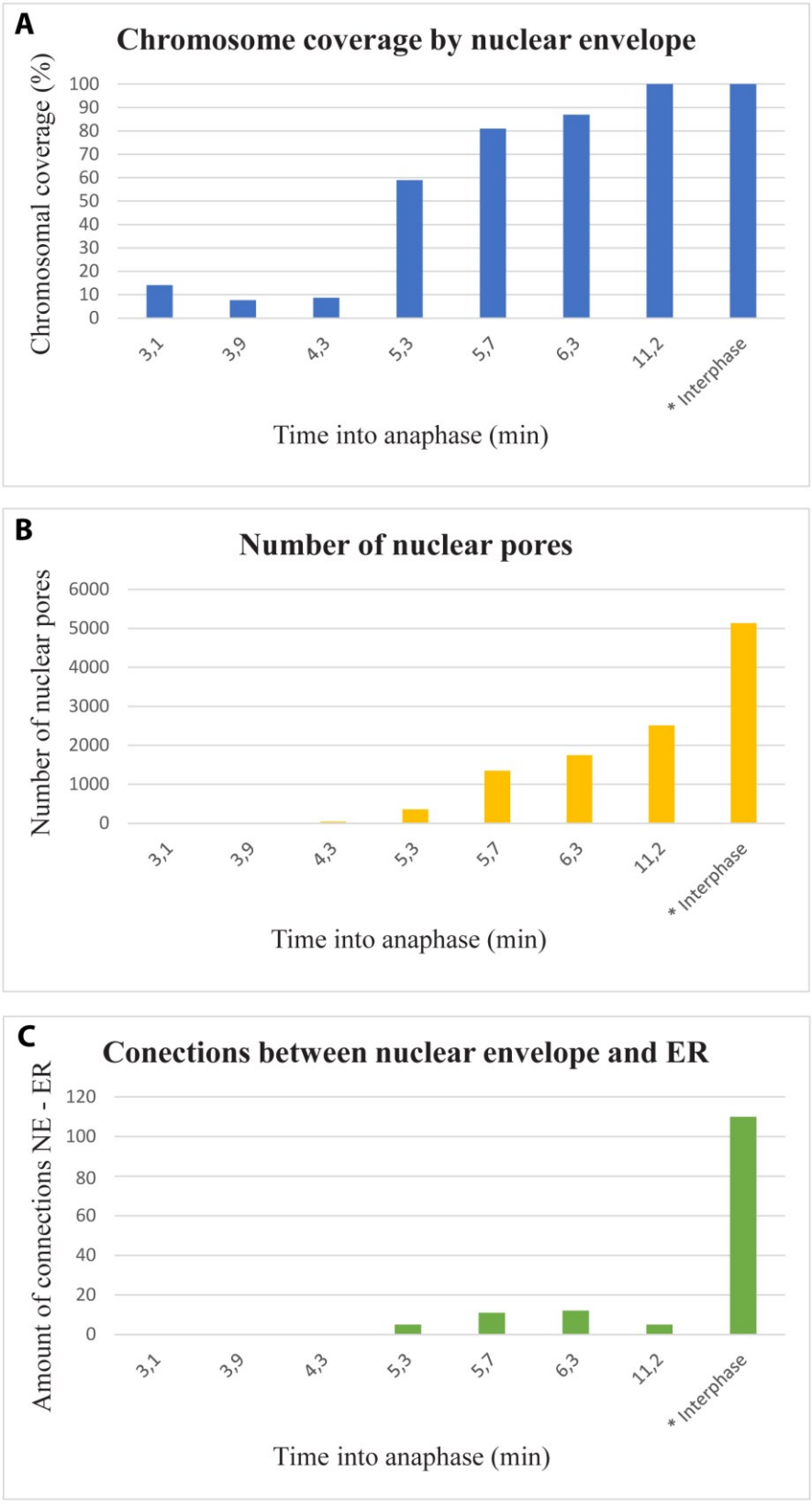

Figure 33: Quantification of chromosomal coverage, number of NPCs and NE-ER connections throughout anaphase. Different parameters were followed throughout anaphase. A) Percentage of the chromosome surface covered by nuclear envelope. B) Amount of NPCs. C) Number of connections between the NE and the ER. *Interphase cell had (extrapolated) number of ~110 connections.

The chromosome NE-coverage and the number of nuclear pores, as well as the amount of contacts between the ER and the NE were measured from the model obtained by manual segmentation of the FIB-SEM datasets. Since for those models only every 10-20th slice (*i.e.* a z-step of 80-160 nm) of the FIB-SEM dataset was segmented and then the segmentation was interpolated between slices, the precision for small openings was not that accurate. For a more detailed understanding of the fenestration of the ER, and to allow extracting more precise numbers, we decided to investigate the use of automated segmentation. For our datasets complete automatic segmentation was not possible, all datasets were cleaned up manually after doing semi-automated segmentation (Figure 34, more details see 4.3.6). We took 250 slices of the central part of half of the chromosomes to do a slice by slice segmentation for the first 6 time points here there are still openings in the NE (Figure 34). The detailed segmentations of the NE (Figure 34) will be used to investigate further the closing of the NE and the relationship between hole size/fenestration of the ER and the NE and the different classes of fenestration size over the different time points. The ER is highly fenestrated, when it comes in contact with the chromosomes (Figure 34 A) and eventually all the holes are closed to form the interphase NE.

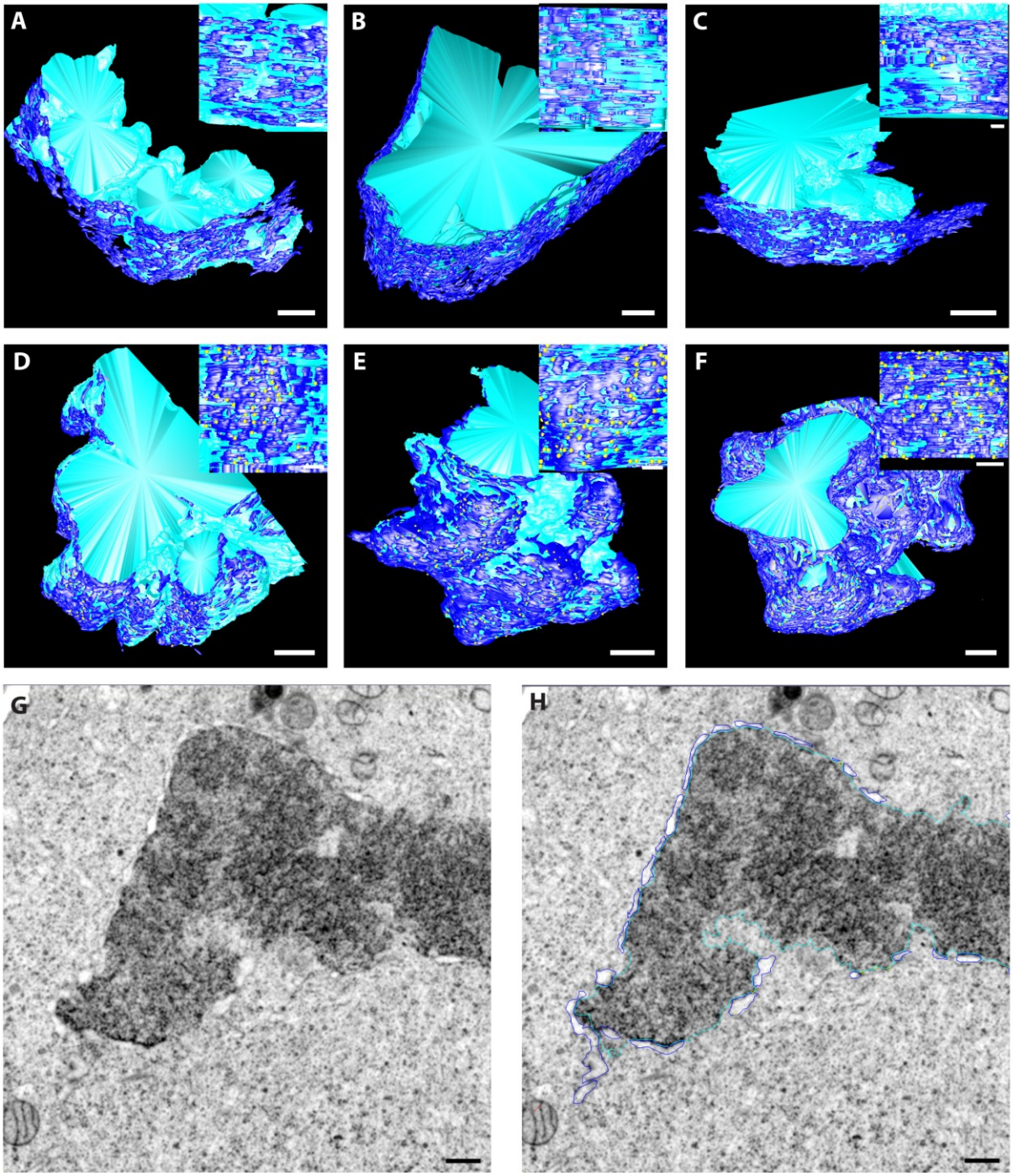

Figure 34: Detailed segmentation of the NE at different times during anaphase. Chromosomes = light blue, ER/NE dark blue, NPCs = yellow: A) 3.1 min, B) 3.9 min, C) 4.3 min, D) 5.3 min, E) 5.7 min and F) 6.3 min into anaphase; scale bar 1µm. Inset zoom on fenestration of the ER/NE; scale bar 500 nm. A)-C) and F) scale bar 0.5 µm, D) + E) scale bar 0.2 µm. G) EM slice of 5.7 min dataset. H) Segmentation of NE (dark blue) and chromosomes (light blue) with NPCs within the next 10 slices shown as yellow circles; scale bars 300 nm.

4.3 Methods

4.3.1 Cell culture

Hela Kyoto cells were cultured in DMEM supplemented with 10 % fetal calf serum (FCS), 2 mM L - glutamine, 1 mM sodium pyruvate, 100 U/ml penicillin and 100 µg/ml streptomycin. For correlative light and electron microscopy, cells were grown on etched sapphire disks or on sapphire disks (0.16 mm thick, 3 mm diameter; Wohlwend GmbH, Sennwald, Switzerland) patterned with a finder grid by carbon coating.

4.3.2 Live cell imaging

At least 30 min before the start of the experiment, the medium was replaced by imaging medium (IM; a CO_2-independent medium without phenol red (Invitrogen) containing 20 % FCS, 2 mM L-glutamine, 100 µg/ml penicillin and streptomycin). Imaging was performed in a microscope-body-enclosed incubator at 37 °C, mounted on a widefield microscope (Axio Observer Carl Zeiss, Oberkochen, Germany) using 10× objective (Carl Zeiss). Mitosis was monitored every 12 sec by time-lapse imaging.

4.3.3 Sample preparation for electron microscopy using a high-pressure freezer

At different cell cycle stages the cells were cryo-immobilized using a high-pressure freezer (HPM 010; ABRA Fluid AG, Widnau, Switzerland). The cells were immersed in IM containing 20 % Ficoll (PM400; Sigma Aldrich) as a cryo-protectant, right before freezing. The samples were freeze substituted using an automatic freeze substitution unit (Leica EM AFS) and were incubated with 1 % OsO_4, 0.1 % uranyl acetate and 5 % H_2O in 100 % acetone at -90 °C for 24 h. The temperature was raised from -90 °C to -30 °C (5 °C/h), kept at -30 °C for 3 h and then raised to 0 °C (5 °C/h). The samples were washed with 100 % acetone, infiltrated with increasing concentrations of Durcupan in acetone (25 %, 50 % and 75 %) and finally embedded in 100 % Durcupan. The polymerization was carried out at 60 °C for 4 days.

4.3.4 Preparation for FIB-SEM acquisitionn

The sapphire disk was removed, with the cells remaining at the surface of the Durcupan block. The block containing the cells was coarsely trimmed down with a handsaw to about 2 mm height (Villinger, Gregorius *et al.*, 2012). In the next trimming step razor blades were used to trim the cells opposing surface as parallel as possible to the block-face. To be able to target the chosen cells in the SEM, marks were branded on the surface of the resin disk using an Olympus

Biosystems Cut^R with a pulsed 355 nm laser (motorized XY-stage) and a 20x objective. The program Xcellence cell^frap was used to perform the laser branding. A pattern was created in the experiment manager to brand a pattern that is pointing to the region of interest using the Frap function (laser 5 %). The branded pattern from the LM is later on visible on the surface of the sample inside the SEM, which can then be used to target the ROI to acquire EM data.
To be able to target the correct cells inside the FIB-SEM, laser brandings were introduced at the surface of the resin block as described in 4.2 (Figure 28).

4.3.5 FIB-SEM acquisition

The resin disk containing the cells was mounted on a conductive carbon sticker (12 mm, Plano GmbH) that was placed on SEM stubs (6 mm length, Agar Scientific). If necessary, the parallel alignment between the disk and the SEM stub was done using small wedges of polymerized Durcupan (Figure 35).

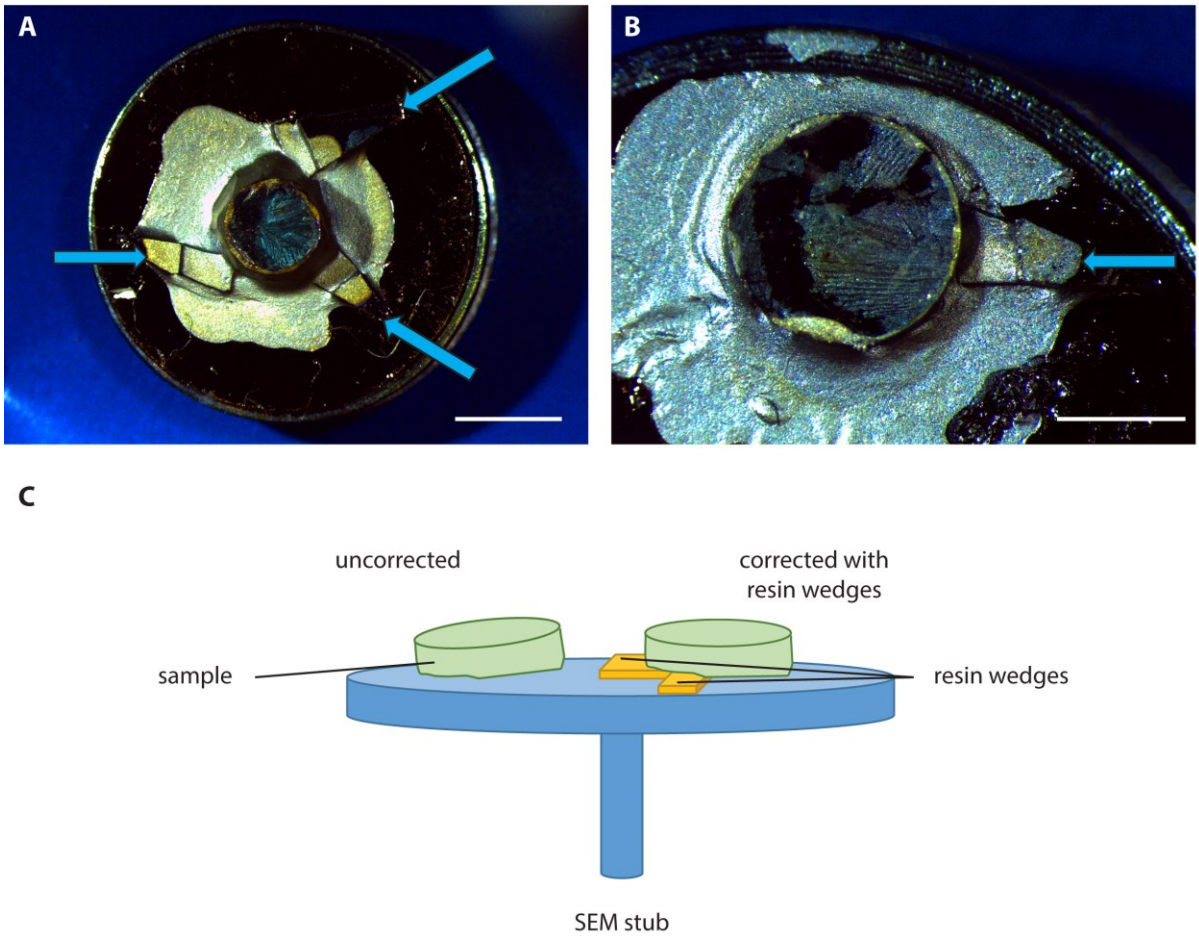

Figure 35: Sample preparation for high-pressure frozen cell monolayers. Samples on SEM stub mounted with resin wedges (blue arrows) to make the top surface parallel to the SEM stub. A) Scale bar 3 mm and B) Scale bar 1.5 mm: C) Illustration of how to mount the sample with resin wedges.

To limit charging by the electron beam during SEM imaging, the samples were surrounded by silver paint and coated with gold for 180 sec at 30 mA in a sputter coater (Quorum, Q150R S). The samples were introduced into the Auriga 60/Crossbeam 540 (Zeiss, Germany) and positioned so that the sample was facing the SEM at an angle of 36° and the FIB at an angle of 54°. ATLAS 3D, part of Atlas5 software (Fibics, Ottawa), was used to prepare the sample for "Slice & View". The laser branding was used to find back the region of interest and to position the milling and acquisition areas. The ion beam was used to dig a trench in front of the ROI with 15 nA to reach a depth of 20 µm. Next, the image-surface was polished at 3 nA, for imaging, the FIB was set to a 1.5 nA current, and SEM imaging and FIB milling took place simultaneously (Narayan, Danielson *et al.*, 2014). The images were acquired at 1.5 kV with the Energy selective backscattered (EsB) detector with a grid voltage of 1.1 kV, the analytical mode at a 700 pA current, and setting the dwell time and line average so that the frame-time added up to 1.5 min.

4.3.6 Image analysis and segmentation

The acquired raw FIB-SEM data were aligned using TrackEM2 (Cardona, Saalfeld *et al.*, 2012) inside Fiji (Schindelin, Arganda-Carreras *et al.*, 2012). After alignment, the stack was cropped, gray levels were inverted and the images were smoothened within Fiji (3 x 3 mean filter). For some datasets with stationary noise (mainly vertical stripes), the VSNR (Variational Stationary Noise remover) Fiji plugin was used to reduce the effect (Fehrenbach, Weiss *et al.*, 2012). The full datasets were segmented manually in IMOD (Kremer, Mastronarde *et al.*, 1996), whereas some parts of the datasets were segmented semi-automatically in more detail using Ilastik and MIB. Matlab (R2016a; Mathworks, USA) will be used to extract measures from the detailed segmentation.

We were working on automating the segmentation as much as possible and on getting more detailed segmentation on every slice (Figure 34). One of the first challenges for the software/computer was the size of the datasets (20-50 GB). Different programs allowed opening of the full dataset, but it was not possible to do any 3D rendering or segmentation. In MIB/Ilastik on our workstations (64 GB RAM) 8 GB is the maximum the software can handle at once for segmentation. IMOD, which was regularly used for segmentation, has no features for automation. In MIB it is possible to chop a dataset into smaller portions, segment different parts and merge them back together again afterwards. But this process was tedious and had not yielded satisfying results. Another possibility was to run the software on a cluster with higher computing capabilities, but the two programs used by us at the time were not optimized to be used on a cluster and the system at EMBL was not meant for GUI-based, user-interacting software. Therefore, we decided to only use a representative part of the dataset, spanning core and non-core region in the center of one set of daughter chromosomes (250 slices, 5 nm x 5 nm x 8 nm, < 0.5 GB). We tried Ilastik, which is an interactive image segmentation and analysis software (http://ilastik.org/index.html) used on EM data mostly for reconstructing neuronal networks (Sommer, Straehle *et al.*, 2011; Kreshuk, Koethe *et al.*, 2014; Maco, Holtmaat *et al.*, 2013; Andres, Koethe *et al.*, 2012; Plaza, Scheffer *et al.*, 2012). It allowed to integrate image analysis tools and different filters to segment specific structures. Based on machine learning, Ilastik is supposed to be trained by the user in order to process volumes. We also tried MIB (Microscopy Image browser), which is an "advanced image processing, segmentation and visualization software" (http://mib.helsinki.fi), used for cellular structure-function relationships of cells and cell organelles (Belevich, Joensuu *et al.*, 2016; Joensuu, Belevich *et al.*, 2014; Furuta, Yadav *et al.*, 2014; Majaneva, Remonen *et al.*, 2014). We have

tried to combine the two approaches, in constant exchange with the developers, to first extract features with MIB that would help annotating in Ilastik. In a second step Ilastik would automatically segment the MIB annotated structures. In a last step, the segmentation is cleaned up manually in MIB. The second challenge we encountered was the inability to apply a single, optimized segmentation-pipeline to datasets acquired at different time points during anaphase. The slight variation in contrast levels, and the different organization of the ER/NE and the chromosomes, required cumbersome adjustment of the pipeline's parameters and more often demanded manual segmentation of the objects. In conclusion, at this time the automated segmentation procedures are not applicable to complex and heterogeneous objects in datasets such as those used in our work. The datasets up to 5 min, where the ER is not yet firmly attached to the chromosomes, had to be manually segmented in MIB, since the automatic recognition of ER/chromosomes in Ilastik did not work. Datasets after 5 min, where ER has turned into NE firmly attached to the chromosomes, were labeled in the pixel classification pipeline in Ilastik. In Ilastik the user is able to train on a couple of slices of a dataset different objects and have the software predict on other slices of the dataset. In the end, Ilastik creates a probability map storing the probability for each single pixel/voxel to be foreground (part of the object). Through thresholding this map can now be used to filter out foreground (object) and background. The probability maps for the chromosomes, the NE and the cytosol were exported to MIB. Furthermore, the remaining imprecise labelling was removed manually in MIB. If MIB is solely used, big datasets can be imported, chopped, segmented and reassembled later.

In this part of the project it became clear again, that a lot of softwares are still quite limited in the amount of data they can handle. Some have the option of a big data package (Amira) or they can be run in a batch/headless mode on a cluster (Ilastik). Different softwares allow segmentation, but have different tools to make it easier and/or automate it.

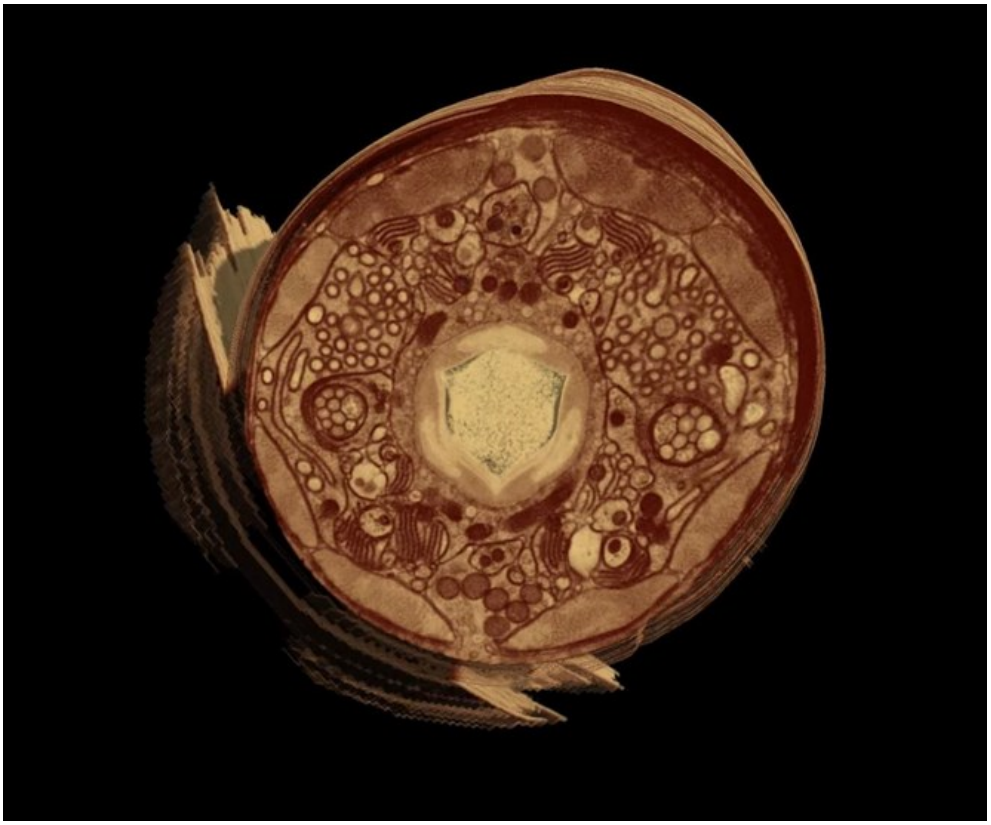

Chapter 5: Anatomy of *C. elegans* dauer larvae

Cover image: Image from thresholded EM data from *C. elegans* FIB-SEM dataset, Zeiss Crossbeam540.

The QR code is a link to the supplementary videos (#3), also available following this link: **http://tinyurl.com/Steyer-videos**

5.1 Introduction

In the previous chapters, we have seen how powerfull the combination of CLEM and volume EM was to access the ultrastructure of specific cells, as selected from heterogeneous monolayers by mean of light microscopes. Both imaging techniques have also been used on multicellular model organisms, but most often separately. Our goal was to combine them on a powerful model system: the nematode *Caenorhabditis elegans*. *C. elegans* is commonly used to understand the organization of neuronal networks and their link to behavior, especially because the genetic modification of these animals is quite easy to achieve (Brenner, 1974). With a nervous system composed of only 302 neurons, *C. elegans* is one of the few organisms where the full connectome has been traced (White, Albertson *et al.*, 1978; Po, Hwang *et al.*, 2010). In addition to having a low number of neurons, the worm is quite easy to cultivate and in most cases the anatomy is very similar between individual animals. Up until now most research has been focused on the adult worm as well as some of the different larval stages (L1/L2). In parallel to their normal life cycle, these nematodes are able to persist in an alternative developmental stage called the dauer stage, where the worm is completely self-sufficient. *C. elegans* worms enter this life stage upon starvation, overpopulation or high temperatures (Cassada and Russell, 1975). Furthermore, the signal to enter into the dauer stage is transferred via nematode specific pheromones. All worm stages produce ascarosides (group of glycolipids, containing ascarylose, found in some nematodes), with the exception of the dauer stage (Kaplan, Srinivasan *et al.*, 2011). Nevertheless, it has been shown that an increasing amount of pheromones and decreasing amounts of food lead to a rise in amount of dauer stages (Golden and Riddle, 1982). During this stage, the worm does not take up food nor chemicals from the outside and can survive for up 2-4 months (instead of just a couple of days for adults). Another striking fact is that the dauer larvae do not seem to age, which made this specific larval stage an interesting research model for studying aging. The laboratory with which we are collaborating has undertaken a thorough study of this stage, focusing especially on a comparative description of its neuro-anatomy across different larval stages and transitions. One of the biggest questions related to that topic is how the dauer larvae sense when there is food available again, while it looks like they are completely closed to the outside. Therefore, the sensory neurons (AFD, AWA, AWC) would be considered good candidates to look at. FIB-SEM uniquely provides the resolution in x, y and z to map the neurons throughout the worm and visualize the complexity of the network in full. The results of our work revealed for

the first time the full head anatomy of a dauer stage worm at close to isotropic resolution, which also made it possible to more accurately trace the connectome. The diameter of some neuron extensions is so small (down to a few nanometers) that they can only be revealed by EM. Although *C. elegans* is a small nematode (adult: 80 µm diameter/1150 µm length, dauer: 15 µm diameter/400 µm length) imaging it fully at high-resolution with volume EM could become overwhelming in time (head alone more than a week per animal) and in data size (in the TB range). Therefore, precise targeting appears as a good solution for restricting the acquisition to specific ROIs in the FIB-SEM. Here, we developed an approach to quickly and efficiently visualize and target specific parts of the nematode in the SEM. This enables to study the ultrastructure of this powerful model system during the dauer stage, but also in other stages of the *C. elegans* life cycle. A better understanding of the anatomy of the worm will give first insides into what might be happening during the dauer stage and how *C. elegans* manages to return to the normal larval stages on its own.

5.2 Results and Discussion

5.2.1 Minimal Resin embedding of C. elegans

Electron microscopy in 3D has already been performed on *C. elegans* L1/L2 larvae (Nelson, Albert *et al.*, 1983) or young adult mostly by manual serial sectioning (Hall and Russell, 1991). In a recent study combining array tomography (see chapter 1) and super-resolution, data on the connectome were complemented with the network of electrical synapses (gap junctions, Markert, Britz *et al.*, 2016). The sensory system at the anterior part of the nematode has also been studied by serial imaging, revealing the fine anatomy of the sensory cilia and glia (Doroquez, Berciu *et al.*, 2014). In related nematode species, the connectome, as revealed by EM, was even correlated to behavior (Bumbarger, Riebesell *et al.*, 2013). However, one major technical bottleneck revealed by these approaches was the limited z resolution of ultramicrotomy based serial sectioning (30 to 50 nm at best) while some neurites would have thinner diameters. As a consequence, parts of the connectome still remained ambiguous. FIB-SEM appeared as a unique solution to this. As little was known about the neuro-anatomy of dauer stage, we decided to benefit from this technique to undertake a fine description of the anterior part of the animal. The first step was to adjust the sample preparation techniques to make targeting easier. The *C. elegans* worms were high-pressure frozen and freeze substituted (protocols 5.3.2 - 5.3.3), for optimal preservation of their ultrastructure. We have seen in the chapter 3 that it was possible to remove large amount of the resin surrounding adherent cells. As a result, the overall topology of the monolayer was clearly visible by SEM after polymerization of the resin. Following the same concept, we decided to adapt the protocol to the nematodes. This minimal resin approach allowed direct visual inspection of the surface of the worm in the SEM (Figure 36) revealing damaged specimens or allowing a precise orientation of the animal for FIB-SEM imaging. On the dauer stage of *C. elegans* features like the amphidial channels or the alae, a very distinctive pattern of a set of raised cuticular ridges that extend along both sides of the animal (Figure 36 B), are clearly visible and can be used as landmarks for precise anatomical targeting. Since the resin layer above the worm was very thin, it was even possible to see the furrows of the cuticle (Figure 36 A). Interestingly, we have used the same protocols for other model organisms such as zebrafish or *Platynereis* (Schieber et al in CLEM 3rd edition, by Paul Verkade Methods in Cell Biology, in preparation).

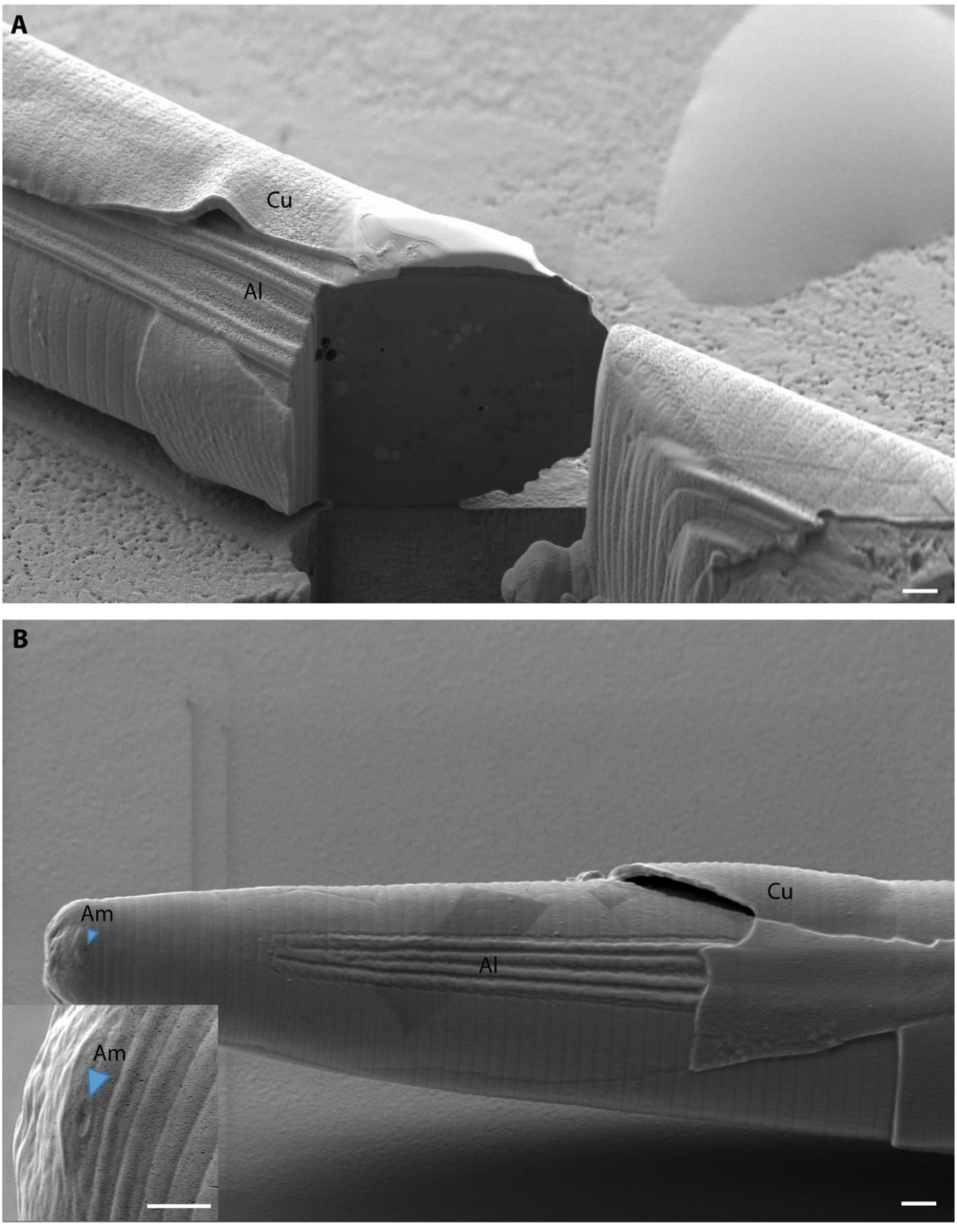

Figure 36: Minimal resin embedded worms. Dauer larvae after HPF and freeze substitution. Minimal resin embedding exposes many surface features that are used to target specific regions of interest (Al = alae, Cu = cuticle, Am = amphidial channels). A) FIB milling in the mid-body region exposes cross-section through the full diameter of the animal. B) Anterior part of the dauer larva; scale bar 2 µm. Inset: zoom on amphidial channel; scale bar 2 µm.

We tried several ways to drain as much resin as possible (Figure 37), whilst laying the samples on fine needles is efficient on rather large specimens (*e.g.* zebrafish done by Nicole Schieber, Figure 37 A), capillary forces are still too high when dealing with the small dauer larvae (Figure 37 A). Similarly, placing the worms on a piece of Aclar (copolymer film similar to plastic used in tissue culture; Scientific Services; Germany), which was mounted vertical, did not help to drain enough resin, (Figure 37 B). The best results were achieved by sliding the worms individually onto a piece of Aclar until most of the resin was gradually adsorbed at the surface of the film (Figure 37 C).

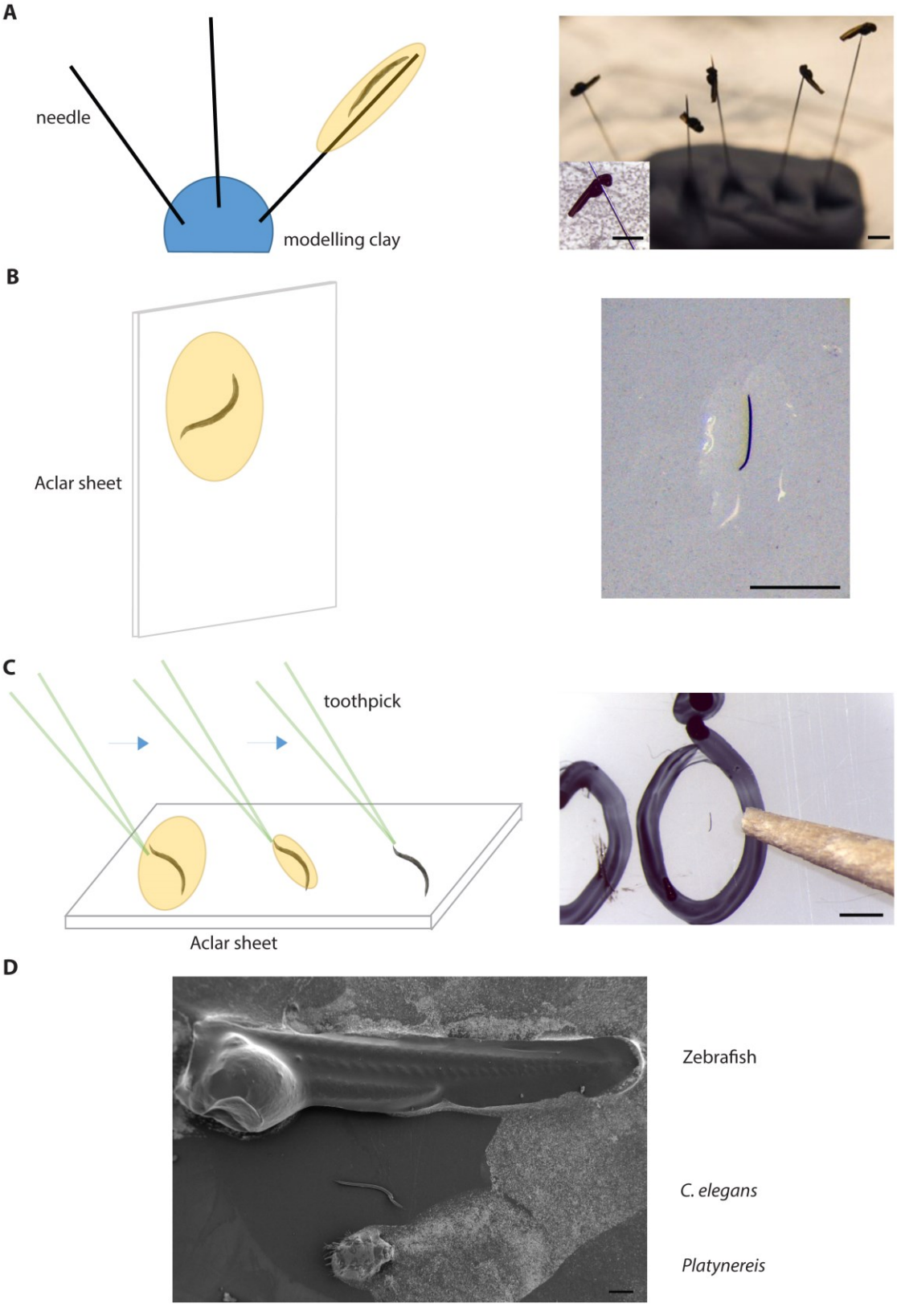

Figure 37: Minimal resin different techniques. A) Worms placed on needle to drain resin. Image of zebrafish placed on needle to drain resin; scale bar 1 mm. B) Worm placed on Aclar sheet sitting at 90° to get rid of resin. Image; scale bar 500 µm. C) Toothpick used to drag worm out of resin drop. Image; scale bar 1 mm. D) SESI image of a zebrafish, *C. elegans* and a *Platynereis* after embedding on SEM stub; scale bar 200 µm.

The infiltrated worms were left to polymerize on the Aclar film and then transferred to a SEM holder. In some cases, where the head was not directly touching the substrate (Figure 36 B), some resin was added to avoid chopping parts of the worm off while milling through it in the FIB-SEM. Since the resin layer was only a thin layer, the full anatomy of the worm was visible and distances could be measured directly. In order to acquire a dataset of the nerve ring and the neuronal connections towards the anterior part of the head, 80 µm were measured from the tip of the worm. With a security margin of ca. 15 µm, to allow proper stabilization of the microscope before imaging, a platinum layer was then deposited, followed by the digging of a trench (Figure 38 C-D). After polishing the cross-section through the worm, the acquisition was started. In the end a total of 10080 slices with 5 nm x 5 nm x 8 nm pixel size through 80 µm leading to raw data of about 1.5 TB were acquired over 8 days, see supplementary video #3. **http://tinyurl.com/Steyer-videos**

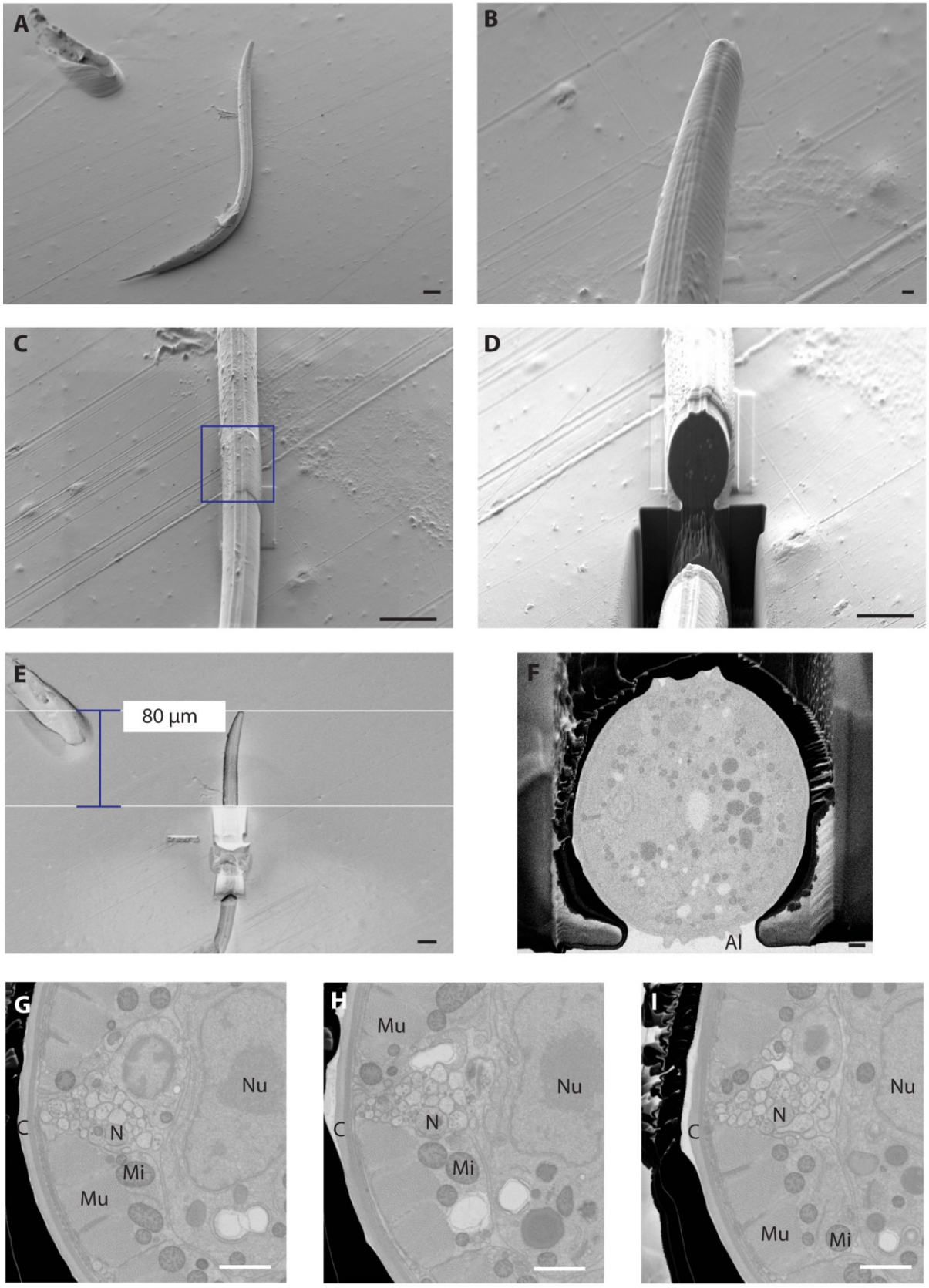

Figure 38: Process of targeting minimal resin embedded *C. elegans*.

Figure 38 (previous page): A) Full worm embedded in minimal layer of resin acquired in an SEM; scale bar 20 µm. B) Worm head; scale bar 2 µm. C) Deposition of platinum on worm indicated by blue box; scale bar 20 µm. D) Trench to expose cross-section through worm; scale bar 10 µm. E) Targeting of the nerve ring in the head of the worm; scale bar 20 µm. F) Cross-section through worm (Al = alae); scale bar 1 µm. G-I) Images through dorsal nerve cord (N) looking at synapses and dense core vesicles (C = cuticle, Mi = mitochondria, Mu = muscle, Nu = nucleus); scale bar 1 µm.

5.2.2 Anatomy of the head

Since there is only limited knowledge about the anatomical differences between the dauer and other larval stages of *C. elegans*, we decided to analyze the overall morphology and, more specifically, the neuronal connections. This was the first time that such a big part of one individual worm was acquired with close to isotropic resolution. The "full connectome" so far has been assembled from five individual adult worms using serial sectioning followed by TEM. The FIB-SEM allows better z-resolution, less deformation due to sectioning, less missing information between sections and easier alignment of the data. From the very tip of the head, a distance of 80 µm moving from posterior to anterior along the length of the worm was acquired at a 5 nm x 5 nm pixel size in x/y and a slice thickness of 8 nm (Figure 38). With this dataset, open questions in the field of connectomics could be addressed, since previously only serial sections of multiple worms were used to look at the wiring of *C. elegans* and the serial sections (40-70 nm) could not always unambiguously provide information about the neuron connections between sections. The very front of the worm head (first 10 µm) was segmented manually to be able to compare to a reference adult worm dataset (Doroquez, Berciu *et al.*, 2014).

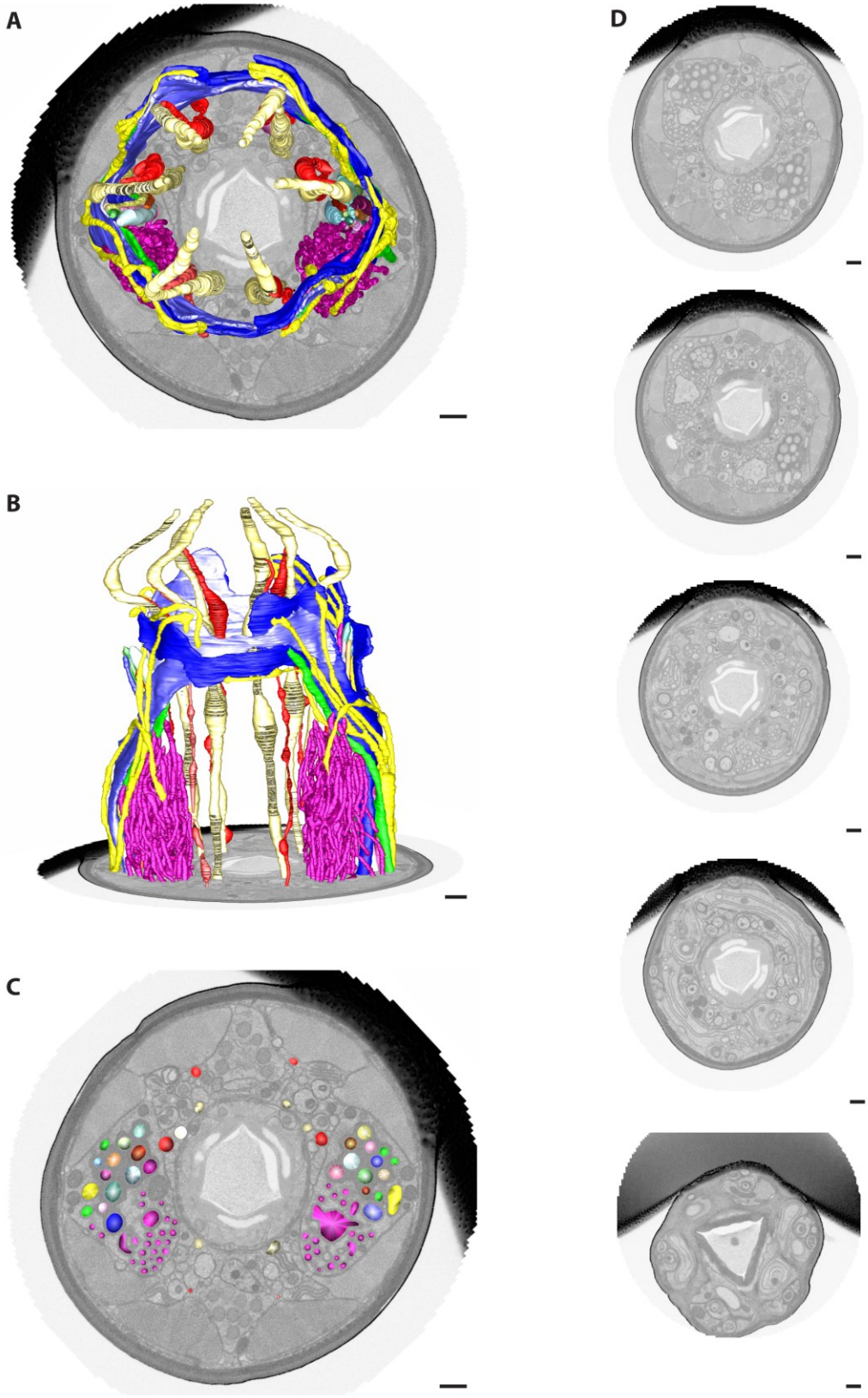

Figure 39: Morphology of the head of *C. elegans* dauer larva. A) Top view of model, B) side view of model. C) Bottom view of model; scale bar 500 nm. D) Image series through the head; scale bar 500 nm. The different colors represent different neurons. Sensory neurons in *C. elegans*: Yellow = AWA, green = AWB, pink = AFD, dark blue = AWCv, light blue = AWCd, red/beige = inner labial neurons.

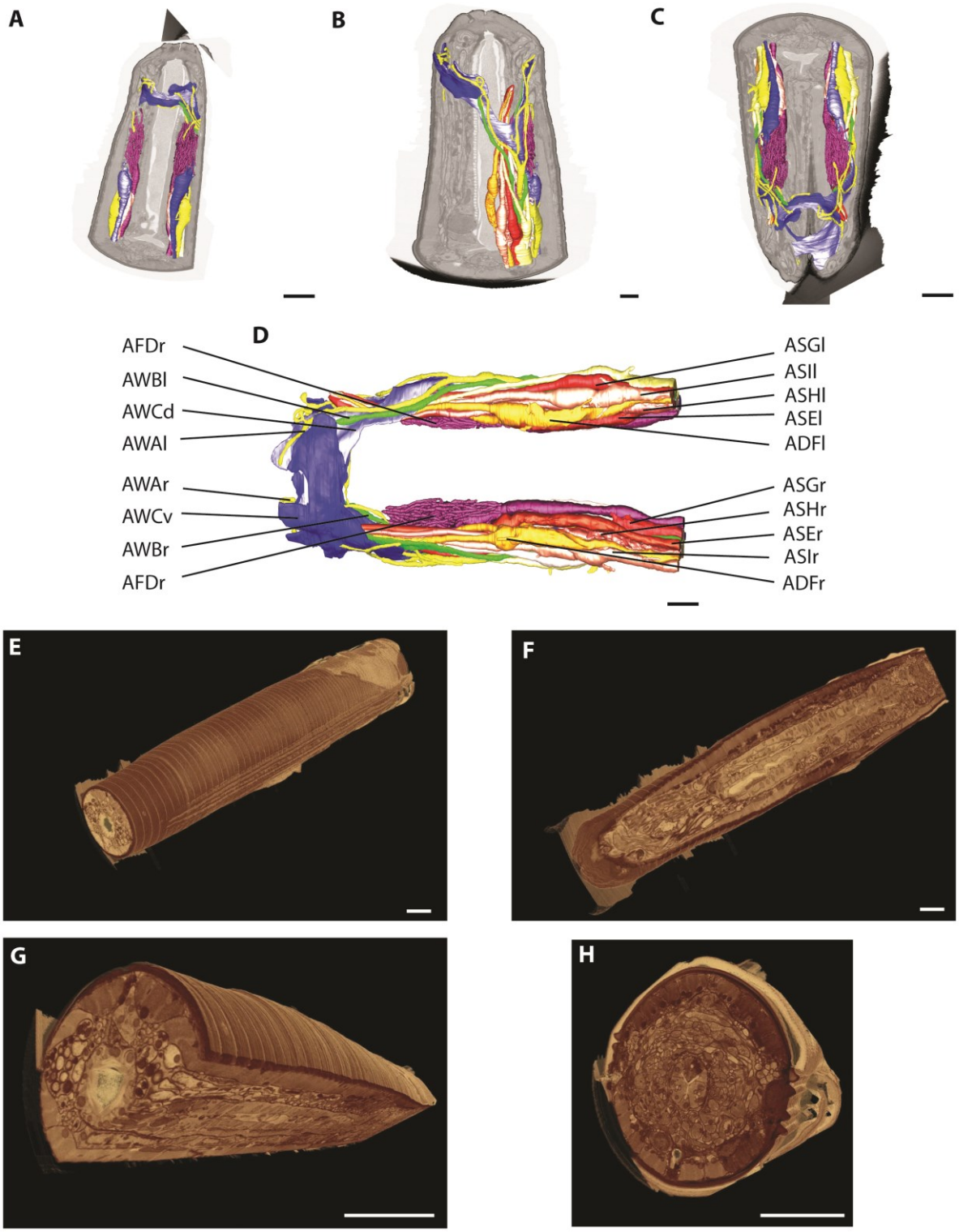

Figure 40: Model of *C. elegans* dauer larva head. A-C) Longitudinal views on segmented *C. elegans* head with EM images in the background (segmentation done by Sarah Tröger, University of Würzburg), acquired at 5 nm x 5 nm x 8 nm voxel size in the FIB-SEM; scale bar 2 µm. D) Longitudinal view on nervous system, naming of the different neurons (r = right, l = left, d = dorsal, v = ventral). E)-H) Images from thresholded dataset corresponding to model A-D), done in ORS (VisualSI) by Robert Kirmse (ZEISS); scale bar 5 µm. Supplementary video #3: **http://tinyurl.com/Steyer-videos**

Although we are not reaching the lateral resolution that can be achieved with TEM, we have the clear advantage of having close to isotropic resolution all the way through our dataset with this method. This allowed our collaborators from the lab of Mei Zhen (Samuel Lunenfeld Research Institute, Department of Molecular Genetics, Department of Physiology, University of Toronto) to connect the gaps they were missing from the serial sections they were working with. It will be interesting, in the future, to compare the findings between the dauer larvae and the L1/L2 and adult worms, to get a better understanding of the morphological changes that are happening, while transitioning between the stages.

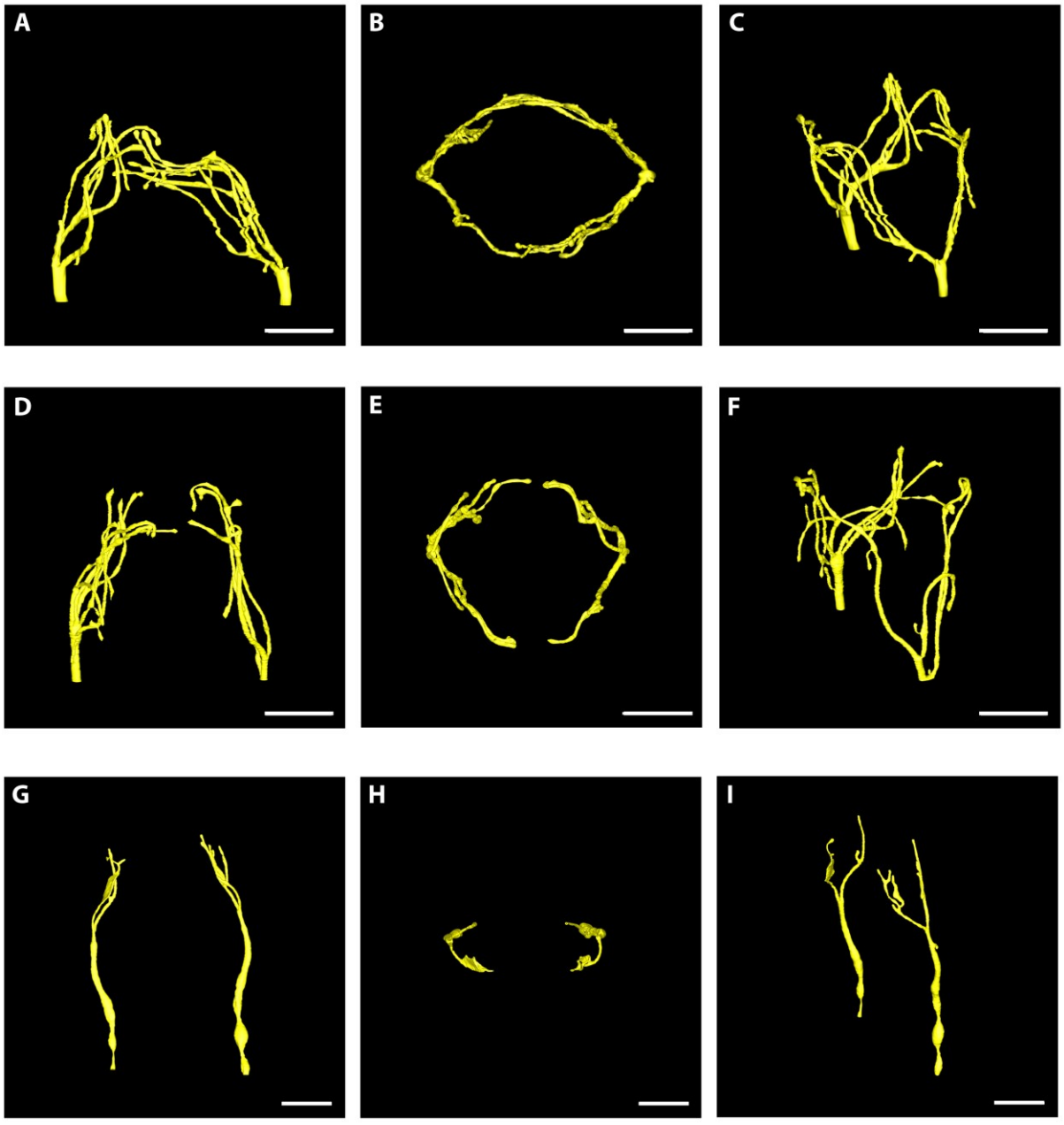

Figure 41: Comparison of AWA neurons in 3 individual *C. elegans* dauer larvae.

Figure 41 (previous page): Three models based on three different *C. elegans* heads, acquired at 5 nm x 5 nm x 8 nm voxel size in the FIB-SEM; scale bar 2 µm. A), D), G) Longitudinal view on AWA neuron. B), E), H) Transversal view from the tip of the worm of AWA. C), F), I) Longitudinal 45° view on AWA neuron.

Two further datasets of the most anterior part of the head of 2 different *C. elegans* dauers were acquired and segmented in addition to the dataset above. The anatomy between individual *C. elegans* worms is known to be very comparable, but here we found a striking inter-animal variation in the morphology of the AWA neuron (olfactory sensory neuron, yellow in Figure 39 and Figure 40). All three individuals have two AWA neurons (dorsal and ventral), but the amount and the length of the bifurcations seemed to be quite different, as well as the distance between the two neurons (Figure 41). This needs to be quantified in more detail. The first worm (Figure 41 A-C) had the most complex system of branches and both neurons got very close. The least furcated AWA neurons were found in the third worm (Figure 41 G-I) which were so far apart that they did not even touch. The second worm had quite a lot of bifurcations and somewhere in the middle between worm 1 and 3 (Figure 41 D-F). Since the dauer larvae have to sense when there is food available again, the sensory neurons would be considered good candidates to look at depending on their state (*e.g.* when the worm has seen some food or the beginning/end of the dauer stage). Since it is difficult to identify how long the worms have progressed within the dauer larva stage, it is not yet clear if the differences originate from different phases of dauer larva stage or if they represent intra-individual diversity. It might also be dependent on what the worms have come into contact with during the dauer stage cycle.

5.3 Methods

5.3.1 Cultivation of *C. elegans*

C. elegans worms were maintained on NGM (Nematode Growth Medium) agar plates containing nystatin. *E. coli* strain OP50 was seeded on the plates as the food source. The worms were transferred to new plates by either picking them individually with a platinum rod or by "chunking", where part of the agar plate is cut out and transferred to a new plate. The plates were stored at 20 °C when performing experiments and kept at 15 °C for later use to slow down the breeding.

5.3.2 Purification of dauer larvae and high-pressure freezing

A week before high-pressure freezing, the *C. elegans* worms were transferred to fresh plates containing *E. coli*, so that the worms reached a critical density that causes a large number of worms to go into dauer stage. The worms were collected either by using some M9 buffer to wash them off the plates or they were picked individually. To separate the dauer larvae from the other worm stages, all worms were treated with SDS, which kills adults and all larvae except the ones in dauer stage. During the dauer stage, the worms don't take up the SDS due to their sealed pharynx and the thick cuticle. The treatment with SDS did not cause any visible damage to the dauer stage larvae and the worms continued moving around as usual. The worms were transferred into 50 ml conical centrifuge tubes by washing them off the plates with M9 medium. They were centrifuged at 2000 g for 5 min at 4 °C, and the supernatant was discarded. The pellet was resuspended in 50 ml of a 1 % SDS solution and the worms were incubated on a shaker for 15 min. Afterwards, the sample was centrifuged at 2000 g for 5 min at 4 °C, and the solution was discarded leaving only about 5 ml. Subsequently, the tube was refilled with ddH_2O and the last step was repeated 3 times. Since dauer larvae show a highly locomotive behavior, separating themselves quite quickly from immobile material, the solution was pipetted on agar plates. Since *C. elegans* worms are not able to move along in liquids, the remaining solution had to dry for the dauer larvae to crawl out of the debris. After 2-3 hours the solution had dried and the majority of the dauer larvae had crawled out of the immobile material and they were washed off the plate with a small volume of M9 buffer. The worms were centrifuged at 2000 g for 5 min at 4 °C and the supernatant was removed. Finally, 1 ml of a 10 % BSA solution was added and after centrifugation again at 2000 g for 5 min at 4 °C and discarding the supernatant, 10 µl of 10 % BSA was added to the worms. The resulting

batch of dauer stage purified worms were then transferred to the 200 µm deep side of a type A carrier (Stigloher, Zhan *et al.*, 2011) and the flat side of a type B carrier was added on top. The worms inside the carrier sandwich were then frozen in either a Leica HPM100 or Leica ICE and kept in liquid nitrogen until they were further processed.

5.3.3 Freeze substitution

For fixation and freeze substitution, a 0.1 % tannic acid and 0.5 % glutaraldehyde solution was prepared in acetone, filled in glass vials and frozen with LN_2. The samples were placed on top of the fixation solution making sure that the carriers were open to allow the chemicals access to the worms. The samples were incubated in the fixation solution for 96 h at -90 °C in an automatic freeze substitution machine (Leica, EM AFS) followed by four washing steps with anhydrous acetone. The samples were then incubated with 2 % osmium tetroxide in anhydrous acetone for 28 h. Next, the temperature was raised over the course of 14 h to -20 °C and kept for 16 h. Finally, the temperature was raised over 4 h to 4 °C and the osmium tetroxide solution was removed by washing four times with anhydrous acetone.

5.3.4 Embedding in Durcupan

The worms were transferred from the carriers into a 50 % Durcupan in acetone solution and incubated for 5 h. In the following steps as much solution as possible was removed from the sample and the Durcupan solutions were added and incubated for 2 hours each. Following incubating the samples with 50 % Durcupan, one substitution with 90 % Durcupan solution and three substitutions with 100 % Durcupan solution were performed. To be able to directly target regions inside the worm, as much resin as possible was removed, ending up with only a very thin layer of resin on top of the sample. The worms were individually picked up with a toothpick and positioned on Aclar. They were gently dragged out of the remaining resin drop until there was no more liquid surrounding them. The worms on top of the Aclar were polymerized in the oven for 96 h at 60 °C. After 4 days, small pieces of Aclar, with the worm on top, were cut out using a razor blade. A conductive carbon sticker (12 mm, Plano GmbH) was placed on SEM stubs (6 mm length, agar scientific) and the Aclar/worm pieces were placed on top. The Aclar piece was surrounded by silver paint (Colloidal Silver Liquid, ted Pella Inc.) and coated with gold for 180 seconds at 30 mA gold in a sputter coater (Quorum, Q150R S) to avoid charging.

5.3.5 FIB-SEM acquisition

FIB-SEM imaging was performed as described in2.3.8.

5.3.6 Post-processing

The acquired images were cropped down to the area of interest and the contrast was inverted. Fiji was used for image processing. First two different smoothing steps ((3 x 3 mean filter) were applied to the raw data and then the image stack was aligned using TrackEM2, a Fiji plugin (Cardona, Saalfeld *et al.*, 2012).

Chapter 6: Conclusion

The collaborations with different research groups at EMBL (Lab Rainer Pepperkok, Lab Jan Ellenberg), other research institutes (Lab Christian Stigloher University Würzburg, Lab Balpreet Singh Ahluwahlia, Tromsø University), as well as companies (Zeiss and Fibics) made it possible to advance in automating CLEM workflows and becoming more precise in targeting regions of interest from 2D cell cultures to 3D multicellular organisms.

In our project, automating phenotypic screens using CLEM, our aim was to automate the complex steps that are required for CLEM data acquisition, making it possible to reach unprecedented throughput in screens performed using EM (chapter 2). This would allow to generate higher amounts of data allowing to draw statistically relevant conclusions. This was achieved by combining multiple siRNA treatments in one dish (solid phase reverse transfection), feedback light microscopy (chapter 2, Tischer, Hilsenstein *et al.*, 2014), automatic navigation inside the FIB-SEM, automatic acquisition and the use of stereological probes, increasing the acquisition and the quantification. The next step will be to run our pipeline on multiple cell unattended and improve our targeting accuracy, which could be done using fiducial markers (*e.g.* beads) visible in LM and EM. Since the SEM stage has a repositioning error of about 1-2 µm, it would be interesting to think about using the electron beam to shift to the correct position instead of moving the stage. Since the coordinate system has quite a big spacing (one labeled square 600 µm) the reference points are quite far away from the region of interest. Decreasing the size of the coordinate system will therefore increase our accuracy in targeting. The screen was developed for adherent cells growing on a coordinate system (chapter 2), but could be extended to samples with a different type of coordinate system with the region of interest close to the surface of the sample (chapter 3 and chapter 4). To be able to be closer to native cell ultrastructure, a future direction would be to apply our automated CLEM workflow to high-pressure frozen samples. Due to the limited diameter of the sample that can be frozen there will be a restriction to how many different treatments can be screened in one sample. The coordinate system needs to be adapted to for example etched sapphire disks. This screen was restricted to siRNAs targeting the Golgi, but the same set-up could be applied to other targets like the mitochondria. There is already a project planned, looking at the changes of the nucleus after siRNA knockdown. As a perspective there would be the potential to administer something else then siRNAs in the individual gelatin spots, for example different drugs, but this will take still a lot more development. A long the lines of EM image analysis,

we will continue exploring different tools that can be used to extract numbers, which on the one hand will be linked to other stereological tools and on the other hand continuing semi-automatic segmentation. Since the stereological analysis right now is done manual, it will be interesting to explore option of automation.

In our projects exploring the potentials of on chip CLEM the first goal was to find a way how to process samples for CLEM being grown on the photonics chips. LSECs were extracted from rats and grown on the chips to look at the endocytic pathway that FSA/phages are taking. The cells were imaged in the evanescent field produced by the waveguides on the chip, and our CLEM approach subsequently allowed for ultrastructural analysis by electron microscopy. To get a better understanding of the structure-function relationship of the LSECs, full isotropic datasets were acquired with 5-10 nm slice thickness, instead of 20-100 nm slice thickness in the stereological approach. One of the most crucial steps was to be able to visualize landmarks in both the LM and the EM to be able to target specific cells. This was accomplished by combining increased temperature and centrifugation to remove as much resin as possible. The next step will be to look at the uptake of phage-like viruses by the LSECs. Here the question would be, if the phages are digested in the lysosomes or if they manage to escape from the endocytic compartments. In future work, automating the acquisition of multiple regions on one chip (similar to chapter 2), would be very interesting. This will enable to do more thorough comparative studies, also looking at changes between healthy and diseased cells on one sample.

In the project of understanding the reformation of the nuclear envelope and the nuclear pores (chapter 4), we took the targeting, volume acquisition and image analysis to the next level. Here we performed a time-resolved CLEM study (30 sec-1 min between acquired time points), uniquely enabling to visualize transient events taking place during anaphase at high-resolution. To quantify our results, we explored different semi-automated and manual segmentation techniques, as well as the use of stereological probes. It will be interesting to quantify the detailed segmentation more closely, looking at the distribution of fenestration size over the time course of anaphase. Another point would be to look at the organization of the ER that is not close to the chromosomes and look at changes throughout the different time points.

For the fast and easy collection of data from a 3D organism, like *C. elegans,* we had to optimize protocols for resin embedding (minimal resin embedding), allowing direct targeting of regions of interest. This was done by dragging the specimen out of the resin, until there was only a thin

layer of resin left over. The large dataset resulted from FIB-SEM imaging of 80 µm along the length of a worm posed new challenges of big data handling, alignment and visualization, which can already be challenging for datasets of individual cells. This was overcome, by using a workstation, a computing cluster, semi-automated alignment tools (TrackEM2) as well as manual alignment. It would be interesting to study the AWA neuron more closely, which seemed to show the most differences compared to the adult dataset. The potential of targeting very precisely specific regions within a multicellular organism, will be great to apply to other larval stages as well as other organisms.

In conclusion, we have successfully set up an automated CLEM workflow, making a screen of heterogeneous phenotypes possible not just on the LM level, but also on the EM level. We have made a lot of progress targeting individual cells in different samples, as well as specific regions in a multicellular organism using minimal resin techniques.

Supplemental Data

Table 7: siRNA for Golgi morphology knockdown

Query	Gene symbol	Ensembl ID	Supplier's siRNA IDs
ENSG00000182326	C1S	ENSG00000182326	s2157
ENSG00000017621	Identifier not found		
ENSG00000116574	RHOU	ENSG00000116574	s33827
ENSG00000183813	CCR4	ENSG00000183813	s3206
ENSG00000117472	TSPAN1	ENSG00000117472	s19658
ENSG00000162129	CLPB	ENSG00000162129	s37653
ENSG00000197520	FAM177B	ENSG00000197520	s53382
ENSG00000006740	ARHGAP44	ENSG00000006740	s19218
ENSG00000180574	Q6KF84_HUMAN	ENSG00000180574	
ENSG00000139182	CLSTN3	ENSG00000139182	s18807
ENSG00000086289	EPDR1	ENSG00000086289	s29377
ENSG00000137145	DENND4C	ENSG00000137145	s31214
ENSG00000101782	RIOK3	ENSG00000101782	s16726
ENSG00000146063	TRIM41	ENSG00000146063	s40532
ENSG00000165655	ZNF503	ENSG00000165655	s39515
ENSG00000007080	CCDC124	ENSG00000007080	s41755
ENSG00000172901	NP_776161.2	ENSG00000172901	s47574
ENSG00000243943	ZNF512	ENSG00000243943	s39029
ENSG00000133704	IPO8	ENSG00000133704	s20635
ENSG00000167701	GPT	ENSG00000167701	s6103
ENSG00000118523	CTGF	ENSG00000118523	s3708
ENSG00000067715	SYT1	ENSG00000067715	s13694
ENSG00000179841	AKAP5	ENSG00000179841	s18200
ENSG00000140464	PML	ENSG00000140464	s10715
ENSG00000129250	KIF1C	ENSG00000129250	s258
ENSG00000198783	ZNF830	ENSG00000198783	s40699
ENSG00000177156	TALDO1	ENSG00000177156	s13776
ENSG00000011304	PTBP1	ENSG00000011304	s11436
ENSG00000011347	SYT7	ENSG00000011347	s17291
ENSG00000132849	INADL	ENSG00000132849	s19903
ENSG00000100485	SOS2	ENSG00000100485	s13289
ENSG00000157927	RADIL	ENSG00000157927	s31280
ENSG00000075945	KIFAP3	ENSG00000075945	s22677
ENSG00000109738	GLRB	ENSG00000109738	s5835
ENSG00000134909	ARHGAP32	ENSG00000134909	s18799
ENSG00000170142	UBE2E1	ENSG00000170142	s561
ENSG00000181085	MAPK15	ENSG00000181085	s48270
ENSG00000176422	SPRYD4	ENSG00000176422	s49210
ENSG00000186350	RXRA	ENSG00000186350	s12384
ENSG00000165322	ARHGAP12	ENSG00000165322	s41278
ENSG00000136108	CKAP2	ENSG00000136108	s25563
ENSG00000001460	C1orf201	ENSG00000001460	s40420
ENSG00000066735	KIF26A	ENSG00000066735	s25178
ENSG00000115368	WDR75	ENSG00000115368	s38530
ENSG00000145107	TM4SF19	ENSG00000145107	s41962
ENSG00000230797	YY2	ENSG00000230797	s53862
ENSG00000144045	DQX1	ENSG00000144045	s46581
ENSG00000136450	SRSF1	ENSG00000136450	s12727
ENSG00000123933	MXD4	ENSG00000123933	s20828
ENSG00000173598	NUDT4	ENSG00000173598	s22020
ENSG00000184432	COPB2	ENSG00000184432	s17738
ENSG00000062194	GPBP1	ENSG00000062194	s35172
ENSG00000169083	AR	ENSG00000169083	s1538
ENSG00000115604	IL18R1	ENSG00000115604	s16795
ENSG00000170921	TANC2	ENSG00000170921	s25113
ENSG00000159167	STC1	ENSG00000159167	s13549
ENSG00000185133	INPP5J	ENSG00000185133	s25858
ENSG00000134569	LRP4	ENSG00000134569	s8287
ENSG00000143994	ABHD1	ENSG00000143994	s39348
ENSG00000157005	SST	ENSG00000157005	s13493
ENSG00000125458	NT5C	ENSG00000125458	s195191
ENSG00000011198	ABHD5	ENSG00000011198	s224185
ENSG00000092445	TYRO3	ENSG00000092445	s14544
ENSG00000185479	KRT6B	ENSG00000185479	s7962
ENSG00000178803	Identifier not found		
ENSG00000115091	ACTR3	ENSG00000115091	s19642
ENSG00000183853	KIRREL	ENSG00000183853	s30530
ENSG00000116786	PLEKHM2	ENSG00000116786	s23280
ENSG00000108848	LUC7L3	ENSG00000108848	s226748
ENSG00000112309	B3GAT2	ENSG00000112309	s43917
ENSG00000133687	TMTC1	ENSG00000133687	s38231
ENSG00000177602	GSG2	ENSG00000177602	s38320
ENSG00000198677	TTC37	ENSG00000198677	s18568
ENSG00000111215	PRR4	ENSG00000111215	s22253
ENSG00000131626	PPFIA1	ENSG00000131626	s506

Table 8: siRNAs selected for further CLEM analysis. The first 10 treatments were acquired with EM. The ones highlighted in red so far only have LM data.

Gene symbol	Description
C1S	complement component 1, s subcomponent
COPB2	coatomer protein complex, subunit beta 2 (beta prime)
COPG1	coatomer protein complex, subunit gamma
DENND4C	DENN/MADD domain containing 4C
DNM1	dynamin 1
GPT	glutamic-pyruvate transaminase (alanine aminotransferase)
IPO8	importin 8
PTBP1	polypyrimidine tract binding protein 1
SRSF1	splicing factor, arginine/serine-rich 1 (splicing factor 2, alternate splicing factor)
WDR75	WD repeat domain 75
ACTR3	ARP3 actin-related protein 3 homolog (yeast)
ARHGAP44	Rho GTPase activating protein 44
FAM177B	family with sequence similarity 177, member B
NT5C	5', 3'-nucleotidase, cytosolic

Appendix

7.1 References

Agnarsson, B., A. B. Jonsdottir, N. B. Arnfinnsdottir and K. Leosson (2011). "On-chip modulation of evanescent illumination and live-cell imaging with polymer waveguides." Opt Express 19(23): 22929-22935.

Alpy, F., A. Rousseau, Y. Schwab, F. Legueux, I. Stoll, C. Wendling, C. Spiegelhalter, P. Kessler, C. Mathelin, M. C. Rio, T. P. Levine and C. Tomasetto (2013). "STARD3 or STARD3NL and VAP form a novel molecular tether between late endosomes and the ER." J Cell Sci 126(Pt 23): 5500-5512.

Anderson, D. J. and M. W. Hetzer (2007). "Nuclear envelope formation by chromatin-mediated reorganization of the endoplasmic reticulum." Nat Cell Biol 9(10): 1160-1166.

Andres, B., U. Koethe, T. Kroeger, M. Helmstaedter, K. L. Briggman, W. Denk and F. A. Hamprecht (2012). "3D segmentation of SBFSEM images of neuropil by a graphical model over supervoxel boundaries." Medical Image Analysis 16(4): 796-805.

Antonin, W., J. Ellenberg and E. Dultz (2008). "Nuclear pore complex assembly through the cell cycle: regulation and membrane organization." FEBS Lett 582(14): 2004-2016.

Armer, H. E., G. Mariggi, K. M. Png, C. Genoud, A. G. Monteith, A. J. Bushby, H. Gerhardt and L. M. Collinson (2009). "Imaging transient blood vessel fusion events in zebrafish by correlative volume electron microscopy." PLoS One 4(11): e7716.

Arnold, J., J. Mahamid, V. Lucic, A. de Marco, J. J. Fernandez, T. Laugks, T. Mayer, A. A. Hyman, W. Baumeister and J. M. Plitzko (2016). "Site-Specific Cryo-focused Ion Beam Sample Preparation Guided by 3D Correlative Microscopy." Biophys J.

Bang, B. H. and F. B. Bang (1957). "Graphic reconstruction of the third dimension from serial electron microphotographs." J Ultrastruct Res 1(2): 138-139.

Bartesaghi, A., A. Merk, S. Banerjee, D. Matthies, X. W. Wu, J. L. S. Milne and S. Subramaniam (2015). "2.2 angstrom resolution cryo-EM structure of beta-galactosidase in complex with a cell-permeant inhibitor." Science 348(6239): 1147-1151.

Bassim, N., K. Scott and L. A. Giannuzzi (2014). "Recent advances in focused ion beam technology and applications." Mrs Bulletin 39(4): 317-325.

Beams, H. W. and R. G. Kessel (1968). "The Golgi apparatus: structure and function." Int Rev Cytol 23: 209-276.

Belevich, I., M. Joensuu, D. Kumar, H. Vihinen and E. Jokitalo (2016). "Microscopy Image Browser: A Platform for Segmentation and Analysis of Multidimensional Datasets." PLoS Biol 14(1): e1002340.

Bennett, A. E., K. Narayan, D. Shi, L. M. Hartnell, K. Gousset, H. He, B. C. Lowekamp, T. S. Yoo, D. Bliss, E. O. Freed and S. Subramaniam (2009). "Ion-abrasion scanning electron

microscopy reveals surface-connected tubular conduits in HIV-infected macrophages." PLoS Pathog 5(9): e1000591.

Betzig, E. (1995). "Proposed method for molecular optical imaging." Opt Lett 20(3): 237-239.

Bhawana, J. L. Miller and A. B. Cahoon (2014). "3D Plant cell architecture of Arabidopsis thaliana (Brassicaceae) using focused ion beam-scanning electron microscopy." Appl Plant Sci 2(6).

Biel, S. S., K. Kawaschinski, K. P. Wittern, U. Hintze and R. Wepf (2003). "From tissue to cellular ultrastructure: closing the gap between micro- and nanostructural imaging." Journal of Microscopy-Oxford 212: 91-99.

Birch-Andersen, A. (1955). "Reconstruction of the nuclear sites of Salmonella typhimurium from electron micrographs of serial sections." J Gen Microbiol 13(2): 327-329.

Bonifacino, J. S. and B. S. Glick (2004). "The mechanisms of vesicle budding and fusion." Cell 116(2): 153-166.

Brenner, S. (1974). "The genetics of Caenorhabditis elegans." Genetics 77(1): 71-94.

Briggman, K. L. and D. D. Bock (2012). "Volume electron microscopy for neuronal circuit reconstruction." Curr Opin Neurobiol 22(1): 154-161.

Bumbarger, D. J., M. Riebesell, C. Rodelsperger and R. J. Sommer (2013). "System-wide rewiring underlies behavioral differences in predatory and bacterial-feeding nematodes." Cell 152(1-2): 109-119.

Burghardt, T., F. Hochapfel, B. Salecker, C. Meese, H. J. Grone, R. Rachel, G. Wanner, M. P. Krahn and R. Witzgall (2015). "Advanced electron microscopic techniques provide a deeper insight into the peculiar features of podocytes." Am J Physiol Renal Physiol 309(12): F1082-1089.

Bykov, Y. S., M. Cortese, J. A. Briggs and R. Bartenschlager (2016). "Correlative light and electron microscopy methods for the study of virus-cell interactions." FEBS Lett 590(13): 1877-1895.

Cantoni, M. and L. Holzer (2014). "Advances in 3D focused ion beam tomography." Mrs Bulletin 39(4): 354-360.

Cardona, A., S. Saalfeld, J. Schindelin, I. Arganda-Carreras, S. Preibisch, M. Longair, P. Tomancak, V. Hartenstein and R. J. Douglas (2012). "TrakEM2 software for neural circuit reconstruction." PLoS One 7(6): e38011.

Carpenter, A. E., T. R. Jones, M. R. Lamprecht, C. Clarke, I. H. Kang, O. Friman, D. A. Guertin, J. H. Chang, R. A. Lindquist, J. Moffat, P. Golland and D. M. Sabatini (2006). "CellProfiler: image analysis software for identifying and quantifying cell phenotypes." Genome Biol 7(10): R100.

Cassada, R. C. and R. L. Russell (1975). "The dauerlarva, a post-embryonic developmental variant of the nematode Caenorhabditis elegans." Dev Biol 46(2): 326-342.

Chatel-Chaix, L., M. Cortese, I. Romero-Brey, S. Bender, C. J. Neufeldt, W. Fischl, P. Scaturro, N. Schieber, Y. Schwab, B. Fischer, A. Ruggieri and R. Bartenschlager (2016). "Dengue Virus Perturbs Mitochondrial Morphodynamics to Dampen Innate Immune Responses." Cell Host Microbe 20(3): 342-356.

Clermont, Y., A. Rambourg and L. Hermo (1995). "Trans-Golgi network (TGN) of different cell types: three-dimensional structural characteristics and variability." Anat Rec 242(3): 289-301.

Cretoiu, D., M. Gherghiceanu, E. Hummel, H. Zimmermann, O. Simionescu and L. M. Popescu (2015). "FIB-SEM tomography of human skin telocytes and their extracellular vesicles." Journal of Cellular and Molecular Medicine 19(4): 714-722.

Dacks, J. B., L. A. Davis, A. M. Sjogren, J. O. Andersson, A. J. Roger and W. F. Doolittle (2003). "Evidence for Golgi bodies in proposed 'Golgi-lacking' lineages." Proc Biol Sci 270 Suppl 2: S168-171.

Dalton, A. J. and M. D. Felix (1954). "Cytologic and cytochemical characteristics of the Golgi substance of epithelial cells of the epididymis in situ, in homogenates and after isolation." Am J Anat 94(2): 171-207.

de Boer, P., J. P. Hoogenboom and B. N. Giepmans (2015). "Correlated light and electron microscopy: ultrastructure lights up!" Nat Methods 12(6): 503-513.

De Leeuw, A. M., A. Brouwer and D. L. Knook (1990). "Sinusoidal endothelial cells of the liver: fine structure and function in relation to age." J Electron Microsc Tech 14(3): 218-236.

De Matteis, M. A. and A. Luini (2008). "Exiting the Golgi complex." Nat Rev Mol Cell Biol 9(4): 273-284.

Denk, W. and H. Horstmann (2004). "Serial block-face scanning electron microscopy to reconstruct three-dimensional tissue nanostructure." PLoS Biol 2(11): e329.

Doroquez, D. B., C. Berciu, J. R. Anderson, P. Sengupta and D. Nicastro (2014). "A high-resolution morphological and ultrastructural map of anterior sensory cilia and glia in Caenorhabditis elegans." Elife 3: e01948.

Drobne, D., M. Milani, A. Zrimec, V. Leser and M. Berden Zrimec (2005). "Electron and ion imaging of gland cells using the FIB/SEM system." J Microsc 219(Pt 1): 29-35.

Drobne, D., M. Milani, A. Zrimec, M. B. Zrimec, F. Tatti and K. Draslar (2005). "Focused ion beam/scanning electron microscopy studies of Porcellio scaber (Isopoda, Crustacea) digestive gland epithelium cells." Scanning 27(1): 30-34.

Durdu, S., M. Iskar, C. Revenu, N. Schieber, A. Kunze, P. Bork, Y. Schwab and D. Gilmour (2014). "Luminal signalling links cell communication to tissue architecture during organogenesis." Nature 515(7525): 120-124.

Dylewski, D. P., R. M. Haralick and T. W. Keenan (1984). "Three-dimensional ultrastructure of the Golgi apparatus in bovine mammary epithelial cells during lactation." J Ultrastruct Res 87(1): 75-85.

Earl, L. A., J. D. Lifson and S. Subramaniam (2013). "Catching HIV 'in the act' with 3D electron microscopy." Trends Microbiol 21(8): 397-404.

Erfle, H., B. Neumann, U. Liebel, P. Rogers, M. Held, T. Walter, J. Ellenberg and R. Pepperkok (2007). "Reverse transfection on cell arrays for high content screening microscopy." Nat Protoc 2(2): 392-399.

Farquhar, M. G. and G. E. Palade (1981). "The Golgi apparatus (complex)-(1954-1981)-from artifact to center stage." J Cell Biol 91(3 Pt 2): 77s-103s.

Farquhar, M. G. and J. F. Rinehart (1954). "Cytologic alterations in the anterior pituitary gland following thyroidectomy: an electron microscope study." Endocrinology 65(6): 857-876.

Fehrenbach, J., P. Weiss and C. Lorenzo (2012). "Variational algorithms to remove stationary noise: applications to microscopy imaging." IEEE Trans Image Process 21(10): 4420-4430.

Ferguson, S., A. M. Steyer, M. T.M., Y. Schwab and J. M. Lucocq (in preparation). "A stereological toolkit for fast and efficient 3D quantification of Golgi populations in section-based EM." Traffic.

Fernandez-Leiro, R. and S. H. Scheres (2016). "Unravelling biological macromolecules with cryo-electron microscopy." Nature 537(7620): 339-346.

Furuta, K. M., S. R. Yadav, S. Lehesranta, I. Belevich, S. Miyashima, J. O. Heo, A. Vaten, O. Lindgren, B. De Rybel, G. Van Isterdael, P. Somervuo, R. Lichtenberger, R. Rocha, S. Thitamadee, S. Tahtiharju, P. Auvinen, T. Beeckman, E. Jokitalo and Y. Helariutta (2014). "Plant development. Arabidopsis NAC45/86 direct sieve element morphogenesis culminating in enucleation." Science 345(6199): 933-937.

Gilbert, P. F. (1972). "The reconstruction of a three-dimensional structure from projections and its application to electron microscopy. II. Direct methods." Proc R Soc Lond B Biol Sci 182(1066): 89-102.

Glick, B. S. (2000). "Organization of the Golgi apparatus." Curr Opin Cell Biol 12(4): 450-456.

Glick, B. S. and A. Luini (2011). "Models for Golgi traffic: a critical assessment." Cold Spring Harb Perspect Biol 3(11): a005215.

Godman, G. C., C. Morgan, P. M. Breitenfeld and H. M. Rose (1960). "A correlative study by electron and light microscopy of the development of type 5 adenovirus. II. Light microscopy." J Exp Med 112: 383-402.

Goetz, J. G., E. Steed, R. R. Ferreira, S. Roth, C. Ramspacher, F. Boselli, G. Charvin, M. Liebling, C. Wyart, Y. Schwab and J. Vermot (2014). "Endothelial cilia mediate low flow sensing during zebrafish vascular development." Cell Rep 6(5): 799-808.

Golden, J. W. and D. L. Riddle (1982). "A Pheromone Influences Larval Development in the Nematode Caenorhabditis-Elegans." Science 218(4572): 578-580.

Goud, B. and P. A. Gleeson (2010). "TGN golgins, Rabs and cytoskeleton: regulating the Golgi trafficking highways." Trends Cell Biol 20(6): 329-336.

Grabenbauer, M., W. J. Geerts, J. Fernadez-Rodriguez, A. Hoenger, A. J. Koster and T. Nilsson (2005). "Correlative microscopy and electron tomography of GFP through photooxidation." Nat Methods 2(11): 857-862.

Griffiths, G. (2000). "Gut thoughts on the Golgi complex." Traffic 1(9): 738-745.

Griffiths, G., R. Pepperkok, J. K. Locker and T. E. Kreis (1995). "Immunocytochemical localization of beta-COP to the ER-Golgi boundary and the TGN." J Cell Sci 108 (Pt 8): 2839-2856.

Griffiths, G., S. Pfeiffer, K. Simons and K. Matlin (1985). "Exit of newly synthesized membrane proteins from the trans cisterna of the Golgi complex to the plasma membrane." J Cell Biol 101(3): 949-964.

Griffiths, G., P. Quinn and G. Warren (1983). "Dissection of the Golgi complex. I. Monensin inhibits the transport of viral membrane proteins from medial to trans Golgi cisternae in baby hamster kidney cells infected with Semliki Forest virus." J Cell Biol 96(3): 835-850.

Griffiths, G. and K. Simons (1986). "The Trans Golgi Network - Sorting at the Exit Site of the Golgi-Complex." Science 234(4775): 438-443.

Gundersen, H. J. (1986). "Stereology of arbitrary particles. A review of unbiased number and size estimators and the presentation of some new ones, in memory of William R. Thompson." J Microsc 143(Pt 1): 3-45.

Gundersen, H. J., E. B. Jensen, K. Kieu and J. Nielsen (1999). "The efficiency of systematic sampling in stereology--reconsidered." J Microsc 193(Pt 3): 199-211.

Hall, D. H. and R. L. Russell (1991). "The posterior nervous system of the nematode Caenorhabditis elegans: serial reconstruction of identified neurons and complete pattern of synaptic interactions." J Neurosci 11(1): 1-22.

Hampoelz, B., M. T. Mackmull, P. Machado, P. Ronchi, K. H. Bui, N. Schieber, R. Santarella-Mellwig, A. Necakov, A. Andres-Pons, J. M. Philippe, T. Lecuit, Y. Schwab and M. Beck (2016). "Pre-assembled Nuclear Pores Insert into the Nuclear Envelope during Early Development." Cell 166(3): 664-678.

Hanson, H. H., J. E. Reilly, R. Lee, W. G. Janssen and G. R. Phillips (2010). "Streamlined embedding of cell monolayers on gridded glass-bottom imaging dishes for correlative light and electron microscopy." Microsc Microanal 16(6): 747-754.

Hayworth, K. J., C. S. Xu, Z. Lu, G. W. Knott, R. D. Fetter, J. C. Tapia, J. W. Lichtman and H. F. Hess (2015). "Ultrastructurally smooth thick partitioning and volume stitching for large-scale connectomics." Nat Methods 12(4): 319-322.

Hayworth, K. J. K., N.; Schalek, R.; Lichtmann, J.W. (2006). "Automating the Collection of Ultrathin Serial Sections for Large Volume TEM Reconstructions." Microsc Microanal 12: 86.

Hell, S. W. and J. Wichmann (1994). "Breaking the diffraction resolution limit by stimulated emission: stimulated-emission-depletion fluorescence microscopy." Opt Lett 19(11): 780-782.

Helle, Ø. I. Ø., C.I. ; McCourt, P. ; Ahluwalia, B.S.; (2015). "Chip-based optical microscopy for imaging membrane sieve plates of liver scavenger cells." Proc. of Spie 9554(Nanoimaging and Nanospectroscopy III).

Heymann, J. A., M. Hayles, I. Gestmann, L. A. Giannuzzi, B. Lich and S. Subramaniam (2006). "Site-specific 3D imaging of cells and tissues with a dual beam microscope." J Struct Biol 155(1): 63-73.

Hoang, T. V., C. Kizilyaprak, D. Spehner, B. M. Humbel and P. Schultz (2016). "Automatic segmentation of high pressure frozen and freeze-substituted mouse retina nuclei from FIB-SEM tomograms." J Struct Biol.

Hoelz, A., J. S. Glavy and M. Beck (2016). "Toward the atomic structure of the nuclear pore complex: when top down meets bottom up." Nat Struct Mol Biol 23(7): 624-630.

Hoenger, A. (2014). "High-resolution cryo-electron microscopy on macromolecular complexes and cell organelles." Protoplasma 251(2): 417-427.

Ichimura, K., S. Kakuta, Y. Kawasaki, T. Miyaki, T. Nonami, N. Miyazaki, T. Nakao, S. Enomoto, S. Arai, M. Koike, K. Murata and T. Sakai (2017). "Morphological process of podocyte development revealed by block-face scanning electron microscopy." J Cell Sci 130(1): 132-142.

Jimenez, N., E. G. Van Donselaar, D. A. De Winter, K. Vocking, A. J. Verkleij and J. A. Post (2010). "Gridded Aclar: preparation methods and use for correlative light and electron microscopy of cell monolayers, by TEM and FIB-SEM." J Microsc 237(2): 208-220.

Joensuu, M., I. Belevich, O. Ramo, I. Nevzorov, H. Vihinen, M. Puhka, T. M. Witkos, M. Lowe, M. K. Vartiainen and E. Jokitalo (2014). "ER sheet persistence is coupled to myosin 1c-regulated dynamic actin filament arrays." Molecular Biology of the Cell 25(7): 1111-1126.

Joesch, M., D. Mankus, M. Yamagata, A. Shahbazi, R. Schalek, A. Suissa-Peleg, M. Meister, J. W. Lichtman, W. J. Scheirer and J. R. Sanes (2016). "Reconstruction of genetically identified neurons imaged by serial-section electron microscopy." Elife 5.

Kaplan, F., J. Srinivasan, P. Mahanti, R. Ajredini, O. Durak, R. Nimalendran, P. W. Sternberg, P. E. Teal, F. C. Schroeder, A. S. Edison and H. T. Alborn (2011). "Ascaroside expression in Caenorhabditis elegans is strongly dependent on diet and developmental stage." PLoS One 6(3): e17804.

Karreman, M. A., A. V. Agronskaia, E. G. van Donselaar, K. Vocking, F. Fereidouni, B. M. Humbel, C. T. Verrips, A. J. Verkleij and H. C. Gerritsen (2012). "Optimizing immuno-labeling for correlative fluorescence and electron microscopy on a single specimen." J Struct Biol 180(2): 382-386.

Karreman, M. A., L. Mercier, N. L. Schieber, G. Solecki, G. Allio, F. Winkler, B. Ruthensteiner, J. G. Goetz and Y. Schwab (2016). "Fast and precise targeting of single tumor cells in vivo by multimodal correlative microscopy." J Cell Sci 129(2): 444-456.

Kasthuri, N., K. J. Hayworth, D. R. Berger, R. L. Schalek, J. A. Conchello, S. Knowles-Barley, D. Lee, A. Vazquez-Reina, V. Kaynig, T. R. Jones, M. Roberts, J. L. Morgan, J. C. Tapia, H. S. Seung, W. G. Roncal, J. T. Vogelstein, R. Burns, D. L. Sussman, C. E. Priebe, H. Pfister and

J. W. Lichtman (2015). "Saturated Reconstruction of a Volume of Neocortex." Cell 162(3): 648-661.

Kizilyaprak, C., A. G. Bittermann, J. Daraspe and B. M. Humbel (2014). "FIB-SEM tomography in biology." Methods Mol Biol 1117: 541-558.

Klumperman, J. (2000). "Transport between ER and Golgi." Curr Opin Cell Biol 12(4): 445-449.

Klumperman, J. (2011). "Architecture of the Mammalian Golgi." Cold Spring Harbor Perspectives in Biology 3(7).

Knott, G., H. Marchman, D. Wall and B. Lich (2008). "Serial section scanning electron microscopy of adult brain tissue using focused ion beam milling." J Neurosci 28(12): 2959-2964.

Kolotuev, I., Y. Schwab and M. Labouesse (2010). "A precise and rapid mapping protocol for correlative light and electron microscopy of small invertebrate organisms." Biol Cell 102(2): 121-132.

Kondylis, V. and C. Rabouille (2009). "The Golgi apparatus: lessons from Drosophila." FEBS Lett 583(23): 3827-3838.

Kosinski, J., S. Mosalaganti, A. von Appen, R. Teimer, A. L. DiGuilio, W. Wan, K. H. Bui, W. J. Hagen, J. A. Briggs, J. S. Glavy, E. Hurt and M. Beck (2016). "Molecular architecture of the inner ring scaffold of the human nuclear pore complex." Science 352(6283): 363-365.

Kremer, A., S. Lippens, S. Bartunkova, B. Asselbergh, C. Blanpain, M. Fendrych, A. Goossens, M. Holt, S. Janssens, M. Krols, J. C. Larsimont, C. Mc Guire, M. K. Nowack, X. Saelens, A. Schertel, B. Schepens, M. Slezak, V. Timmerman, C. Theunis, V. A. N. B. R, Y. Visser and C. J. Guerin (2015). "Developing 3D SEM in a broad biological context." J Microsc.

Kremer, J. R., D. N. Mastronarde and J. R. McIntosh (1996). "Computer visualization of three-dimensional image data using IMOD." J Struct Biol 116(1): 71-76.

Kreshuk, A., U. Koethe, E. Pax, D. D. Bock and F. A. Hamprecht (2014). "Automated detection of synapses in serial section transmission electron microscopy image stacks." PLoS One 9(2): e87351.

Krohn, V. E. (1961). "Liquid metal droplets for heavy particle propulsion." Progress in Astronautics and Rocketry 5: 73-80.

Krohn, V. E. and G. R. Ringo (1975). "Ion source of high brightness using liquid metal." Appl. Phys. Lett. 27: 479-481.

Kukulski, W., M. Schorb, M. Kaksonen and J. A. G. Briggs (2012). "Plasma Membrane Reshaping during Endocytosis Is Revealed by Time-Resolved Electron Tomography." Cell 150(3): 508-520.

Kukulski, W., M. Schorb, S. Welsch, A. Picco, M. Kaksonen and J. A. Briggs (2011). "Correlated fluorescence and 3D electron microscopy with high sensitivity and spatial precision." J Cell Biol 192(1): 111-119.

Lee, T. H. and A. D. Linstedt (1999). "Osmotically induced cell volume changes alter anterograde and retrograde transport, Golgi structure, and COPI dissociation." Mol Biol Cell 10(5): 1445-1462.

Leighton, S. B. (1981). "SEM images of block faces, cut by a miniature microtome within the SEM - a technical note." Scan Electron Microsc(Pt 2): 73-76.

Lindsey, J. D. and M. H. Ellisman (1985). "The Neuronal Endomembrane System .2. The Multiple Forms of the Golgi-Apparatus Cis Element." Journal of Neuroscience 5(12): 3124-3134.

Lu, L., M. S. Ladinsky and T. Kirchhausen (2009). "Cisternal organization of the endoplasmic reticulum during mitosis." Mol Biol Cell 20(15): 3471-3480.

Lu, L., M. S. Ladinsky and T. Kirchhausen (2011). "Formation of the postmitotic nuclear envelope from extended ER cisternae precedes nuclear pore assembly." J Cell Biol 194(3): 425-440.

Lucic, V., A. H. Kossel, T. Yang, T. Bonhoeffer, W. Baumeister and A. Sartori (2007). "Multiscale imaging of neurons grown in culture: from light microscopy to cryo-electron tomography." J Struct Biol 160(2): 146-156.

Lucocq, J. (1993). "Unbiased 3-D quantitation of ultrastructure in cell biology." Trends Cell Biol 3(10): 354-358.

Lucocq, J. (2008). "Quantification of structures and gold labeling in transmission electron microscopy." Methods Cell Biol 88: 59-82.

Lucocq, J., E. Berger and C. Hug (1995). "The pathway of Golgi cluster formation in okadaic acid-treated cells." Journal of Structural Biology 115(3): 318-330.

Lucocq, J. M. and C. Hacker (2013). "Cutting a fine figure: On the use of thin sections in electron microscopy to quantify autophagy." Autophagy 9(9): 1443-1448.

Lucocq, J. M., T. M. Mayhew, Y. Schwab, A. M. Steyer and C. Hacker (2015). "Systems biology in 3D space--enter the morphome." Trends Cell Biol 25(2): 59-64.

Maco, B., A. Holtmaat, M. Cantoni, A. Kreshuk, C. N. Straehle, F. A. Hamprecht and G. W. Knott (2013). "Correlative in vivo 2 photon and focused ion beam scanning electron microscopy of cortical neurons." PLoS One 8(2): e57405.

Majaneva, M., I. Remonen, J. M. Rintala, I. Belevich, A. Kremp, O. Setala, E. Jokitalo and J. Blomster (2014). "Rhinomonas nottbecki n. sp. (cryptomonadales) and molecular phylogeny of the family Pyrenomonadaceae." J Eukaryot Microbiol 61(5): 480-492.

Markert, S. M., S. Britz, S. Proppert, M. Lang, D. Witvliet, B. Mulcahy, M. Sauer, M. Zhen, J. L. Bessereau and C. Stigloher (2016). "Filling the gap: adding super-resolution to array tomography for correlated ultrastructural and molecular identification of electrical synapses at the C. elegans connectome." Neurophotonics 3(4): 041802.

Marsh, B. J. (2005). "Lessons from tomographic studies of the mammalian Golgi." Biochim Biophys Acta 1744(3): 273-292.

Marsh, B. J., D. N. Mastronarde, K. F. Buttle, K. E. Howell and J. R. McIntosh (2001). "Organellar relationships in the Golgi region of the pancreatic beta cell line, HIT-T15, visualized by high resolution electron tomography." Proc Natl Acad Sci U S A 98(5): 2399-2406.

Mastronarde, D. N. (1997). "Dual-axis tomography: an approach with alignment methods that preserve resolution." J Struct Biol 120(3): 343-352.

Mayhew, T. M. and H. J. G. Gundersen (1996). "'If you assume, you can make an ass out of u and me': A decade of the disector for stereological counting of particles in 3D space." Journal of Anatomy 188: 1-15.

Mellman, I. and K. Simons (1992). "The Golgi complex: in vitro veritas?" Cell 68(5): 829-840.

Mikula, S. and W. Denk (2015). "High-resolution whole-brain staining for electron microscopic circuit reconstruction." Nat Methods 12(6): 541-546.

Milrot, E., Y. Mutsafi, Y. Fridmann-Sirkis, E. Shimoni, K. Rechav, J. R. Gurnon, J. L. Van Etten and A. Minsky (2016). "Virus-host interactions: insights from the replication cycle of the large Paramecium bursaria chlorella virus." Cell Microbiol 18(1): 3-16.

Mironov, A. A., R. S. Polishchuk and G. V. Beznoussenko (2008). "Combined video fluorescence and 3D electron microscopy." Methods Cell Biol 88: 83-95.

Moerner, W. E. and L. Kador (1989). "Optical detection and spectroscopy of single molecules in a solid." Phys Rev Lett 62(21): 2535-2538.

Narayan, K., C. M. Danielson, K. Lagarec, B. C. Lowekamp, P. Coffman, A. Laquerre, M. W. Phaneuf, T. J. Hope and S. Subramaniam (2014). "Multi-resolution correlative focused ion beam scanning electron microscopy: applications to cell biology." J Struct Biol 185(3): 278-284.

Narayan, K. and S. Subramaniam (2015). "Focused ion beams in biology." Nature Methods 12(11): 1022-1031.

Nelson, F. K., P. S. Albert and D. L. Riddle (1983). "Fine structure of the Caenorhabditis elegans secretory-excretory system." J Ultrastruct Res 82(2): 156-171.

Nixon, S. J., R. I. Webb, M. Floetenmeyer, N. Schieber, H. P. Lo and R. G. Parton (2009). "A Single Method for Cryofixation and Correlative Light, Electron Microscopy and Tomography of Zebrafish Embryos." Traffic 10(2): 131-136.

Noske, A. B., A. J. Costin, G. P. Morgan and B. J. Marsh (2008). "Expedited approaches to whole cell electron tomography and organelle mark-up in situ in high-pressure frozen pancreatic islets." J Struct Biol 161(3): 298-313.

Orloff, J., M. Utlaut and L. Swanson (1993). "High-resolution focused ion beams." AIP Review of Scientific Instruments 64.

Otsuka, S., K. H. Bui, M. Schorb, M. J. Hossain, A. Z. Politi, B. Koch, M. Eltsov, M. Beck and J. Ellenberg (2016). "Nuclear pore assembly proceeds by an inside-out extrusion of the nuclear envelope." Elife 5.

Peddie, C. J. and L. M. Collinson (2014). "Exploring the third dimension: volume electron microscopy comes of age." Micron 61: 9-19.

Pelletier, L., C. A. Stern, M. Pypaert, D. Sheff, H. M. Ngo, N. Roper, C. Y. He, K. Hu, D. Toomre, I. Coppens, D. S. Roos, K. A. Joiner and G. Warren (2002). "Golgi biogenesis in Toxoplasma gondii." Nature 418(6897): 548-552.

Penczek, P., M. Marko, K. Buttle and J. Frank (1995). "Double-tilt electron tomography." Ultramicroscopy 60(3): 393-410.

Plaza, S. M., L. K. Scheffer and M. Saunders (2012). "Minimizing manual image segmentation turn-around time for neuronal reconstruction by embracing uncertainty." PLoS One 7(9): e44448.

Po, M. D., C. Hwang and M. Zhen (2010). "PHRs: bridging axon guidance, outgrowth and synapse development." Curr Opin Neurobiol 20(1): 100-107.

Porter, K. R., A. Claude and E. F. Fullam (1945). "A Study of Tissue Culture Cells by Electron Microscopy : Methods and Preliminary Observations." J Exp Med 81(3): 233-246.

Quinn, P., G. Griffiths and G. Warren (1983). "Dissection of the Golgi complex. II. Density separation of specific Golgi functions in virally infected cells treated with monensin." J Cell Biol 96(3): 851-856.

R Development Core Team (2008). "A language and environment for statistical computing." R Foundation for Statistical Computing.

Rabouille, C. and J. Klumperman (2005). "Opinion: The maturing role of COPI vesicles in intra-Golgi transport." Nat Rev Mol Cell Biol 6(10): 812-817.

Rabouille, C., T. Misteli, R. Watson and G. Warren (1995). "Reassembly of Golgi stacks from mitotic Golgi fragments in a cell-free system." J Cell Biol 129(3): 605-618.

Rabut, G., P. Lenart and J. Ellenberg (2004). "Dynamics of nuclear pore complex organization through the cell cycle." Curr Opin Cell Biol 16(3): 314-321.

Rambourg, A., Y. Clermont and A. Marraud (1974). "Three-dimensional structure of the osmium-impregnated Golgi apparatus as seen in the high voltage electron microscope." Am J Anat 140(1): 27-45.

Rambourg, A. C. Y. (1997). "Three-dimensional structure of the Golgi apparatus in mammalian cells." The Golgi Apparatus: 37-61.

Redemann, S. and T. Muller-Reichert (2013). "Correlative light and electron microscopy for the analysis of cell division." J Microsc 251(2): 109-112.

Romero-Brey, I. and R. Bartenschlager (2015). "Viral Infection at High Magnification: 3D Electron Microscopy Methods to Analyze the Architecture of Infected Cells." Viruses 7(12): 6316-6345.

Russell, M. R., T. R. Lerner, J. J. Burden, D. O. Nkwe, A. Pelchen-Matthews, M. C. Domart, J. Durgan, A. Weston, M. L. Jones, C. J. Peddie, R. Carzaniga, O. Florey, M. Marsh, M. G.

Gutierrez and L. M. Collinson (2016). "3D correlative light and electron microscopy of cultured cells using serial blockface scanning electron microscopy." J Cell Sci.

Sartori, A., R. Gatz, F. Beck, A. Rigort, W. Baumeister and J. M. Plitzko (2007). "Correlative microscopy: bridging the gap between fluorescence light microscopy and cryo-electron tomography." J Struct Biol 160(2): 135-145.

Schalek, R. H., K.; Kasthuri, N.; Morgan, J.L.; Berger, D.; Wilson, A.M.; Anger,P. (2012). "ATUM-based SEM for High-Speed Large-Volume Biological Reconstructions." Microsc. Microanal. 18.

Schalek, R. K., N.; Hayworth, K.; Berger, D.; Tapia, J.C.; Morgan, J.L.; Turaga S.C.; Fagerholm, E.; Seung, H.S.; Lichtmann, J.W. (2011). "Development of High-Throughput, High-Resolution 3D Reconstruction of Large-Volume Biological Tissue Using Automated Tape Collection Ultramicrotomy and Scanning Electron Microscopy." Microsc. Microanal. 17.

Schertel, A., N. Snaidero, H. M. Han, T. Ruhwedel, M. Laue, M. Grabenbauer and W. Mobius (2013). "Cryo FIB-SEM: volume imaging of cellular ultrastructure in native frozen specimens." J Struct Biol 184(2): 355-360.

Schindelin, J., I. Arganda-Carreras, E. Frise, V. Kaynig, M. Longair, T. Pietzsch, S. Preibisch, C. Rueden, S. Saalfeld, B. Schmid, J. Y. Tinevez, D. J. White, V. Hartenstein, K. Eliceiri, P. Tomancak and A. Cardona (2012). "Fiji: an open-source platform for biological-image analysis." Nat Methods 9(7): 676-682.

Schur, F. K., W. J. Hagen, M. Rumlova, T. Ruml, B. Muller, H. G. Krausslich and J. A. Briggs (2015). "Structure of the immature HIV-1 capsid in intact virus particles at 8.8 A resolution." Nature 517(7535): 505-508.

Schwarz, H. and B. M. Humbel (2007). "Correlative light and electron microscopy using immunolabeled resin sections." Methods Mol Biol 369: 229-256.

Shen, H., E. Huang, T. Das, H. Xu, M. Ellisman and Z. Liu (2014). "TIRF microscopy with ultra-short penetration depth." Opt Express 22(9): 10728-10734.

Simpson, J. C., B. Joggerst, V. Laketa, F. Verissimo, C. Cetin, H. Erfle, M. G. Bexiga, V. R. Singan, J. K. Heriche, B. Neumann, A. Mateos, J. Blake, S. Bechtel, V. Benes, S. Wiemann, J. Ellenberg and R. Pepperkok (2012). "Genome-wide RNAi screening identifies human proteins with a regulatory function in the early secretory pathway." Nat Cell Biol 14(7): 764-774.

Smedsrod, B., P. J. De Bleser, F. Braet, P. Lovisetti, K. Vanderkerken, E. Wisse and A. Geerts (1994). "Cell biology of liver endothelial and Kupffer cells." Gut 35(11): 1509-1516.

Smedsrod, B. and H. Pertoft (1985). "Preparation of pure hepatocytes and reticuloendothelial cells in high yield from a single rat liver by means of Percoll centrifugation and selective adherence." J Leukoc Biol 38(2): 213-230.

Sommer, C., C. Straehle, U. Koethe and F. A. Hamprecht (2011). "ilastik: interactive learning and segmentation toolkit." iEEE International Symposium on Biomedical Imaging (ISBI): 230-233.

Spiegelhalter, C., J. F. Laporte and Y. Schwab (2014). "Correlative light and electron microscopy: from live cell dynamic to 3D ultrastructure." Methods Mol Biol 1117: 485-501.

Spiegelhalter, C., V. Tosch, D. Hentsch, M. Koch, P. Kessler, Y. Schwab and J. Laporte (2010). "From dynamic live cell imaging to 3D ultrastructure: novel integrated methods for high pressure freezing and correlative light-electron microscopy." PLoS One 5(2): e9014.

Spurr, A. R. (1969). "A low-viscosity epoxy resin embedding medium for electron microscopy." J Ultrastruct Res 26(1): 31-43.

Steinbrecht, R. A. and M. Müller (1987). "Freeze-substitution and freeze-drying. In "Cryotechniques in Biological Electron Microscopy"." Springer Berlin, Heidelberg: 149-172.

Stigloher, C., H. Zhan, M. Zhen, J. Richmond and J. L. Bessereau (2011). "The presynaptic dense projection of the Caenorhabditis elegans cholinergic neuromuscular junction localizes synaptic vesicles at the active zone through SYD-2/liprin and UNC-10/RIM-dependent interactions." J Neurosci 31(12): 4388-4396.

Storrie, B., J. White, S. Rottger, E. H. Stelzer, T. Suganuma and T. Nilsson (1998). "Recycling of golgi-resident glycosyltransferases through the ER reveals a novel pathway and provides an explanation for nocodazole-induced Golgi scattering." J Cell Biol 143(6): 1505-1521.

Thyberg, J. and S. Moskalewski (1985). "Microtubules and the organization of the Golgi complex." Exp Cell Res 159(1): 1-16.

Tischer, C., V. Hilsenstein, K. Hanson and R. Pepperkok (2014). "Adaptive fluorescence microscopy by online feedback image analysis." Methods Cell Biol 123: 489-503.

Titze, B. and C. Genoud (2016). "Volume scanning electron microscopy for imaging biological ultrastructure." Biol Cell.

Trucco, A., R. S. Polishchuk, O. Martella, A. Di Pentima, A. Fusella, D. Di Giandomenico, E. San Pietro, G. V. Beznoussenko, E. V. Polishchuk, M. Baldassarre, R. Buccione, W. J. Geerts, A. J. Koster, K. N. Burger, A. A. Mironov and A. Luini (2004). "Secretory traffic triggers the formation of tubular continuities across Golgi sub-compartments." Nat Cell Biol 6(11): 1071-1081.

van Rijnsoever, C., V. Oorschot and J. Klumperman (2008). "Correlative light-electron microscopy (CLEM) combining live-cell imaging and immunolabeling of ultrathin cryosections." Nat Methods 5(11): 973-980.

Villinger, C., H. Gregorius, C. Kranz, K. Hohn, C. Munzberg, G. von Wichert, B. Mizaikoff, G. Wanner and P. Walther (2012). "FIB/SEM tomography with TEM-like resolution for 3D imaging of high-pressure frozen cells." Histochem Cell Biol 138(4): 549-556.

Villinger, C., G. Neusser, C. Kranz, P. Walther and T. Mertens (2015). "3D Analysis of HCMV Induced-Nuclear Membrane Structures by FIB/SEM Tomography: Insight into an Unprecedented Membrane Morphology." Viruses 7(11): 5686-5704.

von Appen, A. and M. Beck (2016). "Structure Determination of the Nuclear Pore Complex with Three-Dimensional Cryo electron Microscopy." J Mol Biol 428(10 Pt A): 2001-2010.

Walther, P. and A. Ziegler (2002). "Freeze substitution of high-pressure frozen samples: the visibility of biological membranes is improved when the substitution medium contains water." Journal of Microscopy 208: 3-10.

Wandke, C. and U. Kutay (2013). "Enclosing chromatin: reassembly of the nucleus after open mitosis." Cell 152(6): 1222-1225.

Watanabe, S., A. Punge, G. Hollopeter, K. I. Willig, R. J. Hobson, M. W. Davis, S. W. Hell and E. M. Jorgensen (2011). "Protein localization in electron micrographs using fluorescence nanoscopy." Nat Methods 8(1): 80-84.

Wei, D., S. Jacobs, S. Modla, S. Zhang, C. L. Young, R. Cirino, J. Caplan and K. Czymmek (2012). "High-resolution three-dimensional reconstruction of a whole yeast cell using focused-ion beam scanning electron microscopy." Biotechniques 53(1): 41-48.

White, J. G., D. G. Albertson and M. A. Anness (1978). "Connectivity changes in a class of motoneurone during the development of a nematode." Nature 271(5647): 764-766.

Wisse, E., R. B. De Zanger, K. Charels, P. Van Der Smissen and R. S. McCuskey (1985). "The liver sieve: considerations concerning the structure and function of endothelial fenestrae, the sinusoidal wall and the space of Disse." Hepatology 5(4): 683-692.

Woog, I., S. White, M. Buchner, M. Srayko and T. Muller-Reichert (2012). "Correlative light and electron microscopy of intermediate stages of meiotic spindle assembly in the early Caenorhabditis elegans embryo." Methods Cell Biol 111: 223-234.

Yang, Z. (2000). "Caveat on the error analysis for stereological estimates." Image Analysis and Stereology: 9-13.

Yao, N. (2007). "Focused Ion Beam Systems." Cambridge University Press.

Young, R. J., T. Dingle, K. Robinson and P. J. A. Pugh (1993). "An application of scanned focused ion beam milling to studies on the internal morphology of small arthopods." Journal of Microscopy-Oxford 172: 81-88.

Zhou, Z. H. (2011). "Atomic resolution cryo electron microscopy of macromolecular complexes." Adv Protein Chem Struct Biol 82: 1-35.

7.2 List of Figures

7.3 List of Tables